NOVEL APPLICATIONS OF METEORIC- AND IN SITU-PRODUCED BERYLLIUM-10 IN THE EAST ANTARCTIC

Rachel D. Valletta

A DISSERTATION

in

Earth and Environmental Science

Presented to the Faculties of the University of Pennsylvania

in

Partial Fulfillment of the Requirements for the

Degree of Doctor of Philosophy

2017

Supervisor of Dissertation

Jane K. Willenbring
Associate Professor, Geosciences Research Division, UCSD

Graduate Group Chairperson

Douglas J. Jerolmack
Associate Professor, Earth and Environmental Science

Dissertation Committee

Douglas J. Jerolmack, Associate Professor, Earth and Environmental Science

David Goldsby, Associate Professor, Earth and Environmental Science

Irina Marinov, Assistant Professor, Earth and Environmental Science

NOVEL APPLICATIONS OF METEORIC- AND IN SITU-PRODUCED BERYLLIUM-10 IN THE EAST ANTARCTIC

For Sugah and Pa

ACKNOWLEDGEMENTS

Thank you to my academic advisors for their expansive knowledge and personal guidance:

My committee members and external advisors for their thoughtful commentary and critique and contributions to this work, especially Dr. Adam R. Lewis and Dr. Sandra Passchier.

Dr. Gilles Brocard, for early guidance, training in the field, and a rewarding friendship.

G-085 members and, especially, Dr. Kate Swanger, who graciously offered me an opportunity to contribute to her field campaign.

To undergraduate academic advisors, who both encouraged and enabled me to begin this journey, including Dr. Gregory Hoke and Dr. Julie Brigham-Grette.

Finally, thank you to Dr. Jane K. Willenbring, for boundless enthusiasm and creativity.

Heartfelt thanks to my fellow graduate students for helping me keep a healthy work-life balance, especially Aunty Nini, Tina-Beana, and my office boys. A special thank you to Mama Joan for keeping us all in line!

To my support network of friends, now scattered across the globe: thank you for your diverse social and cultural education.

Thanks above all to my family - including Stout, Beans and Pickles! - for their enduring support, infectious laughter, and oversized Sunday dinners. To Scuba, for teaching me to always "keep my eyes peeled." To Uncle Billy, for first pushing me towards scientific research in the ultimate pursuit of effecting social change. To Pappy, for always supporting "his gals."

Especially, I am beholden to the immeasurably strong women in my life, without whom I would be much worse for the wear:

Ma, for never letting me miss the "BUS!"

Nana and Grams, the Italian grandmothers everyone else wish they had.

My sisters, Jessica and Samantha, for always reminding me of the importance of laughter and for teaching me the value of hard work and pure grit. "I love you more...Diddly."

My newest sister, Vanessa. We made it, Pooh!

And finally, Amélie. Thank you for maintaining an eternal optimism, the likes of which I will never understand, but I am constantly in awe of.

Funding support

This work was made by possible by various University of Pennsylvania entities, including the Benjamin Franklin Scholarship, the Orville Phillips Fellowship, and research grants from the Graduate and Professional Student Assembly and the Graduate Student Government of the School of Arts and Sciences. The Geological Society of America graduate student research award and the J. Hoover Mackin research award supported the cost of sample analyses presented in Chapters 3 and 5. Several National Science Foundation grants supported this work and include CAREER grant #1651243 to Jane K. Willenbring, and Antarctic Geoscience awards #1043554 to Jane K. Willenbring and #0739693 to Adam R. Lewis and Allan C. Ashworth.

ABSTRACT

NOVEL APPLICATIONS OF METEORIC- AND IN SITU-PRODUCED BERYLLIUM-10 IN THE EAST ANTARCTIC

Rachel D. Valletta

Jane K. Willenbring

This work comprises three novel applications of *in situ*- and meteoric-produced ^{10}Be in East Antarctica. Sampled deposits cover a wide spatiotemporal transect through the Dry Valleys, from an inland, middle elevation location of Quaternary age, to a mid-valley, high elevation location of Miocene age, and finally to an offshore, submarine location of Pliocene age. Each research chapter we present is a unique project unto itself, but all chapters utilize the cosmogenic radionuclide beryllium-10 (^{10}Be).

In the first application, we present "Difference Dating," a new approach to date glacial moraines in regions where traditional exposure age dating is fraught with complications. Difference Dating allows for the construction of deglaciation chronologies in regions where they are frequently precluded by inheritance issues. We use Difference Dating to constrain the ages of Quaternary moraines in an alpine glacial cirque, Wright Valley, Dry Valleys.

The second and third applications use meteoric-produced ^{10}Be in two different depositional settings. In marine sediments, we recast the ^{10}Be/^{9}Be ratio as a proxy for East Antarctic Ice Sheet freshwater discharge during mid-Pliocene interglacials. Using this record, we suggest that zones of deep water formation may be significant in funneling Be into the global thermohaline circulation belt. We also apply the meteoric-produced ^{10}Be system to paleolake sediments, where extremely low concentrations are used to construct an age model extending to 14-17.5 My. This range is commensurate with lake sediment deposition during the Middle Miocene Climatic Optimum, a rare Antarctic terrestrial deposit of this globally significant warming event.

TABLE OF CONTENTS

ACKNOWLEDGEMENTS iv

ABSTRACT vi

TABLE OF CONTENTS vii

LIST OF TABLES xi

LIST OF ILLUSTRATIONS xii

CHAPTER 1 : Introduction 1

1.1 Context 1

1.2 Cosmogenic radionuclide dating 5

1.3 Thesis structure 6

CHAPTER 2 : Background Information 9

2.1 Introduction 9

2.2 *In situ* production 10

2.2.1 Exposure and burial dating with *in situ*-produced CRNs 11

2.2.2 Inheritance 13

2.2.3 *In situ* production scaling models 14

2.3 Meteoric production of ^{10}Be 15

2.3.1 Determining soil erosion rates using meteoric ^{10}Be 17

2.3.2 ^{10}Be/^{9}Be in marine sediment cores 18

2.4 Summary 19

CHAPTER 3 : "Difference Dating:" a novel approach towards dating alpine glacial moraines 25

3.1 Introduction . . . 25
3.1.1 Regional setting . . . 26
3.1.2 Boulder scatter . . . 27
3.1.3 Desert pavement exposure histories . . . 28
3.2 Material and Methods . . . 29
3.2.1 Experimental methods . . . 29
3.2.2 Numerical methods . . . 30
3.2.2.1 Calculating shielding factors . . . 33
3.3 Results . . . 34
3.3.1 Radionuclide measurements . . . 34
3.3.1.1 ^{10}Be . . . 34
3.3.1.2 ^{26}Al . . . 35
3.3.1.3 Outlier exclusion . . . 35
3.3.2 Exposure ages and model results . . . 36
3.3.3 Outer moraine 1 . . . 36
3.3.4 Inner moraine 2 . . . 37
3.3.4.1 Additional Al/Be results . . . 38
3.4 Discussion . . . 38
3.4.1 Difference Dating: future directions . . . 38
3.4.2 Paleoclimatic inferences . . . 40
3.5 Conclusions . . . 40

CHAPTER 4 : ^{10}Be/^{9}Be ratios reflect East Antarctic Ice Sheet mass changes: a record offshore the Wilkes Subglacial Basin . . . 51
4.1 Introduction . . . 51
4.1.1 ^{10}Be in Antarctic marine sediments . . . 52
4.2 Setting . . . 54
4.3 Methods . . . 55
4.3.1 Be leaching . . . 55

4.3.2 Diatom separation and dissolution 56
4.4 Results and Discussion 57
4.4.1 Authigenic ^{10}Be 57
4.4.2 Authigenic ^{9}Be 59
4.4.3 Authigenic ^{10}Be/^{9}Be 60
4.4.4 Opal ^{9}Be 60
4.5 ^{10}Be delivery during interglacials 61
4.5.1 The impact of paleoproductivity 61
4.5.2 The impact of sea ice coverage 62
4.5.3 ^{10}Be in deep water formation zones 63
4.6 Summary 64

CHAPTER 5 : Extreme decay of meteoric beryllium-10 as a proxy for persistent aridity 73
5.1 Introduction 73
5.2 Sediment age model 75
5.3 Methods 77
5.3.1 Treating paleolake sediments 77
5.3.2 Error assessment 77
5.3.3 Choosing a flux value, Q 78
5.4 Results 78
5.5 Discussion 79
5.5.1 Middle Miocene climatic transitions and Paleolake Friis emplacement 79

CHAPTER 6 : Summary 88
6.1 Difference Dating 88
6.2 Authigenic ^{10}Be/^{9}Be as a proxy for East Antarctic Ice Sheet melt 91
6.3 Extending the upper age limit of meteoric ^{10}Be in paleolake sediments . . . 92

APPENDIX A 93

BIBLIOGRAPHY 127

INDEX 128

LIST OF TABLES

TABLE 3.1 : Cosmogenic radionuclide data 49

TABLE 3.2 : Monte Carlo modeling results and shielding factors 50

TABLE 4.1 : Be isotopes in authigenic and lithogenic fractions of U1361a sediments 70

TABLE 4.2 : Pearson correlation coefficients of geochemical proxies in U1361a sediments 71

TABLE 4.3 : ^{9}Be in opal 72

TABLE 5.1 : Meteoric ^{10}Be adhered to Paleolake Friis sediments. 85

TABLE 5.2 : Erosion rates used to estimate Paleolake Friis sediment age. 86

TABLE 5.3 : Concentration ranges of meteoric ^{10}Be adhered to lake sediments worldwide 87

TABLE A.1 : BET surface area in U1361a sediments 97

LIST OF ILLUSTRATIONS

FIGURE 2.1 : Cosmogenic radionuclide accumulation to steady state 21
FIGURE 2.2 : The Al/Be erosion island 22
FIGURE 2.3 : The effect of inheritance on glacial moraine dating 23
FIGURE 2.4 : Modern ^{10}Be atmospheric flux. 24

FIGURE 3.1 : Regional map of the Dry Valleys, Antarctica 42
FIGURE 3.2 : Sampling site OLY-38 43
FIGURE 3.3 : Ventifaction and quartzification in desert pavement clasts 44
FIGURE 3.4 : Kernel density estimates of pavement clasts 45
FIGURE 3.5 : Cumulative distribution function of pavement clasts 46
FIGURE 3.6 : Leibert Cirque difference dates 47
FIGURE 3.7 : Al/Be erosion-island plot 48

FIGURE 4.1 : The Adélie Coastline, East Antarctica 65
FIGURE 4.2 : Geochemical proxies in U1361a sediments 66
FIGURE 4.3 : Be isotopes in U1361a sediments 67
FIGURE 4.4 : ^{9}Be in biogenic opal 68
FIGURE 4.5 : Schematic illustration depicting Be delivery to a glacial margin . . 69

FIGURE 5.1 : Meteoric ^{10}Be measured in shallow Dry Valleys sediments 82
FIGURE 5.2 : ^{10}Be decay to “blank” concentration 83
FIGURE 5.3 : Modeled age range of Paleolake Friis sediments 84

FIGURE A.1 : XRD spectra of U1361a Sample 15 98
FIGURE A.2 : XRD spectra of U1361a Samples 2, 4 and 5 99
FIGURE A.3 : XRD spectra of U1361a Samples 12, 18 and 19 100

FIGURE A.4 : XRD spectra of U1361a Sample 22, size fractions 2-5μm, 5-10μm, and >10μm 101
FIGURE A.5 : XRD spectra of U1361a Samples 1 and 6 102
FIGURE A.6 : Assemblage of SEM-derived image of Sample 15 diatoms after cleaning procedure. 103
FIGURE A.7 : Sample 22, SEM image of <2μm fraction 104
FIGURE A.8 : Sample 22, SEM image of 2-5μm fraction. 105
FIGURE A.9 : Sample 22, SEM image of 5-10μm fraction. 106
FIGURE A.10 : Sample 22, SEM image of >10μm fraction. 107
FIGURE A.11 : U1361a grain size frequencies 108

CHAPTER 1 : Introduction

1.1. Context

Since its inception ∼34 My ago (*Passchier et al.*, 2016), the Antarctic Ice Sheet has played a key role in driving global atmospheric and oceanic circulation. It is the single largest ice sheet in the world, containing 27 million km^3 of ice (*Fretwell et al.*, 2013) (compared to Greenland's 2.96 million km^3) (*Bamber et al.*, 2013), composed of three main portions: the West and East Antarctic Ice Sheets and the Antarctic Peninsula. Today, this region attracts intense research focus because of its potential contributions to global sea level rise under current and projected anthropogenic warming (*Vaughan et al.*, 2013). In general, it is challenging to quantify future ice sheet contributions to sea level rise because of elongated equilibrium-response times (i.e. how long the ice sheet takes to reach a new equilibrium following a systemic perturbation) (*Golledge et al.*, 2015). Recent model predictions range due to differing underlying physics, and place upper bounds on Antarctic contributions to global mean sea level rise by 2100[1] between 30-40 cm (*Golledge et al.*, 2015; *Ritz et al.*, 2015) and as much as 77 cm (*DeConto and Pollard*, 2016).

Alone, the East Antarctic Ice Sheet (EAIS) contains 53 m of sea level equivalent (*Fretwell et al.*, 2013). Until quite recently, the EAIS was thought to be largely impervious to the effects of anthropogenic warming, even while the Greenland and West Antarctic Ice Sheets saw increasing rates of ice mass loss (Vaughan et al., 2013). However, the advent of more precise, dedicated satellite and airborne altimetry capabilities have produced surprising observations of the EAIS. For example, *Pritchard et al.* (2009) documented dynamic thinning in isolated coastal regions of the EAIS with rates comparable to those in coastal Greenland and the West Antarctic. *Rignot et al.* (2013) confirmed this result, showing that most EAIS mass loss is attributable to calving, while West Antarctic Ice Sheet mass loss is currently dominated by ice shelf melting. Both studies noted significant changes in low-lying regions, where warm ocean waters can lubricate grounding zones and drive ice shelf thinning. One

[1] Under the IPCC's RCP8.5 high emissions scenario (*Vaughan et al.*, 2013)

such region is the Wilkes Land, where much of the subglacial basin is below sea level and inland-dipping. This region contains 9 m of sea level equivalence alone, greater than the entire West Antarctic Ice Sheet (*Vaughan et al.*, 2013). Wilkes Land is expected to contribute to the EAIS's accelerated contributions to global mean sea level rise in the coming centuries (*DeConto and Pollard*, 2016).

How extensive will East Antarctic ice mass loss be under future warming? And, how has the EAIS responded to similar warming trends in the past? While we construct numerical simulations to predict future changes (e.g., *DeConto and Pollard*, 2003; *Huybrechts*, 1993; *Hill et al.*, 2007; *Pollard et al.*, 2015), ultimately these simulations are constrained by geologic data. Geologists reconstruct paleo ice sheet geometries and compare them with proxy records of known forcing parameters, such as temperature and CO_2 levels. Relative to its size and importance as a driver in global atmosphere and ocean systems, geologic samples capturing EAIS dynamics through time are sparse.

Traditionally, geologists have focused their research efforts on the Dry Valleys region. As the largest continuous expanse of ice-free land on the Antarctic continent, it is suitable for the study of EAIS margin dynamics in response to climatic forcing. For many years, geomorphology and paleoclimate studies in the Dry Valleys were dominated by a vigorous debate over the EAIS's susceptibility to collapse during previous warm intervals [for reviews, see *Wilson* (1995), *Barrett* (2013)].

Beginning in the 1980s, researchers in the Dry Valleys posited that the EAIS was an unstable feature that fluctuated dramatically under mildly warmer climate intervals and collapsed entirely as recently as the Pliocene (*Barrett et al.*, 1992). These studies were largely based on biostratigraphy of marine diatoms, which were discovered in high elevation, inland, warm-based glacial deposits of Pliocene age (the Sirius Group) (*Webb et al.*, 1984). The location of the Sirius Group was interpreted to mean a significant inland intrusion of marine waters following a full-scale collapse of the EAIS during Pliocene warming. This "unstable hypothesis" would imply that the EAIS was intensely susceptible to mild Pliocene warming

of only 2-4°C (*Haywood and Valdes*, 2004), comparable to that projected in the coming century (*Stocker*, 2014). The "unstable" hypothesis was later weakened and replaced by the contradicting "stable hypothesis," based largely on geomorphological studies. [Indeed, it was recently found that in Pliocene climate conditions, marine diatoms could be transported aerially to high elevation, ice-free regions, thus negating the necessity for a full-scale EAIS collapse for emplacement of the Sirius Deposits (*Scherer et al.*, 2016)].

The "stable" hypothesis claimed that the EAIS is a stable feature under persistent cold and dry climate conditions since the middle Miocene and at most experienced only minor coastal contractions (*Marchant et al.*, 1993; *Sugden et al.*, 1993; *Sugden*, 1996; *Lewis et al.*, 2007, 2008). Perhaps the most compelling evidence for persistent hyperarid, polar conditions was the presence of unaltered ash deposits scattered throughout the Dry Valleys (*Marchant et al.*, 1993, 1996; *Lewis et al.*, 2007, 2008). In many locations ashfalls infill sand wedge troughs, which only form in cold/dry conditions. Elsewhere, ashes rest on steep slopes and valley floors, and their positioning is indicative of long-term landscape stability. Persistent cold and dry climatic conditions are also indicated from pristine volcanic glass shards that lack evidence for hydration cracking and clay formation. Laser fusion $^{40}Ar/^{39}Ar$ analyses are used to date individual glass shards and sanidine and anorthoclase crystals within ashfalls. Reported ages of Dry Valley glasses stretch through the middle Miocene, implying an uninterrupted polar desert climate, since at least that time.

The geomorphology and geochemistry records contained within ashfalls are robust, but they are exceptionally rare given the extent of the Dry Valleys region. More recently, Dry Valleys research has relied heavily on cosmogenic radionuclide exposure age dating to constrain valley and alpine glacier elevation change in response to warming events (e.g., *Ivy-Ochs et al.*, 1995; *Staiger et al.*, 2006a; *Swanger et al.*, 2011) and to document extremely low denudation rates (e.g., *Summerfield et al.*, 1999; *Putkonen et al.*, 2008; *Morgan et al.*, 2010). These works complement existing geomorphological studies and observe that brief warming intervals punctuate a dominantly cold, dry climate and that alpine and valley glaciers have

endured throughout this time.

In addition to the inner Dry Valleys terrestrial record, the coastal and marine sedimentary record also documents the evolution of the EAIS from the Miocene. The closest such record lies in the nearby Ross Sea, and indicates dynamic EAIS behavior through the early to middle Miocene (*Fielding et al.*, 2011), but is largely incomplete following the middle Miocene and cannot corroborate EAIS permanence during this time. *Levy et al.* (2012) presented an onshore-offshore synthesis of sedimentary deposits from the Dry Valleys/Ross Sea and noted that warm-based, erosive outlet glaciers extended down through the Dry Valleys to the Ross Sea during maximum Pliocene warming, thus implying a persistent EAIS. At the marine sedimentary record offshore the Wilkes Land, the EAIS is described as a permanent, but oscillating, feature since the middle Miocene (*Escutia et al.*, 2005, 2011; *Cook et al.*, 2013). Minor, orbitally forced fluctuations accompanying pulsed warming events during the Pliocene are well documented (*Cook et al.*, 2013; *Patterson et al.*, 2014). More extreme fluctuations may have occurred in the distant Prydz Bay region, where tidewater glacier-like deposits record ice sheet incision and fjord downcutting (*Hambrey and McKelvey*, 2000) and seismic reflection profiles indicate a reorganization of sediment structure in Pliocene-age shelf sediments (*Rebesco et al.*, 2006).

Taking the terrestrial Dry Valleys record and EAIS marine sedimentary record together, it is likely that some unified theory is appropriate: the EAIS has remained a persistent feature since ∼12 My and has experienced warming-induced fringe melting during that time. As the marine sedimentary record indicates, the magnitude of EAIS retraction during warm interglacials is spatially heterogeneous and likely more extreme in low elevations.

No longer burdened by the notion of a full-scale collapse during the Pliocene, finer scale questions concerning the EAIS's fate under warming temperatures can be posed. A recent community-based roadmap for future Southern Ocean and Antarctic research prioritized EAIS-related research questions (*Kennicutt et al.*, 2015). Among these questions are, How fast has the Antarctic ice sheet changed in the past and what does that tell us about the

future? and, How did marine-based Antarctic ice sheets change during previous inter-glacial periods? Geological studies conducted on both marine and terrestrial deposits can play a key role in answering these questions. Central to any such effort is, of course, precise age control. In choosing the appropriate geochronometer to monitor EAIS change, the practitioner should consider sensitivity to geomorphic change, applicability in marine and terrestrial settings, and usefulness in relevant timescales.

1.2. Cosmogenic radionuclide dating

Cosmogenic radionuclide (CRN) dating is ideally suited for constructing age models on terrestrial and marine deposits in the Antarctic. The tool fills a vital role in the terrestrial realm especially, given that other geochronometers face significant challenges in the region and are limited to application through the mid-late Pleistocene or younger: organic materials for radiocarbon dating are often plagued with "old carbon," and have a maximum age range up to ∼60 ky (*Doran et al.*, 1994); carbonaceous sediments for uranium-thorium dating (e.g., *Higgins et al.*, 2000) are sparse, and have a maximum age range up to ∼500 ky; and glacial deposits selected for optically stimulated luminescence dating face issues of partial bleaching and low brightness, and have a maximum age range of up to a few 100 ky in exceptional circumstances (*Rhodes*, 2011).

Over the past three decades, advances in CRN dating techniques have revolutionized the field of geomorphology. The possible applications of CRN dating towards qualitatively and quantitatively understanding earth surface processes are ever-expanding. The list of suitable materials and processes is extensive and includes, but is not limited to, alpine glacial deposits (*Ivy-Ochs and Briner*, 2014), glacially-sculpted bedrock surfaces (*Nishiizumi et al.*, 1991), cave sediments (*Granger*, 2006), fault slip surfaces (*Benedetti and van der Woerd*, 2014), desert glass (*Klein et al.*, 1986), paleolake sediments (*Lebatard et al.*, 2010), paleosols (*Balco and Rovey*, 2008), rates of weathering and total denudation (*Willenbring and von Blanckenburg*, 2010a; *Riebe et al.*, 2015), rates of soil formation (*Dixon and Riebe*, 2014), and rates of river incision and coastal uplift (*Brocard et al.*, 2003). There may even exist

the future prospect for paleoaltimetric reconstruction (*Riihimaki and Libarkin*, 2007).

In the greater Dry Valleys region, CRNs are used in a diverse array of applications to quantify advance and retreat ages of alpine and valley glaciers (*Brook et al.*, 1993; *Staiger et al.*, 2006a; *Swanger et al.*, 2011, 2017), ages of buried ice features (*Bibby et al.*, 2016), rates of valley wall retreat (*Middleton et al.*, 2012), regolith degradation rates (*Putkonen et al.*, 2008; *Morgan et al.*, 2010), soil ages (*Graham et al.*, 2002; *Dickinson et al.*, 2012) and accumulation rates (*Schiller et al.*, 2014), and (minimal) subglacial erosion rates (*Atkins*, 2013). CRN measurements in marine sediments are used to characterize glacial vs subglacial sediment sources (*Sjunneskog et al.*, 2007) and to detect ice shelf presence or absence (*Yokoyama et al.*, 2016).

1.3. Thesis structure

The following three chapters outline three independent applications of CRN dating in both the terrestrial and marine realms. Each chapter is uniquely designed to contribute a new perspective on paleoclimatic trends in the East Antarctic through the use of CRN dating. In doing so, this work addresses several of *Kennicutt et al.*'s (2015) priority questions. My sampling locations cover a vast spatiotemporal transect, from inner Dry Valleys, middle elevation sites of Miocene age, to mid-valley high elevation sites of Quaternary age, and finally to an offshore, marine site of Pliocene age.

Chapter 2 describes some of the technical aspects of dating deposits with CRNs. I provide an outline of *in situ* (within mineral) and meteoric (atmospheric) production mechanisms and introduce some of the challenging aspects of each. For *in situ* applications, this includes the use of atmospheric scaling models. I also discuss specific dating applications, including exposure dating, burial age dating, soil age dating, and the use of the $^{10}Be/^{9}Be$ ratio in marine systems.

Chapter 3 presents a novel sampling technique used to date glacial moraines. This work applies two common techniques of *in situ*-produced isotopes, those of glacial moraine boulder

exposure dating and burial dating, and combines them with a newly developed sampling approach that we have termed, "Difference Dating." Difference Dating offers a brand new approach to quantifying the formational ages of glacial moraines in the Dry Valleys, where standard boulder exposure dating techniques are limited by exogenous factors such as cold-based glaciation. Difference Dating allows the practitioner to: 1) identify moraine boulders that over- or underestimate true moraine age and 2) quantify a moraine age independent of that determined from moraine boulder sampling (which is most likely inaccurate). This chapter is under review at *Quaternary Geochronology*.

Chapters 4 and 5 use applications of meteoric-produced ^{10}Be. Chapter 4 presents a record of radioactive ^{10}Be normalized to its stable isotope ^{9}Be in continental shelf sediments offshore the Wilkes Land Region of the East Antarctic Ice Sheet. Commonly, the ^{10}Be/^{9}Be record measured in marine authigenic minerals is used to interpret paleomagnetic fluctuations or as a tracer of water mass movement. Our record, instead, is dominated by the so-called environmental signal, which is imparted on the dissolved ^{10}Be/^{9}Be record by melting glacial ice. I compare our record with existing sedimentological and geochemical data collected during and after IODP cruise 338 (site U1361a). I show that the ^{10}Be/^{9}Be record reflects advance and retreat cycles of the East Antarctic Ice Sheet, which are not significant enough to alter deep marine records. This chapter is in preparation for submission to the journal *Paleoceanography*.

Chapter 5 presents a terrestrial record from the Friis Hills, Dry Valleys. We sample meteoric ^{10}Be from paleolake sediments, which are contained within a series of stacked, alternating paleosol and alpine glacial deposits. The lake sediments contain a rare fossil assemblage indicative of warmer, wetter tundra-like conditions, including fossil leaf impressions of *Nothofagus* (southern beech) and beetle carcasses, now extinct on the continent. *Nothofagus* has been found at only one other site in the Dry Valleys where it and other plant species were used to estimate summer temperatures of $\sim$5°C (*Lewis et al.*, 2008). Using extremely low [^{10}Be] measured on replicate samples, I develop a chronology for Paleolake

Friis, limiting its age to between 14-17.5 My. This chronology agrees well with stratigraphically underlying ash deposits of 19.76 My and likely coincides with regional records of the Middle Miocene Climatic Optimum, a period of intense global terrestrial and marine warming. Our age model supports the notion that Dry Valleys paleoclimate reached near-modern conditions at least as long as 14 My ago, when the East Antarctic Ice Sheet significantly expanded and established a largely cold-based state, and precludes the possibility of East Antarctic Ice Sheet collapse during more mild Pliocene warming events. This chapter is published in Nature's *Scientific Reports*.

Finally, Chapter 6 presents a summary of these major findings. I prescribe future recommendations for technique development, particularly pertaining to Chapters 3 and 4.

CHAPTER 2 : Background Information

This chapter serves as a brief synopsis of some of the underlying theory and technical aspects of cosmogenic radionuclide dating. It is meant to introduce the unfamiliar reader to a broad overview of *in situ* and meteoric cosmogenic radionuclides and their usefulness to geochronology.

2.1. Introduction

Cosmogenic radionuclides (CRN) are very rare, radioactive isotopes produced during interactions between secondary cosmic radiation and target nuclei in the Earth's atmosphere ("meteoric" production) and within minerals at the Earth's surface ("*in situ*" production). Primary cosmic radiation, originating both within and external to our galaxy, is constantly bombarding the Earth's atmosphere and initiating the particle cascade, a showering of successively less energetic particles termed secondary cosmic radiation. These reactions are greatest at high latitudes, where the Earth's geomagnetic field lines are sub-perpendicular to the Earth's surface, and least at the equator, where geomagnetic field lines are sub-parallel to the Earth's surface and better deflect incoming cosmic radiation (*Lal*, 1991). During these nuclear interactions, high-energy neutrons (>10 MeV) collide and break apart target nuclei in a process known as spallation. Such a reaction produces ^{10}Be [^{16}O(n,4p3n)^{10}Be] and ^{26}Al [^{28}Si(n,p2n)^{26}Al]. As these neutrons successively lose energy, they enter the thermal energy state (0.01-0.025 MeV) at which point the neutron is removed from its environment via neutron capture, as in the production of ^{14}C [^{16}O(n,2pn)^{14}C]. The particle cascade also produces fast and slow muons, which produce CRNs via spallation reactions and muon capture, respectively (*Gosse and Phillips*, 2001). Both spallation and neutron capture may occur *in situ* or meteorically.

2.2. *In situ* production

In the upper two meters of the lithosphere, CRN production is dominated (∼98%) by spallation reactions, but muogenic production likely dominates at depths >10 m (*Gosse and Phillips*, 2001). As in the atmosphere, nuclide production in the lithosphere decreases exponentially with increasing depth and is described as,

$$P(z) = P_0 \; exp\Big(\frac{-z\rho}{\Lambda}\Big) \tag{2.1}$$

where P_0 is production of a nuclide at the Earth's surface (atoms g^{-1} y^{-1}), z is sample depth (cm), and ρ is sample density (g cm^{-3}). Λ is the attenuation length of the nuclide through Earth materials (g cm^{-2}). More specifically, the attenuation length is the thickness of mass (rock, air, soil) required to attenuate incoming cosmic rays by a factor of e^{-1}, the e-folding length (*Gosse and Phillips*, 2001).

In addition to the attenuation effects of the atmosphere, physical shielding may extensively attenuate CRNs. Shielding occurs when physical barriers obstruct particle ray paths and slow or entirely attenuate the particle. The three types of shielding include topographic, self, and geometric shielding. Topographic shielding is caused by topographic obstructions surrounding a sampling site, such as nearby relief. Sampling procedures can be optimized to avoid this issue, and typically topographic shielding is only significant in extreme cases (e.g. when sampling near cliff faces). Self-shielding occurs when the sampling surface dips at values $> 30°$ (*Balco et al.*, 2008). Self-shielding is also a result of sample thickness, where the bottom of the sample is shielded by the mass of the entire sample. Topographic and self-shielding are both easily adjusted for with field measurements of dip angle, sample thickness, and observations of the surrounding horizon. Geometric shielding occurs when an external mass covers a sampling site, e.g. an overlying boulder or sediments. This type of shielding is more difficult to constrain. Complex particle physics-based modeling

approaches to account for geometric shielding do exist (e.g., *Masarik and Beer*, 1999), but these are computationally expensive and time consuming. A newer tool based on 3D modeling of geometric obstructions is also available (*Balco*, 2014). See Chapter 3 for an application of *Balco*'s (2014) MATLAB procedure for quantifying attenuation due to geometric obstructions.

2.2.1. Exposure and burial dating with in situ-produced CRNs

Through time, CRN concentrations will accumulate within rocks and sediments exposed to cosmic radiation. Nuclide inventory will only be removed via surface erosion or nuclide decay, making CRNs an attractive tool for measuring rates of Earth surface processes (*Granger et al.*, 2013). The characteristic exponential decay of all radionuclides is described by the radioactive decay law,

$$N(t) = N_0 exp(-\lambda t) \tag{2.2}$$

where some initial CRN concentration, N_0, decays over time, t, to some new concentration, $N(t)$. The rate of decay is dictated by a nuclide's decay constant, λ, where $\lambda = \frac{ln(2)}{t_{1/2}}$. Half-lives of commonly measured CRNs are as follows: ^{10}Be ($t_{1/2}$=1.39±0.014 My) (*Chmeleff et al.*, 2010; *Nishiizumi et al.*, 2007), ^{26}Al ($t_{1/2}$=708±17 ky) (*Nishiizumi*, 2004), and ^{14}C ($t_{1/2}$=5730 y).

In a rock or sediment sample undergoing a constant rate of erosion, ε (cm y^{-1}), the measured CRN inventory of the sample is expressed as,

$$N(z,t) = N_{inh}(z)e^{-\lambda t} + \frac{P_{sp}(z)}{\lambda + \rho\varepsilon/\Lambda_{sp}}\left[1 - e^{-(\lambda+\rho\varepsilon/\Lambda_{sp})t}\right] + \int_0^t P_{mu}(z+\varepsilon\tau)d\tau \tag{2.3}$$

where $N(z,t)$ is a measured concentration of cosmogenic radionuclide (atoms g^{-1}), N_{inh} is the inherited nuclide concentration, $\tau = (t_{1/2})^{-1}$ (y^{-1}), ρ is material density (g cm^{-3}),

t is time of exposure (y), and P_{sp} and P_{mu} are production rates (atoms g^{-1}) into the subsurface via spallogenic and muogenic production, respectively. Total production rates vary per nuclide: for *in situ*-produced ^{10}Be, ^{26}Al, and ^{14}C, reference (sea-level, high latitude) production rates are 4-5, 35, and 18-20 atoms g^{-1} y^{-1}, respectively (*Granger et al.*, 2013). Frequently, the final muogenic production term is ignored, because $P_{mu} \ll P_{sp}$ and $\rho\varepsilon/\Lambda_{sp} \ll \lambda$. Meaning, muogenically produced ^{10}Be decays before reaching the surface.

Note that Eq. 2.3 is fulfilled when an erosion rate is independently known. This can be achieved by measuring short-lived nuclides that will reach steady state quickly (in the Dry Valleys, perhaps ∼30 ky for ^{14}C). The steady state scenario is one in which nuclide production rate is equal to the rate of nuclide loss via decay and erosion; this is also termed secular equilibrium (*Lal*, 1991). Nuclides with shorter half-lives will reach steady state much faster than a comparatively longer-lived nuclide under the same erosive conditions. Figure 2.1 shows the timing of arrival at steady state for commonly measured CRNs. In the erosion-limited, steady state scenario, Eq. 2.3 simplifies to,

$$N(z) = \frac{P_{sp}(z)}{\lambda + \rho\varepsilon/\Lambda_{sp}} \tag{2.4}$$

(assuming negligible contributions from muogenic production). From Eq. 2.4, ε is obtained, and can be used to determine the time of exposure for a longer-lived nuclide using Eq. 2.3 (*Dunai*, 2010).

In the Dry Valleys, Antarctica, erosion rates are extremely low (on the order of 0.1-10 cm My^{-1}), and at steady state the erosion term in the denominator approaches zero, such that $N(z) \propto P/\lambda$. Thus, solving Eq. 2.4 with a relatively longer-lived nuclide will yield a sample's maximum exposure age. The term "maximum exposure age" is flexible; it accepts an underestimation of true exposure age due to loss of nuclide inventory during erosion while still offering a numerical value with geological significance.

As the exposure age quantifies the total time a sample has been exposed to cosmic radiation, so too a burial age quantifies the time a sample has spent buried and blocked from cosmic radiation (*Granger and Muzikar*, 2001; *Granger*, 2006). The time a sample spends buried will only be reflected in its measured CRN concentration if the time is long enough in comparison to the nuclide's half-life. To unravel complex burial histories, isotopes that accumulate on similar timescales, but with different half-lives, are paired. Common pairings include ^{10}Be with either ^{26}Al or ^{14}C. The ratio of the two chosen CRNs is directly related to a sample's burial time and erosion rate and is expressed as (*Granger*, 2006),

$$\frac{N_1}{N_2}(t) = \frac{P_1}{P_2}\left[\frac{\tau_2^{-1} + (\lambda + \rho\varepsilon/\Lambda)}{\tau_1^{-1} + (\lambda + \rho\varepsilon/\Lambda)}\right] \tag{2.5}$$

Here, production rate (P) of nuclides 1 and 2 represents initial production rate prior to burial. See Chapter 2 for an application of Eq. 2.5 using Al and Be. The isotope pair ^{26}Al and ^{10}Be is produced at the Earth's surface at a ratio of ∼6.75:1, and may vary slightly based on precise site latitude and elevation (e.g., *Corbett et al.*, 2017). Because ^{26}Al decays faster than ^{10}Be, the ^{26}Al/^{10}Be measurement can never exceed this ratio of production rates (*Granger*, 2006). Under constant exposure, ^{26}Al will reach secular equilibrium faster than ^{10}Be; when ^{10}Be reaches its secular equilibrium, the ratio ^{26}Al/^{10}Be has decreased to ∼3. The effect of burial on the ^{26}Al/^{10}Be ratio is displayed in Figure 2.2.

2.2.2. Inheritance

An important consideration in all *in situ*-produced CRN studies is the possibility of inherited nuclide inventory. Inheritance is any CRN concentration accumulated prior to sample deposition at its current location. In Antarctica, this phenomenon is commonly observed in glacial moraine boulders and produces inaccurate exposure ages that overestimate the true age of feature formation (e.g., *Brook et al.*, 1993; *Ackert Jr. and Kurz*, 2004; *Margerison et al.*, 2005; *Staiger et al.*, 2006a; *Swanger et al.*, 2011). This is largely attributed to slow

geomorphic change in the region; see Chapter 3. See Figure 2.3 for an example of the effect of inheritance on glacial moraine dating. Outside of the polar regions, inheritance is observed far less frequently (*Putkonen and Swanson*, 2003).

Researchers have addressed the issue of inheritance in a variety of direct and indirect ways: by sampling alluvium at depth where production is negligible (in Eq. 2.1, as $z \rightarrow \infty$, $P(z) \rightarrow 0$) and assuming measured concentration represents the inherited portion (e.g., *Anderson et al.*, 1996); by modeling randomly distributed periods of prior exposure assigned via constrained Monte Carlo simulations (e.g., *Heyman et al.*, 2011); and by measuring control samples representative of maximum inheritance (e.g., *Staiger et al.*, 2006a). See Chapter 3 for an expanded discussion on inheritance and a novel approach to explicitly quantifying inherited concentrations.

2.2.3. In situ production scaling models

Inherent to any CRN application is a reliable estimate of the local production rate. Because atmospheric attenuation slows secondary cosmic radiation, production rates at the Earth's surface are greater at high elevation (low atmospheric mass) and less at low elevation (high atmospheric mass). Production rates will also vary based on latitude, geomagnetic field strength, and solar modulation (*Masarik and Beer*, 1999, 2009). To account for production variation in time, elevation and location, one must employ a production scaling scheme. An efficient way to do so is to use an automated exposure age calculator (e.g., *Marrero et al.*, 2016), which offer several production scaling frameworks; two basic types exist. The first type of production scaling framework is derived from empirical fits to field data and include those based largely on cosmic-ray emulsion data and neutron-monitor data (*Lal*, 1991; *Stone*, 2000) and those based on neutron-monitor data alone (*Dunai*, 2001; *Lifton et al.*, 2005; *Desilets et al.*, 2006). The second, emerging type of production scaling framework is based on analytical fits to physics-based modeling (*Lifton et al.*, 2014). In exposure age calculators, these scaling procedures scale calibration data to a sampling site's location to produce a reference production rate ($P(0)$ in Eqs. 2.1,2.3,2.4). Calibration data comprises

accurate time-averaged production rates quantified at sites of independently known age (*Borchers et al.*, 2015).

Each scaling scheme differs in the manner in which it scales calibration data. For example, early production scaling schemes (*Lal*, 1991; *Stone*, 2000) are based upon latitude-altitude scaling and do not account for changes in the geomagnetic field, thus the nuclide production rate is assumed time-invariant. This assumption is perhaps more acceptable for older deposits, but younger (<100 ky) exposure ages may be substantially affected by known variations in the geomagnetic field, such as the Laschamp Excursion, and solar modulation, such as the Maunder Minimum. To address this issue, scaling schemes later incorporated cutoff rigidity (the minimum particle energy required to initiate the particle cascade, dependent on geomagnetic strength) (*Dunai*, 2010; *Desilets et al.*, 2006) and solar modulation (*Lifton et al.*, 2005, 2014), in addition to atmospheric pressure. As a result, each of these scaling schemes assumes time-variant production rates, which peak during conditions of a weak geomagnetic field and increased solar activity.

Thus, the practitioner must be prudent in selecting the appropriate production scaling framework for a given location. In Antarctica, especially at high elevation sites, the Lifton-Sato-Dunai elevation scaling scheme (*Lifton et al.*, 2014) appears to perform best (`https://cosmognosis.wordpress.com/2016/09/09/saturated-surfaces-in-antarctica/`).

2.3. Meteoric production of ^{10}Be

Meteoric ^{10}Be is produced via the same spallation reactions as *in situ*-produced ^{10}Be, but its target elements reside in the atmosphere rather than within the quartz lattice. After spallation, meteoric ^{10}Be forms oxides (^{10}BeO) and hydroxides ($^{10}BeOH_2$) and adheres to atmospheric aerosols, primarily sulfates (*Lal and Peters*, 1967). ^{10}Be will rapidly homogenize over 1-2 y in the atmosphere, smoothing out latitudinal differences in high atmosphere production rates. This mixing rate is confirmed both by surface ^{10}Be measurements (*Raisbeck et al.*, 1981) and atmospheric models (*Heikkilä et al.*, 2013). In this regard, meteoric

^{10}Be offers a great advantage over *in situ*-produced CRNs, because altitudinal scaling models, such as those discussed in Section 2.2.3, are in most cases unnecessary.

^{10}Be-bearing aerosols reach the Earth's surface via wet (rain, snow) or dry (dust) deposition. Fluxes are greatest in regions of high precipitation and near the mid latitudes, where stratospheric and tropospheric mixing are greatest (*Heikkilä et al.*, 2013); see Figure 2.4. The global average flux to the Earth's surface is 5.8 x 10^5 ^{10}Be atoms g^{-1} cm^{-1} y^{-1} (*Masarik and Beer*, 1999; *Field et al.*, 2006; *Heikkilä*, 2007).

Through continued deposition, meteoric ^{10}Be will accumulate at the surface and at depth as the isotope moves into the soil column via infiltration and clay illuviation (*Willenbring and von Blanckenburg*, 2010a). A typical depth profile of ^{10}Be in zones of constant soil production will decrease exponentially with increasing depth (e.g., *Brown et al.*, 1992) and peak in clay-rich Bt and fine-grained horizons (e.g., *Pavich et al.*, 1986). Aerosol-bound ^{10}Be also accumulates in ice and may enter the soil subsurface during ice melt (*Finkel and Nishiizumi*, 1997). This last mechanism of delivery has been observed in Dry Valleys locations that undergo surface snow melt (*Schiller et al.*, 2014).

Beryllium's chemical behavior in the environment is an area of active research. Some key findings from the literature as summarized from *Boschi* (2016) include:

- Be is highly particle reactive and readily sorbs to both mineral and organic fractions with high solid/fluid partition coefficients. Be has a high affinity for sorption to certain clay species, notably illite. Be sorption is strongly pH dependent, existing as its divalent cation at both low (<6) and high (>11) pHs, and forming insoluble $Be(OH)_2$ near neutral and slightly basic (∼8-9) pH.

- Certain soil characteristics, including surface area, grain size, and mineralogy, are observed to control Be sorption. Boschi herself refined this observation, offering a relationship to predict Be sorption based on a soil's cation exchange capacity and its quartz content, expressed as the inverse of quartz %. (This relationship is not yet

validated on a wide array of soil types or marine sediments.)

- Dissolved fresh water concentrations of Be (native ^{9}Be) are in the ppb to ppm range. After pH, other factors known to influence Be sorption include salinity, suspended particle concentration, organic matter composition, phosphorous and sulfur oxides.

Extensive reviews of Be environmental chemistry can be found (e.g., *Vesely et al.*, 2002; *Taylor et al.*, 2003).

A foundational understanding of Be in the environment enables the application of ^{10}Be for geomorphology studies. A slew of innovative techniques utilize ^{10}Be from terrestrial and marine deposits. Two of these techniques include measuring depth profiles of ^{10}Be in soils to quantify erosion rates and measuring ^{10}Be and its stable isotope ^{9}Be in deep marine authigenic minerals and ferromanganese deposits to trace continental sedimentation to the sea.

2.3.1. Determining soil erosion rates using meteoric ^{10}Be

In one notable geomorphological application, ^{10}Be soil profiles are used to date soil age and rates of soil production and erosion. In these applications, a soil's "age" is the time since it was first exposed to ^{10}Be-bearing precipitation. The age of an eroding soil surface is dependent on the depth-integrated inventory of ^{10}Be concentration, I (atoms cm^{-2}); the surface [^{10}Be], N_{surf} (atoms g^{-1}); the local ^{10}Be flux, Q (at cm^{-2} y^{-1}); the soil's erosion rate, ε (cm y^{-1}); and soil density, ρ (g cm^{-3}) (*Willenbring and von Blanckenburg*, 2010a) (their Eq. 8):

$$t = \frac{-ln\left(1 - \frac{I\lambda}{Q - \varepsilon\rho N_{surf}}\right)}{\lambda} \tag{2.6}$$

Note that the equation has two unknowns, t and ε. If one assumes the soil surface has

reached a steady state condition ($t \rightarrow \infty$), then I depends only on accumulation via nuclide flux and losses to erosion and decay (*Brown et al.*, 1987):

$$I = \frac{Q - \varepsilon \rho N_{surf}}{\lambda} \tag{2.7}$$

Note that, as in the *in situ* steady state application (Eq. 2.4), steady state meteoric ^{10}Be inventories adsorbed to soil constituents are directly proportional to production (here, encompassed by Q) offset by nuclide decay and erosion.

Willenbring and von Blanckenburg (2010a) derive an additional equation for steady state erosion based on a single surface ^{10}Be measurement:

$$N_{surf} = \frac{Q}{\rho \varepsilon} \tag{2.8}$$

where N_{surf}, Q, ρ and ε are as defined above. Typical values of N_{surf} are around 10^8-10^9 atoms g^{-1}, 2-3 orders of magnitude greater than the oldest measured *in situ*-produced concentrations. Unsurprisingly, N_{surf} values are greatest in older soils with low erosion rates (*Willenbring and von Blanckenburg*, 2010a). In addition to dating modern erosion rates, ^{10}Be profiles can constrain paleosol ages, first performed by *Lebatard et al.* (2010). See Chapter 5 for an application of Eq. 2.8 in dating paleolake sediments of Miocene age.

2.3.2. ^{10}Be/^{9}Be in marine sediment cores

Concentrations of ^{10}Be normalized to the stable isotope ^{9}Be are proposed as faithful recorders of deep ocean circulation patterns (*von Blanckenburg et al.*, 1996) and, on coarse timescales, shifts in continental sedimentation (*Willenbring and von Blanckenburg*, 2010b; *von Blanckenburg et al.*, 2012; *von Blanckenburg and Bouchez*, 2014; *von Blanckenburg et al.*, 2015). ^{10}Be/^{9}Be measured in authigenic marine sediments and ferromanganese crusts are expected to reflect the dissolved ^{10}Be/^{9}Be seawater ratio at the time of deposition. While ^{10}Be enters

the global oceans dominantly via fallout onto the ocean surface, ^{9}Be enters in riverine fluxes to the sea following chemical weathering and liberation from silicate minerals. Universally, native ^{9}Be in silicate minerals varies very little, typically 2.5±0.5 ppm (*von Blanckenburg et al.*, 2012). The dissolved ^{10}Be/^{9}Be ratio in seawater is thus dictated by four factors: the atmospheric flux of ^{10}Be, denudation rates within riverine basins, the fraction of ^{9}Be liberated via chemical weathering, and the fractions of terrestrial ^{9}Be and ^{10}Be released from freshwater into seawater (*von Blanckenburg and Bouchez*, 2014). Because the ratio is susceptible to changes in weathering intensity and denudation rates, deep marine ^{10}Be/^{9}Be records should show fluctuations in response to shifts in weathering intensity and/or denudation through the late Cenozoic. Using a global compilation, *Willenbring and von Blanckenburg* (2010b) presented constant marine ^{10}Be/^{9}Be measurements through the past 10 My and argued this record as evidence for a lack of major shifts in late Cenozoic weathering.

Before its use as a water mass tracer and proxy for continental sedimentation, ^{10}Be measurements collected from deep marine sediments were used to reconstruct paleomagnetic intensity (*Christl et al.*, 2003). Excursions in the geomagnetic field ultimately affect the magnitude of ^{10}Be delivered to deep marine locations by roughly ±20%. In several locations, aberrations in the ^{10}Be/^{9}Be record that cannot be explained by fluctuations in geomagnetic field strength alone are attributed to the "environmental signal," imparted by, for example, a change in regional freshwater discharge (*Simon et al.*, 2016) or as a result of sediment focusing (*Frank et al.*, 1995). See Chapter 4 for a recasting of the environmental signal as a useful record of freshwater discharge.

2.4. Summary

I have presented an abbreviated overview of *in situ* CRN production and meteoric ^{10}Be production. I have highlighted several limitations in modern *in situ*- and meteorically-produced CRN applications. Each of the following research chapters addresses one of these limitations:

- Exposure age dating that uses *in situ*-produced CRNs is sometimes prohibited by inheritance issues (Section 2.2.2). This problem is exacerbated in the Dry Valleys, Antarctica, where exogenous factors such as cold-based glaciation affect CRN accumulation. In Chapter 3, I introduce "Difference Dating," a new sampling technique for dating alpine glacial moraines. By measuring CRN inventories in multiple co-located deposits, the challenge of handling inherited CRN inventories is circumvented altogether. Difference Dating offers a significant advancement to the well-established technique of exposure age dating glacial moraines.

- Marine sedimentary records of $^{10}Be/^{9}Be$ are used to capture fluctuations in geomagnetic field strength and periods of continental denudation/shifts in terrestrial weathering rates. These records are sometimes muddled by the environmental signal (Section 2.3.2), which may be imparted by changes in sediment redistribution and melting glacial ice. In Chapter 4, I take advantage of the "environmental signal" that dominates a marine sedimentary record collected offshore the East Antarctic Ice Sheet. I show that $^{10}Be/^{9}Be$ fluctuations respond to freshwater discharging during interglacial periods, which may not be present in deeper marine records.

- ^{10}Be profiles in paleosediments can be used to reconstruct paleoerosion rates in deposits up to ∼10-12 My (Section 2.3.1). In Chapter 5, I document paleolake sediments with little to no [^{10}Be], indicating a sediment age >14 My. I extend beyond the age of the ^{10}Be system by solving Eq. 2.8 with a compiled database of global lake sediment [^{10}Be], regional rates of erosion, and evidence from lake sediments, to date the paleolake sediments at 14-17.5 My.

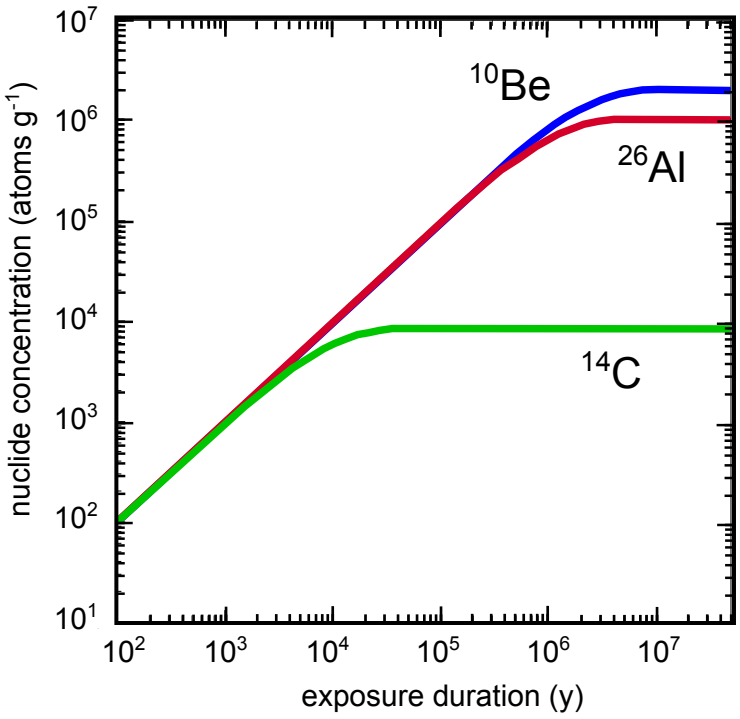

Figure 2.1: Cosmogenic radionuclide accumulation to steady state for commonly measured nuclides. Zero erosion assumed.

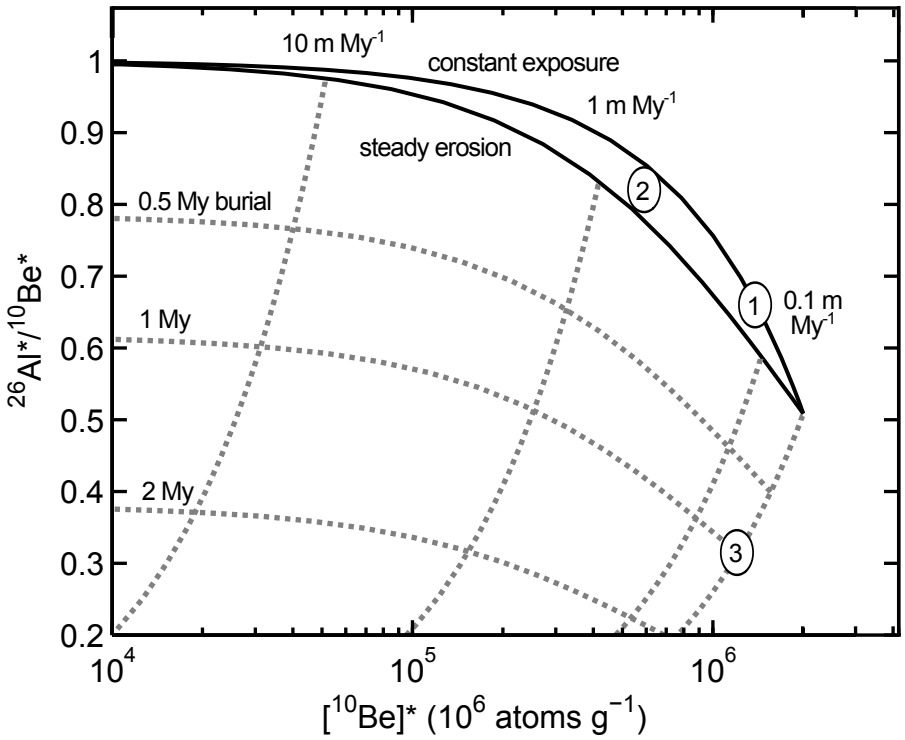

Figure 2.2: The steady state erosion plot in semilog space normalized to sea-level, high latitude production rates (*). The envelope represents the "steady state erosion island" (Lal, 1991). When first exposed to cosmic radiation, samples will accumulate ^{26}Al and ^{10}Be at a ratio of 1:1, and will travel along the constant exposure line until experiencing burial or erosion. 1: A sample that has undergone continuous exposure, no erosion, for 2 My. 2: A sample that has reached steady state with an erosion rate of 1 m My^{-1}. 3: A sample, previously at secular equilibrium, that has undergone sudden, deep burial and decay for 1 My.

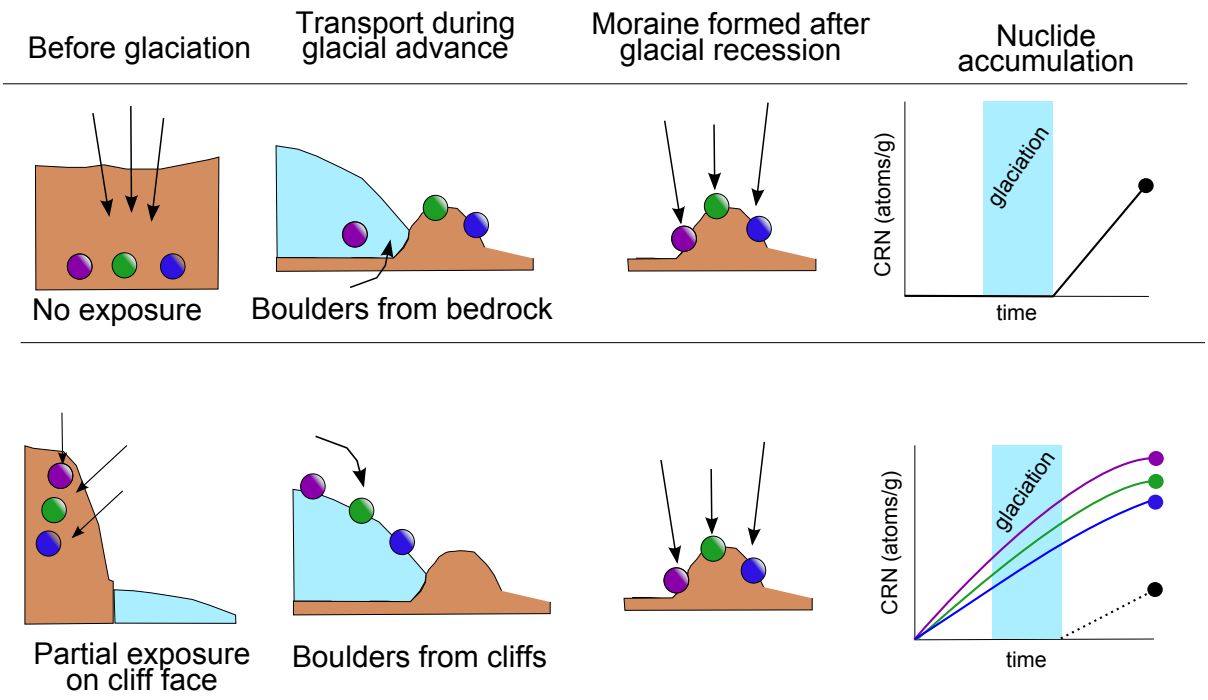

Figure 2.3: The effect of inherited concentration on measured moraine boulder age [recreated from *Ivy-Ochs and Briner* (2014, Fig. 3)]. Top panel: When exposure age dating glacial moraine boulders, one assumes that erosive glacial advance exhumes bedrock never before exposed to cosmic radiation. This bedrock contains no radionuclide concentration accumulated before deposition at the moraine, and all boulders faithfully record the age of moraine formation. Bottom panel: In regions where cold-based glaciation prevails, boulders are not exhumed from buried bedrock, but instead originate in the surrounding cliffs where they have been exposed to cosmic radiation for an indeterminable amount of time. As a result, these boulders contain varying amounts of inheritance, which cause overestimation of moraine age.

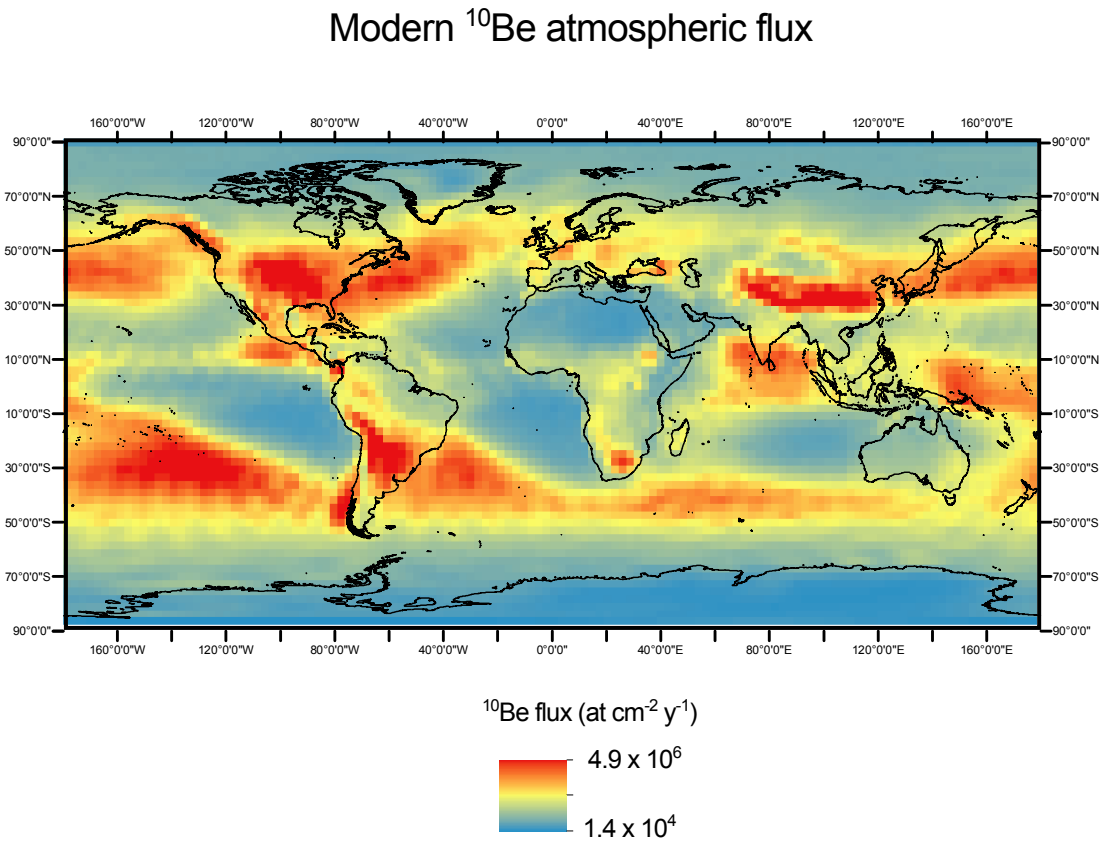

Figure 2.4: Modern ^{10}Be atmospheric flux (*Heikkilä and von Blanckenburg*, 2015). Note that the greatest flux values are found at the mid-latitudes, where mixing between the troposphere and stratosphere is greatest.

CHAPTER 3 : "Difference Dating:" a novel approach towards dating alpine glacial moraines

This manuscript is under review at Quaternary Geochronology. *Co-authors include Jane K. Willenbring and Adam R. Lewis.*

Abstract

The East Antarctic Ice Sheet responds sluggishly to shifts in climate. To capture subtle changes in Antarctic climate, researchers have focused instead on smaller alpine and cirque glaciers that fringe the ice sheet throughout the McMurdo Dry Valleys. The exposure ages of glacial moraine boulders scatter widely and often incorporate large amounts of inheritance, prohibiting the construction of a regional deglaciation chronology. We present a new sampling technique that takes advantage of ubiquitous desert pavements and allows for the detection of inheritance in overlying glacial moraine boulders. Our approach requires a large sample set, but offers increased confidence in modeling moraine age, an acceptable trade-off considering the need for more refined Antarctic paleoclimate reconstructions. Using the beryllium-10 system in sandstone quartz, we show that single exposure ages collected from moraine boulder tops are frequently inaccurate, and consistently over- and underestimate moraine age. Difference Dating offers a new approach to dating alpine glacial moraines independent from traditional boulder exposure age dating.

3.1. Introduction

Since its inception over three decades ago, cosmogenic radionuclide dating has become the glacial geomorphologist's hallmark tool for constructing deglaciation chronologies. A variety of geologic features are targeted to help unravel the timing and duration of glacier ice coverage and range from bedrock to glacial erratics. Perhaps the most common application of exposure dating in periglacial environments is that of moraine boulders, first applied by

Phillips et al. (1990). Because of the boulders' positioning on terminal and lateral moraines, exposure ages correspond to the timing of glacier retreat and, in turn, mark a mass balance adjustment as a result of some transition in climate (e.g., *Gosse et al.*, 1995).

Exposure dating is widely applied throughout the Antarctic continent. Of great interest is understanding the response of the East Antarctic Ice Sheet to climatic forcing, particularly within the context of its potential contribution to global sea level rise. Such studies have focused on the ice sheet's outlet glaciers feeding into the McMurdo Dry Valleys (*Brook et al.*, 1993; *Marchant et al.*, 1994; *Staiger et al.*, 2006b; *Swanger et al.*, 2010). Overall, moraine boulder exposure ages indicate that outlet glaciers have retreated since the Pliocene, with minor fluctuations observed during both global glacials and interglacials (*Brook et al.*, 1993; *Brown et al.*, 1991; *Swanger et al.*, 2011). A sensitive climatic record may exist in high elevation alpine glacier deposits, but these locations have remained largely underutilized because of observed scatter in moraine boulder exposure ages which produce dubious deglaciation chronologies. With this limitation, a new approach to dating glacial moraines is necessary.

We present first results from a novel sampling method that offers an independent moraine dating tool. The "difference dating" technique uses exposure age dating of both moraine boulders and underlying desert pavement clasts. We apply this sampling technique to two moraines in the Leibert Cirque, Olympus Range and demonstrate that only one of four boulders sampled is likely representative of moraine age. This application will prove useful throughout the Dry Valleys where moraine boulders lie atop intact desert pavements. Finally, we suggest future improvements to the technique.

3.1.1. Regional setting

Leibert Cirque lies perched at 1400 masl on the north wall of Wright Valley in the Olympus Range. To the south lies the Labyrinth (*Lewis et al.*, 2006) and to the west Lower Wright Glacier, an outlet glacier draining Taylor Dome of the East Antarctic Ice Sheet. Local bedrock and cirque headwalls are dominantly comprised of Taylor Group sandstones and

Ferrar Dolerite of the Devonian-age Beacon Supergroup (*Turnbull et al.*, 1994). Much of the high elevation Olympus Range exists in the stable upland zone of the Dry Valleys, where extreme aridity and cold temperatures dominate. Precipitation is limited and glacier mass accumulation comes mostly from snow blown off the Polar Plateau (*Marchant and Head*, 2007).

VandenHeuvel (2002) referred to Leibert Cirque as 'Cirque E' and described three prominent alpine moraines within: moraines 1, 2 and 3, referring to distal, intermediate, and most proximal to the headwall in position (1820 m, 1690 m, 1400 m from the headwall, respectively) (see Fig. 3.1). For ease of comparison, we will adopt this nomenclature. The same moraine sequence was noted in adjacent Dean and Dipboye Cirque. We have sampled moraines 1 and 2. Moraines 1 and 2 are arcuate in plan view and parallel to one another; they vary in length (892 m, 922 m) and reach a maximum width in their western portion (3.0, 4.2 m) where they abut patchy exposures of Circe Till (*Lewis et al.*, 2007). Each moraine is dominantly composed of sandstone boulders and <5% dolerite boulders. Corrugated sandstone bedrock outcrops beyond the extent of outer moraine 1. *VandenHeuvel* (2002) attributes moraine formation to the expansion of an alpine glacier at the cirque headwall and invokes the preservation of a desert pavement beneath moraine till as evidence that alpine glaciation was cold-based and non-erosive. Today, all alpine glaciers in the Dry Valleys stable upland zone are cold-based and in equilibrium with the modern climate (*Fountain et al.*, 2016).

3.1.2. Boulder scatter

Moraine boulders sampled for exposure ages produce widely scattered results in the Olympus Range. For example, in Dean and Dipboye Cirques, *VandenHeuvel* (2002) and *Swanger et al.* (2014) measured ^{3}He in dolerite boulders from two moraines and together produced apparent exposure ages which ranged 99-946 ky and 325-1450 ky, ∼142% to >130% different, respectively. We may expect high scatter in ^{3}He datasets because the nuclide is stable, which captures longer exposure histories and thus a higher probability of inheritance. But,

high scatter is also observed in ^{10}Be exposure ages from two alpine moraines on Mount Jason, ∼12 km to the east of Leibert Cirque, where apparent exposure ages ranging 251-527 ky and 1195-2171 ky are as much as ∼70% and ∼60% different, respectively (Valletta, unpublished data). These same data produce reduced chi-square statistics (χ^2_R) $\gg$1, implying data scatter resulting from sources other than measurement error alone (*Balco*, 2011), including inheritance.

Cold-based glacial conditions found in the Olympus Range promote the accumulation of nuclide inheritance. In temperate glacial settings, basal ice above the pressure-melting point slides atop and erodes underlying bedrock, depositing boulders in terminal moraines and exposing them to cosmic radiation for the first time. Conversely, cold-based glaciers are weak erosive agents (*Cuffey et al.*, 2000) because they are largely frozen to underlying bedrock where stress (and basal shearing) reduces to zero; the ice-rock interface remains below the pressure melting point and overlying ice moves via internal plastic deformation only (*Hooke*, 2005). Boulders originate in surrounding cliffs, reach the glacier via rockfall, and travel to the terminal moraine supraglacially, receiving cosmic radiation throughout their entire transport history. This phenomenon is oft noted throughout the Dry Valleys (e.g., *Swanger et al.*, 2011) and the Transantarctic Mountains (e.g. *Hein et al.*, 2014) as the primary driver for observed boulder exposure age scatter.

In regions where inheritance is thought to dominate boulder exposure age scatter, researchers may select the youngest age as most representative. Recent modeling efforts indicate that this practice is often better at estimating the moraine age than the population's median or mean, but that it is not always precise (*Applegate et al.*, 2012).

3.1.3. Desert pavement exposure histories

As an alternative moraine dating technique, we turn to the underlying desert pavement that stretches continuously between and beneath moraines 1 and 2. Desert pavements are armored stone surfaces that create interlocking stone mosaics and lie atop matrices of finer

grained sands (*Cooke*, 1970); they are ubiquitous throughout the Dry Valleys. As many as five mechanisms are recognized for pavement formation and include removal of fines via deflation or overland flow, upward migration of clasts via freeze/thaw, inflation via dust deposition, or degradation via physical and/or chemical weathering (*Bockheim*, 2010).

We assess the exposure histories of the Leibert Cirque pavement in two locations: 1) buried, beneath moraine boulders and 2) exposed, surrounding moraine boulders. We assume these two locations would undergo identical exposure histories were the moraine till never deposited. The boulder's exposure age -if accurate- should account for the difference in pavements' accumulated nuclide inventories. Assuming we can accurately constrain the production rate at each sampled pavement site, we can 1) identify which boulders best reflect true moraine age (if any) and 2) independently estimate moraine age.

In addition, we can use pavement histories to inform on the duration of cold-based glaciation. The lack of post-formational reworking of the Leibert Cirque lag pavement indicates that overriding glacial ice remained cold-based and protected, rather than obliterated, this delicate feature. This has been observed numerous times elsewhere (e.g., *Davis et al.*, 2006; *Kleman and Glasser*, 2007). Thus, we can interpret the apparent exposure age of exposed pavement clasts as the minimum amount of time since cold-based glaciation has dominated.

3.2. Material and Methods

3.2.1. Experimental methods

Four boulder and 44 pavement samples were collected during the austral summer of 2011 for ^{10}Be and ^{26}Al analysis. Each sample's physical characteristics - including luster, iron oxide staining, ventifcation and quartzification - were qualitatively recorded. All radioisotopes were measured in clean quartz aliquots prepared at the University of Pennsylvania Cosmogenic Isotope Lab. We extracted clean quartz from rock using a series of strong acid leaches adapted from established procedures (*Kohl and Nishiizumi*, 1992), including two overnight leaches in 5% HNO_3 and 5% HF on a roller and one overnight treatment in 1%

HNO_3 and 1% HF in a heated sonicator bath. Clean quartz aliquots were subjected to a pure HF etch and Aqua Regia cleansing. Samples were spiked with 250 μl ^{9}Be carrier (Scharlau Be carrier, $^{10}Be/^{9}Be \approx 2 \text{ x } 10^{-15}$), dissolved in pure, heated HF, dried, and converted to chlorinated form via addition of 6 M HCl. 250 μl aliquots were removed from each sample and measured on the in-house ICP-OES for total Al ([^{27}Al]). Chlorinated samples were passed through an anion exchange resin (Bio-rad AG1x8 100-200 mesh) to separate Be and Al, dried, then treated with 0.4 M Oxalic Acid. Be aliquots were passed through a second cation exchange resin once (Bio-rad AG50-X8 200-400 mesh) and Al aliquots and chemical blank (SPEX Al Carrier, $^{26}Al/^{27}Al \approx 5 \text{ x } 10^{-14}$) were passed through a second cation exchange resin twice (Bio-rad AG1-X8 100-200 mesh). All aliquots were precipitated in 1:1 superpure NH_4OH:Milli-Q H_2O, dried in quartz crucibles and oxidized over open flame (>1000 °C). BeO and Al_2O_3 precipitates were homogenized in a 1:3 ratio with Nb and Ag powders (respectively) and packed into clean cathodes for $^{10}Be/^{9}Be$ and $^{26}Al/^{27}Al$ measurement at the Purdue PRIME Lab Accelerator Mass Spectrometer (AMS). ^{10}Be, ^{26}Al concentrations are normalized to 07KNSTD (*Nishiizumi et al.*, 2007) and KNSTD (*Nishiizumi*, 2004) isotope ratio standards, respectively.

3.2.2. Numerical methods

Cosmogenic radionuclides accumulate in eroding geologic surfaces via the following relationship:

$$N(z,t) = N_{inh}(z)e^{-\lambda t} + \frac{P_{sp}(z)}{\lambda + \rho\epsilon/\Lambda_{sp}}\left[1 - e^{-(\lambda+\rho\epsilon/\Lambda_{sp})t}\right] + \int_0^t P_{mu}(z+\epsilon\tau)d\tau \qquad (3.1)$$

where N is a measured concentration of cosmogenic radionuclide (atoms g^{-1}), N_{inh} is the inherited nuclide concentration, λ is the nuclide decay constant (y^{-1}), ρ is density (g cm^{-3}), ϵ is erosion rate (cm y^{-1}), Λ_{sp} is attenuation length (g cm^{-2}), t is time of exposure (y), and P_{sp} and P_{mu} are production rates (atoms g^{-1}) into the subsurface, depth z (cm). We ignore the final term for muogenic production because $P_{mu} << P_{sp}$ and $\rho\epsilon/\Lambda_{sp} << \lambda$.

We report the exposure ages of boulders based on measured nuclide inventories using the updated CRONUS calculator (*Marrero et al.*, 2016) with the 'Sa' scaling scheme and a long term erosion rate of ϵ=10 cm My^{-1} based on locally-derived erosion rates (*Schäfer et al.*, 1999; *Summerfield et al.*, 1999; *Nishiizumi et al.*, 1991; *Ivy-Ochs et al.*, 1995).

As an independent check on the boulder's exposure age, we use desert pavement clasts collected from two locations with unique production rates. This sampling scheme is grounded in the reasoning that, assuming no loss to erosion or decay, the difference in nuclide inventories between two pavement clasts (atoms g^{-1}) is simply the difference in their production rates (atoms g^{-1} y^{-1}) multiplied by the moraine's age (y). We target pavement clasts that are exposed at the surface (N$_{exp}$) and buried beneath a moraine boulder (N$_{bur}$):

$$N_{exp}(t) = N_{inh}(0)e^{-\lambda t} + \frac{P_{sp}(0)}{\lambda + \rho\epsilon/\Lambda_{sp}}(1 - e^{-(\lambda+\rho\epsilon/\Lambda_{sp})t}) \tag{3.2}$$

$$N_{bur}(t) = N_{inh}(0)e^{-\lambda t} + \frac{fP_{sp}(0)}{\lambda}(1 - e^{-\lambda t}) \tag{3.3}$$

where $P_{sp}(0)$ is the production rate at the surface of the pavement. Note that N_{exp} is actively undergoing erosion, but N_{bur} is not. Also note that production at N_{bur} is reduced by a factor of f, the geometric shielding factor imposed by the boulder ($0 \leq f \leq 1$) (see Section 3.2.2.1). To be clear, the inheritance term N_{inh} here refers to nuclide inheritance in each pavement clast (not the boulder). Next, using Eqs. 3.2 and 3.3, we solve for the difference in nuclide inventories, ΔN:

$$\Delta N = \frac{P_{sp}(0)}{\lambda + \rho\epsilon/\Lambda_{sp}}(1 - e^{-(\lambda+\rho\epsilon/\Lambda_{sp})t}) - \frac{fP_{sp}(0)}{\lambda}(1 - e^{-\lambda t}) \tag{3.4}$$

In solving for ΔN, N_{inh} drops out and we can solve for a unique moraine age, t. We will refer to this t value as the "difference date." The following terms have associated uncertainties

which we assume take a Gaussian distribution: P_{sp}, f (see Section 3.2.2.1) and ΔN. To incorporate these uncertainties into our solution, we use a 5000-run Monte Carlo simulation, similar to that presented in *Balco et al.* (2005). Each run uses a randomly selected value from these Gaussian distributions and solves for a unique value of difference date[1]. To satisfy Eq. 3.4 we use the following values: Λ=140 g cm^{-2} (*Borchers et al.*, 2016), λ is 4.99x10^{-7} for ^{10}Be and 9.83x10^{-7} for ^{26}Al (*Korschinek et al.*, 2010; *Chmeleff et al.*, 2010), and unique $P_{sp}(0)$ values at each sample site using elevation scaling factors calculated with the LSD method (*Lifton et al.*, 2014). We again assign a value of ϵ=10 cm My^{-1}; including an uncertainty with ϵ does not alter model results.

If boulder exposure ages accurately depict the timing of moraine formation, then boulder exposure ages should equal difference dates. If not, one of three scenarios is possible: 1) the boulder has underestimated the age of the moraine, 2) the boulder has overestimated the age of the moraine, or 3) the difference date is quantified incorrectly, perhaps due to the inclusion of outliers.

To corroborate these modeling steps, we measure burial ages on a single clast beneath each boulder and on a single exposed clast using Al-Be burial ages (*Granger*, 2006). Burial dating is made possible by the differential rates of decay of two nuclides with non-equal half-lives. To find a unique burial age for each clast, we manuipulate Eq. 3.1 to include both 1) erosion before burial and 2) post-burial production in the absence of erosion:

$$N_j = \frac{P_{sp,j}(0)}{\lambda + \rho\epsilon/\Lambda_{sp}} e^{-(\lambda+\rho\epsilon/\Lambda_{sp})t_b} + \frac{f P_{sp,j}(0)}{\lambda}(1 - e^{-\lambda t_b}) \tag{3.5}$$

where N is the measured concentration of nuclide j (^{26}Al or ^{10}Be) and t_b is burial time. We now have two equations to solve for two unknowns (ϵ, t_b). We solve Eq. 3.5 using the same Monte Carlo scheme described above.

[1]To ensure 5000 runs is sufficient, we plot the standard deviation after each successive run and observe that it converges after ∼2000 runs.

3.2.2.1. Calculating shielding factors

Central to the aforementioned modeling efforts is the proper calculation of f, the geometric shielding factor. To calculate f we use Balco's (2014) MATLAB code for calculating cosmic ray shielding. The code uses Monte Carlo integration to calculate the flux of cosmic radiation received at a near-surface site shielded by geologic obstructions. Individual ray paths incident on the buried pavement sites are partially or completely attenuated as they travel through obstructions (overlying moraine boulders). The mass thickness through which the rays are attenuated is a function of both the obstruction's density and it's linear thickness. The former is measured as the distance through which a ray path traveling at a certain angle must traverse to reach the buried sampling site. The code produces a shielding factor, f, the ratio of the production rate at a shielded site to that at an identically located non-shielded site.

To simulate obstructions, Balco used 360° field photographs and photogrammetric software to generate three-dimensional enclosed spaces termed "shape models." Here, we take advantage of a fortuitously sampled dataset, but one not initially designed with digital shape models in mind. In the absence of 360° photographs of our sampling sites, we develop shape models manually using Meshlab (http://meshlab.sourceforge.net/), a freely available graphics software package. We use a combination of available field photographs and boulder measurements to create a shape model for each sampled boulder and calculate f beneath each boulder's center. The basic mesh of each boulder is an icosphere, a spherical mesh made via the subdivision of icosahedron faces, which is then deformed to fit measured dimensions (see Supplemental Information, Fig. S1). Though this approach smooths out fine-scale features on the boulder face, we are most concerned with properly rendering the maximum vertical height of each boulder because the maximum intensity of incident radiation is strongly concentrated near the vertical (*Gosse and Phillips*, 2001). Changing the overall shape of the boulder does not significantly affect f so long as the maximum vertical scale is maintained. However, f is very sensitive to the maximum vertical height

for boulders ∼1 m tall. We run the script three times on each shape model and average the resulting f values. Each buried location is associated with a single f. Note that boulder OLY-38 was too large to overturn and buried sites OLY-36 and OLY-37 were collected from smaller boulders immediately adjacent to OLY-38; see Fig. 3.2. Based on these boulders' orientation, we assume that all boulders were deposited simultaneously.

Because we do not use an automated, digitally-derived shapefile, we must incorporate some human-induced uncertainty associated with measuring boulder heights in the field and via photographs. We assign a conservative error of ±10 cm in boulder height measurements. For boulders ≤70 cm tall, this error corresponds to $< 10\%$ of f and for larger boulders ≥100 cm tall this error increases to ≤30%. This is to be expected as f increases exponentially with increasing shielding thickness (see Balco, 2014, his Fig. 4).

3.3. Results

3.3.1. Radionuclide measurements

3.3.1.1. ^{10}Be

We measured ^{10}Be in 48 samples (4 sandstone boulder surfaces and 44 pavement clasts) in 5 total batches; see Table 3.1. Chemical blanks processed with each batch registered 2.91 ± 0.86, 3.18 ± 1.59, 8.77 ± 1.58, 33.2 ± 4.60, and 32.0 ± 5.75 x10^4 ^{10}Be atoms g^{-1}. Despite relatively high blank measurements, near-saturated sample concentrations ensure low overall contributions of blank contamination to sample ^{10}Be. Most blank concentrations represent ≪1% of sample concentration. In three samples (OLY-26-P3, OLY-31-DP3, and OLY-33-DP7) the blank concentration represented >2% of total ^{10}Be atoms (2.72%, 2.04%, and 3.67%, respectively). All OLY-26 clasts are discarded as outliers; see Section 3.3.1.3. Samples OLY-31-DP3 and OLY-33-DP7 fall within error of their site's sample populations and are deemed acceptable. A single sample, OLY-36-DP4 registered a low ^{9}Be beam count on the AMS. It is included in Table 3.1 for reference, but is excluded from analysis.

We note that those clasts with lower-than-average [^{10}Be] exhibit retention of fine surface topographies and lack well-developed iron oxide staining and greasy luster siliceous crusts. This is true of all samples collected at site OLY-26 and boulder surfaces. Samples with more physical evidence of ventifaction and quartzification register greater [^{10}Be], an observation also made on dolerite clasts (*Staiger et al.*, 2006b; *Swanger et al.*, 2011); see Fig. 3.3.

3.3.1.2. ^{26}Al

We measured ^{26}Al in 5 samples, 4 of which were buried beneath moraine boulders. The chemical blank returned a ratio of $0.00 \pm 1.18\ 10^{-13}\ ^{26}\mathrm{Al}/^{27}\mathrm{Al}$ indicating negligible contributions of ^{26}Al during lab processing.

3.3.1.3. Outlier exclusion

Properly identifying outliers in this scattered dataset is crucial to our approach. Ideally, a robust statistical criteria could be used to reject outliers, e.g. Chauvenet's criterion (*Rinterknecht et al.*, 2006). However, the logistics of our sampling method limit us to a rather small dataset collected at each site; there are only so many pavement clasts that lie beneath each overturned boulder. Accordingly, we are limited to a quasi-quantitative approach to identify and reject outliers. For a discussion on outlier treatment, we refer the reader to *Balco* (2011).

We use simple methods to help visualize the spread in the dataset, the first of which are kernel density estimates (also referred to as "camelplots"). In this type of plot, we represent each measurement by a single PDF using a Gaussian distribution normalized by the total number of samples. All sample PDFs are summed together, forming the kernel density estimate which peaks in a region near some "true" value; see Fig. 3.4. Most typically, exposure ages are used to construct PDFs, but here we represent each PDF with a mean, μ=^{10}Be measurement, and a standard error, σ=^{10}Be measurement error. Kernel density estimates clearly show the clustering of pavement clasts between 30-38 Matoms g^{-1}. Two samples register >40 Matoms g^{-1} and most other scattered samples fall between 15-30

Matoms g^{-1}; these samples may represent improperly sampled moraine material. They are removed from analysis. Seven samples register <10 Matoms ^{10}Be and are of the same order as overlying boulders' [^{10}Be]. As such, these samples are interpreted as spalled boulder chunks and removed from analysis. Plotting the cumulative distribution function of all pavement clasts at each moraine provides an additional method for visualizing the identified outliers and confirms our selection; see Fig. 3.5.

3.3.2. Exposure ages and model results

^{10}Be measured on exposed clasts produce minimum exposure durations that range 2.6 to 5 My, and average 4.2 My. Several clasts register saturated concentrations, likely reflecting production at higher elevations before delivery to the cirque floor.

Each moraine boulder's shielding factor (f) and apparent exposure age is listed alongside the underlying pavement's difference date and Al-Be burial age in Table 3.2. At each site, we first removed outliers from the measurement datasets before solving for the difference date. [For all sites, N_{exp}=35.52±1.97 Matoms g^{-1}, the mean concentration of exposed pavement clasts (n=9). N_{bur} is unique to each buried site.] See Fig. 3.6 for a comparison of all difference dates with boulder top exposure ages.

3.3.3. Outer moraine 1

At outer moraine 1, site I, the boulder's apparent exposure age is 416±9.5 (75) ky. All pavement samples beneath the site I boulder are discarded as outliers and we cannot test the validity of this exposure age.

At outer moraine 1, site II, the boulder's apparent exposure age is 288±4.5 (48) ky. The corresponding difference date is 318±64 ky, comparable to its Al-Be burial age of 362±316 ky. The agreement amongst the site II boulder exposure age, difference date, and burial age leads us to the conclusion that outer moraine 1 is likely closer to its difference date of 318±64 ky. We select the difference date, rather than the boulder exposure age, because it is better

constrained with multiple buried (n=4) and exposed (n=9) pavement clasts, compared to the boulder's single measurement. This conclusion supports the notion that the site I boulder overestimates the age of moraine 1 and likely contains inheritance. Simultaneously, this conclusion supports the notion that the site II boulder may slightly underestimate the age of moraine 1, perhaps due to boulder spalling events.

3.3.4. Inner moraine 2

At inner moraine 2, site III, the boulder's exposure age is 393±8 (67) ky, older than its corresponding difference date of 366±90 ky. This discrepancy is likely due to inheritance in the site III boulder. We did not measure an Al-Be burial age at this site.

At inner moraine 2, site IV, the boulder top exposure age is 93±1.5 (15) ky, significantly less than its two corresponding difference dates of 149±46 ky and 164±42 ky. The slight disagreement between the two difference dates at site IV may be the result of an inaccurate estimation of f. Al-Be burial ages register 85±334 ky and 189±253 ky, in broad agreement with the difference dates.

Assuming the pavement formed in a spatially uniform manner, difference dates measured at both sites III and IV should match, but they do not. We attribute this to site III data, where all pavement clasts except one are excluded as outliers. This single clast (OLY-33-DP10) registers N_{bur}=32.4±1.0 Matoms g^{-1}, a value that is lower than other moraine 2 buried sites OLY-36 (N_{bur}=34.31±0.25 Matoms g^{-1}) (n=7) and OLY-37 (N_{bur}=33.72±0.28 Matoms g^{-1}) (n=5). Lower N_{bur} values have the overall effect of increasing the calculated difference date and likely results in an erroneous age.

Based on the mean difference dates at site IV, we assign inner moraine 2 an age of ∼157 ky. Similar to outer moraine 1, we find that the difference dating exercise at inner moraine 2 indicates moraine boulder exposure ages can both over- and underestimate moraine age.

3.3.4.1. Additional Al/Be results

Despite large uncertainties, sites' II and IV Al-Be burial ages agree with their corresponding difference dates. More precise burial ages may be obtained using burial isochron dating on larger datasets, especially when incorporating Bayesian treatments (*Muzikar*, 2011).

The Al/Be isotope ratios contain further information; see Fig. 3.7. First, note that all samples cluster near saturation except OLY-26-DP4, giving us more confidence that this sample is likely an outlier and that excluding it and samples of similar concentration from analysis was appropriate. Secondly, we note that the single exposed sample, OLY-32-DP5, is saturated with respect to Al and very near saturation with respect to Be. All other buried samples plot near to and below OLY-32-DP5 in the burial zone. This suggests that buried samples traveled along the constant-exposure line towards saturation (much like OLY-32-DP5) until they were buried by moraine till. Thus, a single stage exposure-burial history is sufficient to explain buried clasts' location on the erosion-island plot. Finally, we calculate a steady-state erosion rate from the single exposed pavement sample of 4 ± 3 cm My^{-1}, a value in excellent agreement with published regional erosion rates.

3.4. Discussion

3.4.1. Difference Dating: future directions

Moraine difference dates indicate that only a single moraine boulder of the four sampled may represent true moraine age. We posit that Leibert Cirque moraines 1 and 2 are ∼318 ky and ∼157 ky, respectively. We observe that when boulders do not explain pavement exposure histories, they can either over- or underestimate moraine age. While the literature is rich with instances of moraine boulder inheritance producing ages that are too old, the occurrence of ages that are too young is not as frequently observed in the Dry Valleys [save instances of diffusive loss of ^{3}He from quartz (*Brook et al.*, 1993)]. We regard it as most likely that sandstone boulders are subject to random spalling events, resulting from thermal fracturing and freeze/thaw processes, which shed exterior boulder surfaces con-

taining high radionuclide concentrations. This argument is also invoked to explain boulder scatter in Taylor Glacier deposits (*Swanger et al.*, 2011). The observation of pavement clasts containing [^{10}Be] concentrations of the same magnitude as boulder tops supports this hypothesis.

Our initial Difference Dating results are encouraging and, with future improvements, the technique could essentially replace boulder exposure age dating in appropriate settings. The primary goal of future applications should be to incorporate multi-nuclide systems so as to minimize age uncertainty. In this study, the relative share of uncertainty alters slightly between sample sets, but is consistently dominated by nuclide measurement uncertainties. For all locations, a simple error analysis reveals that $\sigma\Delta N$ contributes the most to overall uncertainty in the difference date (ranging from 42% to as much as 83%), followed by σf (ranging 10% to 34%), and finally by σP (ranging 7% to 28%). Reducing $\sigma\Delta N$ will result from larger sample sets (though this may not always be possible), precise laboratory processing (though our average process blank result is acceptable at $\sim$0.8% total ^{10}Be atoms, it can be improved), and application to more tightly constrained nuclide systems (e.g., ^{3}He). Negligible contributions from σf can be achieved simply by using automated shapefile creation. Reduction in σP is more challenging, but may be possible if Difference Dating is applied near production rate calibration sites, such as the exposed bedrock features in Arena Valley (*Balco and Shuster*, 2009).

Like boulder exposure age dating, the Difference Dating technique is suitable to a range of target minerals/isotope systems. The method requires greater physical disturbance of moraine deposits and more challenging sampling efforts, but offers a moraine age estimate unaffected by potentially overwhelming inheritance issues. Difference Dating can be validated in future studies using isochron burial dating in the buried pavement clasts, provided production rates can be properly constrained at each buried and exposed location. Quartz sands underlying the pavement clasts may represent an additional target for Difference Dating.

3.4.2. Paleoclimatic inferences

The average exposure age of the desert pavement indicates that cold-based glaciation has endured for >4.2 My. This is in agreement with regional climatic records that place the onset of hyperaridity and cold-based glaciation well before that at ∼14 My (e.g., *Lewis et al.*, 2007, 2006; *Valletta et al.*, 2015).

Difference dates indicate glacial advance during marine isotope stages 6 and 9. Evidence for concurrent glacial advance during both stages is found throughout the Dry Valleys (*Higgins et al.*, 2000; *Swanger et al.*, 2011; *Brook et al.*, 1993; *Brown et al.*, 1991). Though, correlating distant glacial deposits which may reflect valley-wide climatic signals is likely precluded by the complex nature of glacial behavior here, which is strongly controlled by localized wind patterns and solar radiation (*Hoffman et al.*, 2016). Ideally, comparative difference dates could be collected from the Wright Valley cirques conjoining Leibert, and others throughout the Olympus Range. While our outermost moraine 1 age seems to agree with *VandenHeuvel* (2002)'s minimum exposure age collected on a correlated moraine sequence in Dean Cirque (325±15 ky), our moraine 2 age exceeds his youngest corresponding age (99±12 ky). In DipBoye Cirque, the youngest ages from moraines 1 and 2 both exceed our moraine ages (421±6 ky and 386±5 ky, respectively) (*Swanger et al.*, 2014). This mismatch again highlights that moraine boulder exposure ages are highly unlikely to reflect true moraine age in high elevation alpine deposits, that moraine boulders may both over- or underestimate true moraine age, and the need for an alternative moraine dating method is great.

3.5. Conclusions

We present a method for confirming the exposure age of moraine boulders that lie atop intact desert pavement surfaces. In the field, sampling logistics may be complicated by physical limitations; boulders must be small enough to overturn. Extreme care must be made while sampling so as to not incorporate moraine lag. This is not always possible because pavement

clasts may exceed the age at which quartz rinds and ventifaction become well-developed. In this case, samples must be rejected as outliers following isotope measurement, a relatively straight-forward procedure. The Difference Dating technique would lend itself well to paired isotope systems in which isochron burial dating is possible.

Ongoing work looks to improve our method and expand the deglaciation chronology recorded in high-altitude cirque glacier deposits. Recent fieldwork has sampled the corresponding moraine sequence in DipBoye Cirque with the intention of implementing the Difference Dating technique. Accordingly, proper field photographs were taken to produce automated shapefiles, a more reliable approach to calculating shielding factors at each site.

ACKNOWLEDGMENTS: Funding for this work was provided by NSF Collaborative Research grant 1043554. We thank Greg Balco and Brent Goehring for their thoughtful commentary which greatly improved this manuscript.

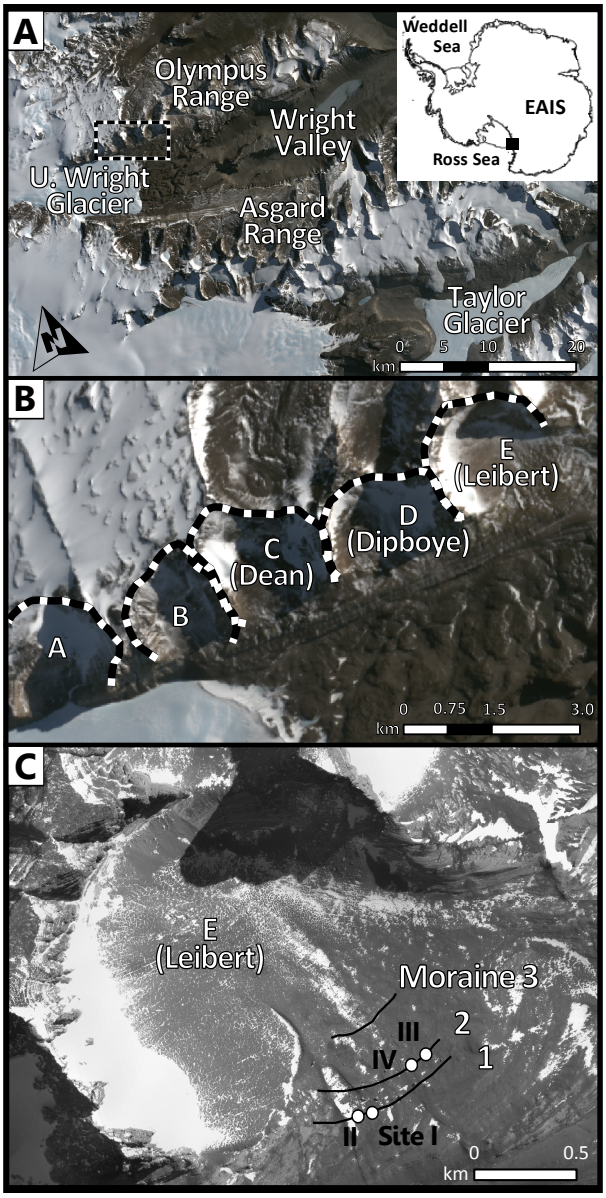

Figure 3.1: Sampling location. A: Overview of Wright Valley region (Landsat 8). B: Inset of box A. Sequence of five cirques on the northern wall of Wright Valley. C: Sequence of moraines 1-3 in Leibert Cirque (E) (WorldView).

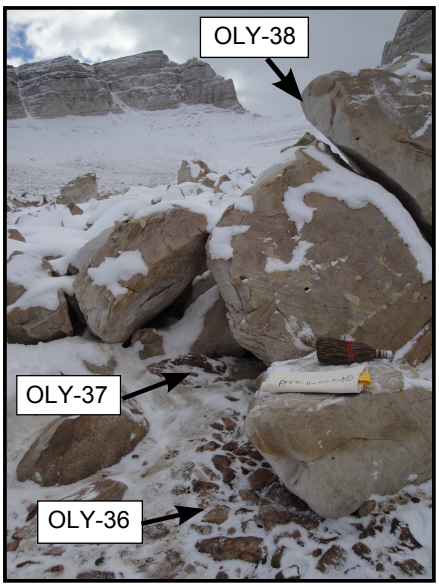

Figure 3.2: Example of sampling site. Pictured: OLY-36, -37, and -38. Note sub-vertical cliffs composed of Beacon Supergroup sandstone in the background. Moraine boulders are likely sourced from these cliffs during rockfall events. In the foreground, note boulder OLY-38 (maximum height: 125 cm tall) which has fractured in place and overlies an intact desert pavement. Site OLY-37 (not visible) lies beneath the fractured, 90 cm tall segment of OLY-38. The foremost, smaller boulder (maximum height: 30 cm) has been rolled away to reveal site OLY-36.

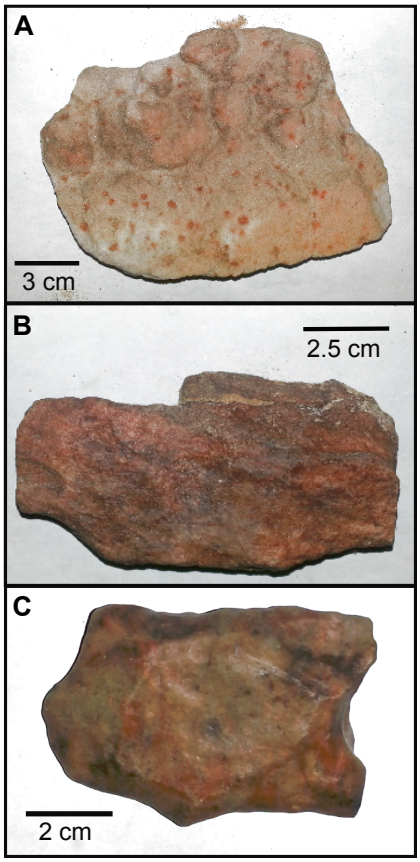

Figure 3.3: Samples representing progressive stages of ventifaction and quartzification. A: OLY-26-P5. Pavement clasts collected from site OLY-26 retain granular surficial grooves and lack a greasy surface luster and quartz rind. Red-orange stains are patchy. B: OLY-33-DP6. Granular appearance is replaced by a thin <0.1 cm thick quartz rind, no clear ventifacted facets are apparent yet. Red-orange staining covers entire clast. C: OLY-31-DP5. The surface of most exposed pavement clasts are strongly ventifacted and characterized by a greasy surface luster, red-orange staining, and impermeable rinds up to $\leq$0.5 cm thick. All images are digitally brightened.

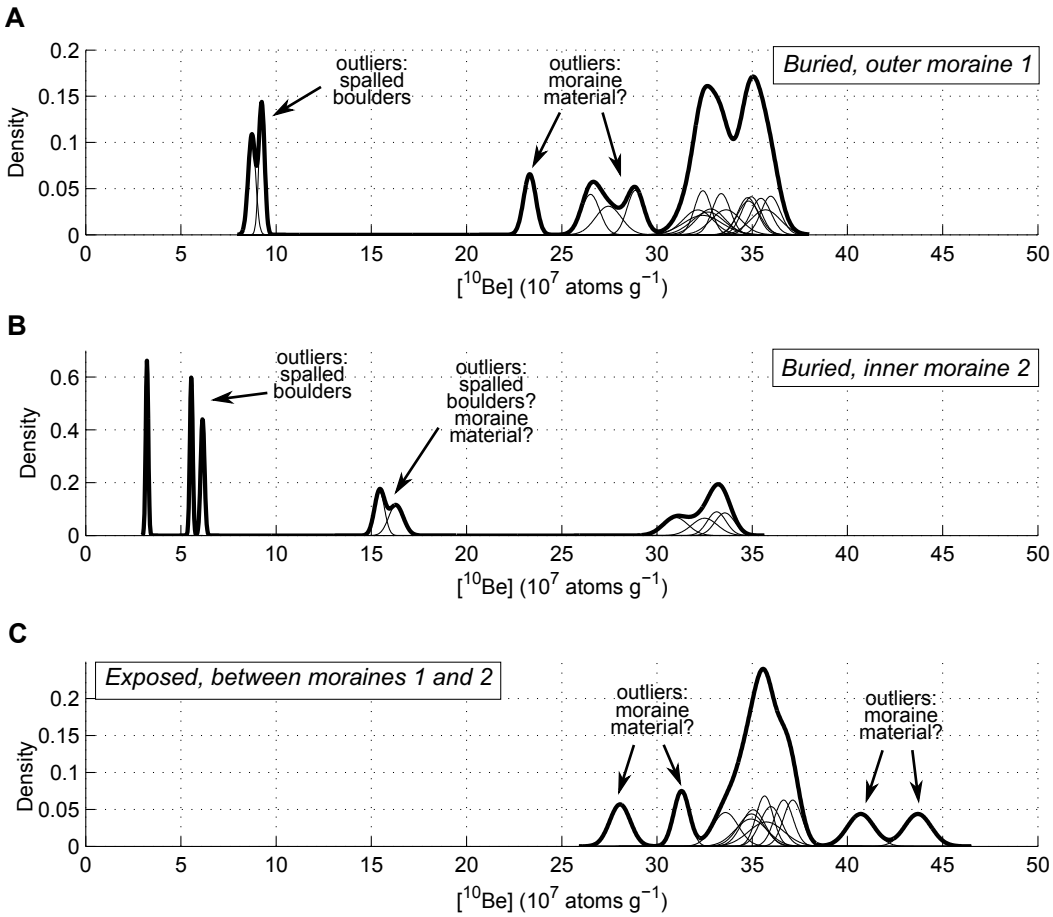

Figure 3.4: Kernel density estimates of pavement clasts buried beneath outer moraine 1 (panel A) and inner moraine 2 (panel B), and exposed pavement clasts collected between the two moraines (panel C). Each clast's ^{10}Be measurement (μ) and uncertainty (σ) are plotted as Gaussian distributions and summed to form a kernel density estimate normalized to an area of one (bold line).

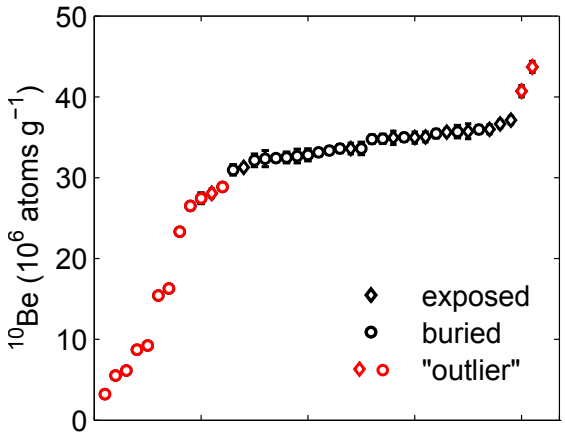

Figure 3.5: The cumulative distribution function for all pavement clasts, buried (circles) and exposed (diamonds). Outliers are identified via kernel density estimate plots and are plotted here in red.

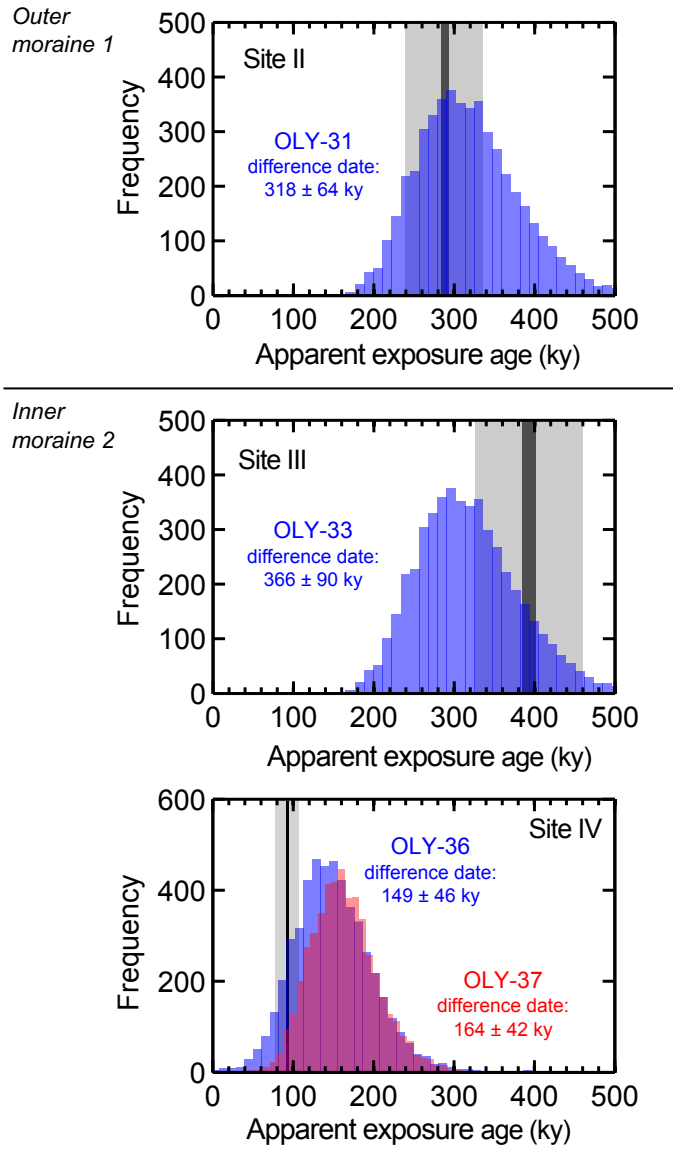

Figure 3.6: Histograms depicting results of the Monte Carlo simulation carried out at sampling sites II, III and IV. Measured exposure ages of each boulder are plotted as vertical lines with experimental (black) and overall (gray) uncertainties.

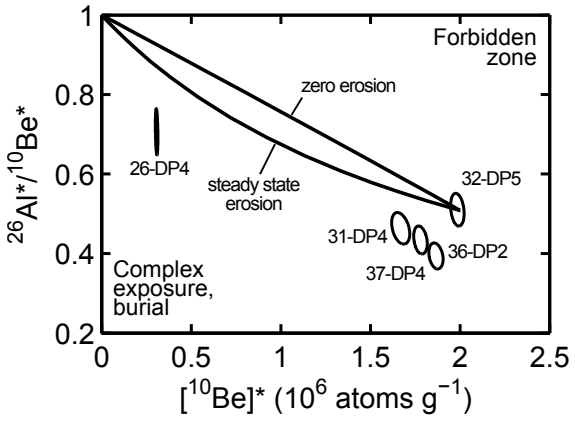

Figure 3.7: Al/Be erosion-island plot. The exposed sample, OLY-32-DP5, corresponds to a steady-state erosion rate of 4 $\pm$ 3 cm My^{-1}. The position of OLY-26-DP4 relative to other buried samples confirms it is an outlier. All other buried samples plot near to and below a single exposed sample OLY-32-DP5, supporting our interpretation of the pavement's exposure history. That is, constant exposure until emplacement of glacial moraines.

Location	Field ID	Sample type[a]	Nuclide	Quartz mass (g)	Thickness (cm)	Concentration (10^6 atoms g^{-1})
Outer moraine 1						
	OLY-27-B	boulder	^{10}Be	20.18	3.0	6.53 ± 0.13
Site I	OLY-28-DP	exposed	^{10}Be	30.83	5.0	21.13 ± 0.34
(-77.5094, 160.9412)	OLY-26-DP3	buried	^{10}Be	19.68	1.9	3.22 ± 0.07
1406 masl	OLY-26-DP4	buried	^{10}Be	22.12	2.5	6.14 ± 0.10
			^{26}Al			30.52 ± 1.71
	OLY-26-DP5	buried	^{10}Be	22.73	1.9	5.54 ± 0.07
	OLY-30-B	boulder	^{10}Be	19.10	3.0	4.83 ± 0.07
	OLY-29-DP	exposed	^{10}Be	24.34	5.0	27.37 ± 0.34
	OLY-31-DP1	buried	^{10}Be	26.88	3.5	33.56 ± 0.52
Site II	OLY-31-DP2	buried	^{10}Be	29.04	1.3	15.43 ± 0.27
(-77.5095, 160.9395)	OLY-31-DP3	buried	^{10}Be	10.22	1.6	16.29 ± 0.38
1397 masl	OLY-31-DP4	buried	^{10}Be	18.89	1.3	30.97 ± 0.65
			^{26}Al			108.40 ± 6.02
	OLY-31-DP5	buried	^{10}Be	25.08	1.9	32.50 ± 0.68
	OLY-31-DP6	buried	^{10}Be	12.79	2.3	33.13 ± 0.49
Inner moraine 2						
	OLY-34-B	boulder	^{10}Be	23.18	1.7	6.52 ± 0.12
	OLY-32-DP1	exposed	^{10}Be	19.89	3.8	43.70 ± 0.70
	OLY-32-DP2	exposed	^{10}Be	27.17	3.0	34.94 ± 0.83
	OLY-32-DP3	exposed	^{10}Be	20.91	3.2	40.71 ± 0.69
	OLY-32-DP4	exposed	^{10}Be	29.26	6.4	33.60 ± 0.67
Site III	OLY-32-DP5	exposed	^{10}Be	23.40	2.5	36.65 ± 0.49
(-77.5076, 160.9571)			^{26}Al			138.6 ± 7.73
1426 masl	OLY-32-DP6	exposed	^{10}Be	30.93	4.7	35.6 ± 0.4
	OLY-33-DP1	buried	^{10}Be	24.99	7.0	9.25 ± 0.15
	OLY-33-DP6	buried	^{10}Be	18.41	2.3	23.32 ± 0.32
	OLY-33-DP7	buried	^{10}Be	24.76	3.2	8.73 ± 0.19
	OLY-33-DP8	buried	^{10}Be	29.76	2.5	26.51 ± 0.48
	OLY-33-DP9	buried	^{10}Be	16.48	1.9	27.45 ± 0.68
	OLY-33-DP10	buried	^{10}Be	9.97	3.1	32.4 ± 1.0
	OLY-38-B	boulder	^{10}Be	24.87	2.0	1.65 ± 0.03
	OLY-35-DP1	exposed	^{10}Be	29.76	1.9	31.29 ± 0.41
	OLY-35-DP2	exposed	^{10}Be	33.78	2.5	34.96 ± 0.70
	OLY-35-DP3	exposed	^{10}Be	28.41	1.3	35.05 ± 0.62
	OLY-35-DP4	exposed	^{10}Be	30.95	1.9	28.06 ± 0.54
	OLY-35-DP5	exposed	^{10}Be	30.41	1.9	35.74 ± 0.93
	OLY-35-DP6	exposed	^{10}Be	32.09	1.3	35.98 ± 0.57
	OLY-35-DP7	exposed	^{10}Be	32.69	3.2	37.13 ± 0.49
Site IV	OLY-36-DP1	buried	^{10}Be	30.30	3.8	35.70 ± 0.78
(-77.5077, 160.9564)	OLY-36-DP2	buried	^{10}Be	31.50	3.8	33.4 ± 0.5
1426 masl			^{26}Al			110.50 ± 6.13
	OLY-36-DP3	buried	^{10}Be	31.49	3.8	34.81 ± 0.58
	OLY-36-DP4	buried	^{10}Be	30.82	3.2	17.58 ± 3.69
	OLY-36-DP5	buried	^{10}Be	31.93	5.1	35.46 ± 0.53
	OLY-36-DP6	buried	^{10}Be	29.46	1.9	32.15 ± 0.78
	OLY-36-DP7	buried	^{10}Be	23.94	1.9	32.68 ± 0.85
	OLY-36-DP8	buried	^{10}Be	29.89	2.5	35.97 ± 0.50
	OLY-37-DP1	buried	^{10}Be	27.54	1.3	34.95 ± 0.51
	OLY-37-DP2	buried	^{10}Be	29.85	2.0	32.83 ± 0.75
	OLY-37-DP3	buried	^{10}Be	31.03	3.5	32.41 ± 0.44
	OLY-37-DP4	buried	^{10}Be	28.44	1.3	34.77 ± 0.52
		buried	^{26}Al			105.20 ± 5.95
	OLY-37-DP6	buried	^{10}Be	29.21	2.5	28.87 ± 0.44
	OLY-37-DP7	buried	^{10}Be	16.94	2.0	33.62 ± 0.78

Table 3.1: Cosmogenic radionuclide data

[a]Desert pavement clasts are designated as 'buried' (beneath that site's corresponding boulder) or 'exposed.'

Location	Field ID	Shielding factor, f	Boulder top exposure age (ky)[1]	Difference date (ky)	Al-Be burial age (ky)
Site II	OLY-31	0.35 ± 0.06	288 ± 4.5 (48)	318 ± 64	362 ± 316
Site III	OLY-33	0.41 ± 0.05	393 ± 8.1 (68)	366 ± 90	-
Site IV	OLY-36	0.48 ± 0.02	93 ± 1.5 (15)	149 ± 46	85 ± 334
	OLY-37	0.29 ± 0.08	93 ± 1.5 (15)	164 ± 42	189 ± 253

[1] internal (external) uncertainty

Table 3.2: Monte Carlo model results and shielding factors

CHAPTER 4 : $^{10}Be/^{9}Be$ ratios reflect East Antarctic Ice Sheet mass changes: a record offshore the Wilkes Subglacial Basin

This manuscript is in preparation for submission to Paleoceanography. *Jane K. Willenbring, Sandra Passchier, and Chiara Elmi are co-authors.*

Abstract

Meteoric radioactive ^{10}Be is produced in the upper atmosphere and deposited on the Antarctic Ice Sheets through time. Along glaciated margins, authigenic ^{10}Be normalized to its stable isotope ^{9}Be reflects changes in ice sheet mass, whereby periods of pulsed warming release ^{10}Be stored within the ice sheet, but chemical liberation of ^{9}Be is limited. We present a record of Be isotopes measured on glaciomarine sediments collected from IODP core U1361a glacial/interglacial intervals of the mid-Pliocene warming, ~5.5-3.5 My. The $^{10}Be/^{9}Be$ ratio is strongly correlated with geochemical and sedimentological trends throughout the core, implying that the environmental signal dominates over the atmospheric production signal here. We interpret fluctuations in the $^{10}Be/^{9}Be$ record as a proxy for freshwater discharge. The age and location of the sediments is useful towards monitoring East Antarctic Ice Sheet melting under mildly warmer temperatures in the Wilkes Land, a region potentially susceptible to major melting due to its low-lying, inward-dipping topography. Additionally, the position of our record directly underlying a zone of deep water formation allows us to examine the delivery of Be directly into Antarctic Bottom Waters.

4.1. Introduction

Meteoric, radioactive ^{10}Be is produced in the upper atmosphere via spallogenic reactions between secondary cosmic radiation and atmospheric oxygen and nitrogen (*Lal and Peters*, 1967). ^{10}Be will rapidly homogenize over 1-2 y in the atmosphere, smoothing out latitudinal differences in high atmosphere production rates (*Raisbeck et al.*, 1981; *Heikkilä et al.*,

2013). Wet (rain, snow) and dry (dust) deposition scavenge ^{10}Be from the atmosphere, delivering it to exposed terrestrial surfaces, the open ocean and ice sheets (*Willenbring and von Blanckenburg*, 2010a). When delivered to the ocean boundaries via riverine transport, the dissolved ^{10}Be load is scavenged from the water column with a particular affinity for aluminosilicates (*Sharma et al.*, 1987; *Frank et al.*, 2000) and biogenic opal (*Chase et al.*, 2002; *Lal et al.*, 2006).

Due to its sensitivity to changes in atmospheric production, particle flux, and bioproductivity, ^{10}Be is the focus of numerous geophysical and ocean geochemical studies for its flexible application as a proxy for geomagnetic field strength in ice cores and marine sediments (*Steig et al.*, 1995; *Yiou et al.*, 1997; *Aldahan and Possnert*, 2003; *Raisbeck et al.*, 2006; *Christl et al.*, 2010), sea ice extent and ice shelf coverage (*Frank et al.*, 2008; *Yokoyama et al.*, 2016), and freshwater discharge from melting ice (*Simon et al.*, 2016). When normalized to its stable isotope ^{9}Be, the ratio is proposed as a faithful recorder of deep ocean circulation patterns (*von Blanckenburg et al.*, 1996) and continental sedimentation to deep marine basins on coarse timescales (*Willenbring and von Blanckenburg*, 2010b; *von Blanckenburg and Bouchez*, 2014; *von Blanckenburg et al.*, 2015).

4.1.1. ^{10}Be in Antarctic marine sediments

Due to its long half-life ($t_{1/2}$=1.39 x 10^6 y) (*Chmeleff et al.*, 2010; *Korschinek et al.*, 2010), ^{10}Be could prove a useful tracer of continental ice sheet dynamics throughout the last 10-12 My, a timespan well-exceeding the limits of traditional particle reactive radionuclides ^{230}Th ($t_{1/2}$=7.5 x 10^4 y) and ^{231}Pa ($t_{1/2}$=3.2 x 10^4 y). Around Antarctica, few marine authigenic ^{10}Be records exist. In the Weddell Sea, *Frank et al.* (1995) document increased ^{10}Be concentrations positively correlating with ^{230}Th sediment fluxes and biogenic barium during global interglacials. They attribute increases in ^{10}Be concentrations in fine grained sediments to a combination of sediment focusing and scavenging by biogenic particles. In a later study, *Frank et al.* (2002) measured depth profiles of dissolved ^{10}Be in seawater showing that the isotope acts as a semi-conservative water mass tracer, and that while

shallow water ^{10}Be is strongly affected by scavenging processes, bottom water ^{10}Be remains unaltered, advecting conservatively beneath zones of high particle flux.

Sjunneskog et al. (2007) measure Be isotopes adsorbed on glacial, glacial marine and open marine sediments from the Ross Sea. They use Be isotope fluctuations to identify changes in lithological units, otherwise made difficult by subtle differences in sediment characteristics. In general, they show that those sediments sourcing subglacial troughs and liberated via ice sheet basal erosion are comparatively depleted in ^{10}Be, while younger, postglacial sediments contain 100-fold more ^{10}Be. *Yokoyama et al.* (2016) describe the same pattern, suggesting that greater concentrations of ^{10}Be accumulated under open marine conditions when ocean temperatures were too warm for established ice shelf and sea ice cover and increased ^{10}Be fallout could reach the open ocean's surface. *Scherer et al.* (1998) make a similar argument from diatom-bearing Quaternary sediments underlying the Whillans Ice Stream. They argue against ^{10}Be sourcing from melting ice and pointed to low ($\ll 10^6$ atoms g^{-1}) ^{10}Be concentrations in pre-Quaternary glacial tills as evidence of such.

All of these records present absolute ^{10}Be concentrations only, which are known to respond to the aforementioned factors, and others, that may change through glacial-interglacial transitions, such as grain size and mineralogy. As an alternative, we employ the ^{10}Be/^{9}Be ratio measured on the authigenic mineral fraction, which corrects for all of these potentially troublesome effects (*Bourles et al.*, 1989).

Globally, deep marine ^{10}Be/^{9}Be records indicate negligible fluctuations throughout glacial-interglacial transitions (*Willenbring and von Blanckenburg*, 2010b; *von Blanckenburg et al.*, 2015), suggestive of negligible changes in global weathering throughout the Cenozoic. Records closer to continental edges, at finer sampling resolutions, indicate a sensitive response in ^{10}Be/^{9}Be to ice mass changes (e.g., *Eisenhauer et al.*, 1994; *Simon et al.*, 2016). The primary goal of this study is to test the application of authigenic ^{10}Be/^{9}Be as proxy for East Antarctic Ice Sheet (EAIS) melt throughout glacial-interglacial intervals. To do so, we analyze the covariation of authigenic ^{10}Be/^{9}Be with geochemical proxies for EAIS fluctua-

tion (ε_{Nd}, $^{87}Sr/^{86}Sr$), biological productivity (opal $\%_{wt}$, Ba/Al) and other sedimentological characteristics (grain size, surface area, mineralogy). We posit that the greatest control on $^{10}Be/^{9}Be$ variation is due to pulses of freshwater discharging from the EAIS during interglacials.

4.2. Setting

We select the IODP U1361a site for $^{10}Be/^{9}Be$ sampling due to its proximity to the EAIS: close enough to monitor its fluctuations, yet far enough away such that ice sheet grounding events have not disrupted the sedimentary record since deposition. The Wilkes Land region of the EAIS is of particular interest because its low-lying, inward dipping topography may make it vulnerable to major ice mass loss under mild warming (*Escutia et al.*, 2011). Though previous models indicate minimum ice mass change in the Wilkes Land region under Pliocene warming (*Dolan et al.*, 2011; *Hill et al.*, 2007; *Pollard and DeConto*, 2009), more recent efforts incorporating hydrofracturing and ice cliff failure dynamics indicate significantly greater losses (*Pollard et al.*, 2015).

IODP core U1361a is collected from the continental rise, ∼310 km offshore the Wilkes Land Subglacial Basin, at ∼3500 m water depth. Located on a submarine channel levee ∼195 m above channel thalweg, the site receives sediments that are fine-grained components of turbidity flows, hemipelagic fallout, and dispersed sediments from bottom currents (*Escutia et al.*, 2005). *Cook et al.* (2013) describe a 75-m long continuous record of Pliocene sedimentation (long term sedimentation rate of 25 m My^{-1}) (*Escutia et al.*, 2011), with alternating units of interglacial, diatom-rich clays (max opal = 45.1$\%_{wt}$) and glacial, diatom-bearing silty clays (max opal = 22.6$\%_{wt}$).

Cook et al. (2013) note that interglacial sediments, deposited under warm, bioproductive regimes, correspond with bulk sediment geochemistry indicative of a retracted ice sheet. Highly radiogenic ε_{Nd} values are interpreted as provenance indicators of the subglacial Ferrar Large Igneous Province some 500 km inland *Ferraccioli et al.* (2009), while less

radiogenic values are more indicative of lower Paleozoic granitoids cropping out along the coastal region (and vice versa for $^{87}Sr/^{86}Sr$ values). See Fig. 4.1.

We sample U1361a sediments at depth intervals corresponding precisely to *Cook et al.*'s (2013) ε_{Nd} and $^{87}Sr/^{86}Sr$ measurements. Importantly, Nd and Sr isotopes are taken from bulk sediment fractions, not authigenic minerals, and represent bedrock provenance rather than weathering trends. We measure ^{9}Be and ^{10}Be sorbed to marine authigenic minerals and ^{9}Be contained within biogenic opal (diatom frustules). We hypothesize that authigenic $^{10}Be/^{9}Be$ ratios will correlate well with *Cook et al.*'s 2013 record because ice sheet retraction should lead to increased ^{10}Be delivery offshore, elevating the $^{10}Be/^{9}Be$ ratio.

4.3. Methods

We obtained 23, ∼5 g samples from the archived IODP U1361a core through the IODP TAMU core repository. Samples were oven-dried overnight at 80°C and homogenized. ∼1 g aliquots of each sample were removed for freeze-drying, BET surface area analysis (MicroMeritics Tri-Star BET Analyzer, University of Pennsylvania) and laser particle size analysis (Malvern Mastersizer 2000, Montclair State University); diatom separation and dissolution; and Be isotope analysis.

4.3.1. Be leaching

We follow the sediment leaching procedure presented in *Ebert et al.* (2012). Bulk samples undergo 3 major steps: organics dissolution with heated 0.01M HNO_3 and 10M H_2O_2, a 24-hour agitation in 0.5M HCl (to extract amorphous oxide-bound Be), and 1M hydroxylamine-hydrochloride (to remove crystalline-bound Be). After each step, the supernate is separated from the sediment. All three supernate fractions are combined, centrifuged, and an aliquot is removed for $^{9}Be_{auth}$ measurement via ICP-MS[1] (University of New Hampshire). The remaining supernate is spiked with ∼200 μl of ^{9}Be carrier ($^{9}Be_{spike}$) (Scharlau Be carrier,

[1]Because samples were precipitated from the NaOH, HCl solution, we interpret diatom Be as minimum representative concentrations only. Dissolution via NaOH precludes ICP-MS analysis because of the over-abundance of Na+ ions which serve to clog the plasma torch. Alternative diatom dissolution methods with HF should be explored for use in this method (assuming clay removal is considered complete).

$^{10}Be/^{9}Be \approx 2 \times 10^{-15}$), passed through anion (BioRad 1x8 100-200 mesh) and cation (BioRad AG50-X8 200-400 mesh) exchange resins, precipitated at pH ~9 using NH_4OH:H_2O (1:1), dried overnight, and finally oxidized over open flame (>1000°C) [modified from *Kohl and Nishiizumi* (1992)]. $^{10}Be/^{9}Be_{spike}$ ratios are measured at the Purdue PRIME Lab AMS, from which ^{10}Be is calculated. We apply a decay correction to all ^{10}Be values using *Tauxe et al.*'s 2012 geomagnetic depth-age model and the decay equation: $^{10}Be(0)=^{10}Be \times exp(\lambda t)$, where $^{10}Be(0)$ is the dissolved ^{10}Be present in the overlying water column at the time of authigenic mineral precipitation, λ is the ^{10}Be decay constant (4.99×10^{-7} y^{-7}) and t is time (y). (For simplicity's sake, all decay-corrected concentrations will be expressed as ^{10}Be.)

To ensure that authigenic ^{9}Be is not sourcing from partially dissolved lithogenic ^{9}Be ($^{9}Be_{lith}$), we perform microwave digestion on the remaining sediment with concentrated HF (9 ml), HNO_3 (3 ml), and HCl (2 ml) (EPA method 3052: Microwave Assisted Acid Digestion of Siliceous and Organically Bound Matrices). $^{9}Be_{lith}$ trends are clearly unique from authigenic ^{9}Be and do not strongly correlate, indicating that our leaching procedure did not liberate lithogenic ^{9}Be and that authigenic ^{9}Be is accurately represented; see Fig. 4.2.

4.3.2. Diatom separation and dissolution

To analyze the concentrations of Be that entered the diatom frustule, we isolate diatoms from ~1 g bulk sediment samples selected from diatom-rich layers. We follow a multi-step procedure modified from *Egan et al.* (2012) to separate diatoms from clays surrounding and adhered to their frustule, including differential settling in Millipore ultrapure H_2O, heavy liquid separation with sodium poly(meta-)tungstate (*Shemesh et al.*, 1989; *Ellwood and Hunter*, 1999), and microfiltration (*Minoletti et al.*, 2008), which involves filtering the suspended samples through polycarbonate membrane filters submerged in a sonicator. We repeatedly filter the samples at sequentially smaller pore sizes (10, 5, and 2 μm). The diatoms were allowed to accumulate on the membrane, air-dried, and removed with Millipore ultrapure H_2O.

To ensure the diatoms are completely cleansed of clays, we analyzed select samples qualitatively, using scanning electron microscopy (SEM) (Quanta 600 FEG ESEM, University of Pennsylvania) in individual size fractions, and all samples semi-quantitatively, using X-Ray Diffraction (XRD) (Panalytical X-Pert Power X-ray Diffractometer, University of Pennsylvania). SEM images indicate minimal clay presence in size fractions >2μm. XRD analyses on bulk samples and clean diatom fractions indicate insignificant clay content and an abundance of amorphous content (biogenic opal). See Appendix A.

In each sample, all diatom size fractions >2μm were combined and dissolved in 0.2M NaOH (pH 13.3) for 40 minutes at 100°C, a method shown to minimize lithogenic dissolution (*Ragueneau et al.*, 2005; *Cardinal et al.*, 2007). The reaction is halted via addition of 1M HCl then raised to ∼pH 9 with NH_4OH, precipitating Be for ICP-MS analysis (University of New Hampshire). We were unable to obtain enough diatom mass for ^{10}Be measurement [Lal et al. (2006) estimated ∼100 mg of diatoms are required for AMS-detectable concentrations].

4.4. Results and Discussion

See Table 4.1 for a presentation of all isotope measurements alongside important geochemical proxies for temperature, biologic productivity and EAIS fluctuation in the Wilkes Land region.

4.4.1. Authigenic ^{10}Be

Authigenic ^{10}Be ranges 1.29±0.2 to 12.74±0.2 x 10^8 atoms g^{-1}, on the higher end of the range observed around Antarctica (*Frank et al.*, 1995; *Scherer et al.*, 1998; *Sjunneskog et al.*, 2007; *Yokoyama et al.*, 2016). ^{10}Be correlates strongly with geochemical proxies for Pliocene warmth and Wilkes Land EAIS retreat, including ε_{Nd} (r=0.80) and $^{87}Sr/^{86}Sr$ (r=-0.84); see Table 4.2.

^{10}Be concentrations in interglacial sediments are greater on average and statistically unique ($p<0.00001$) from glacial concentrations (interglacial sediments: 9.34±0.00 x 10^7 atoms g^{-1},

glacial sediments: 2.08±0.01 atoms x 10^7 g^{-1}). We attribute this pattern to increased ^{10}Be delivery offshore during interglacials via freshwater discharge and iceberg melt. Increases in the dissolved ^{10}Be load would be a direct result of melting ice contributions from the Wilkes Land, where deep water formation in the Adélie Depression would expedite the dissolved load down the continental slope in high salinity shelf waters (*Caburlotto et al.*, 2010), but also that advected from the westward flowing Antarctic Circumpolar Current. I.e., we cannot attribute increase in ^{10}Be to ice melt from the Wilkes Land region alone. Though, the close covariation of ^{10}Be with *Cook et al.*'s (2013) record hints at this direct source. Further, while we expect the ACC to transport large icebergs great distances (e.g., *Williams et al.*, 2010; *Cook et al.*, 2013), dissolved ^{10}Be contributions from melting icebergs do not contribute to bottom water ^{10}Be in stratified water masses (*Frank et al.*, 2002).

Several factors may cause the ^{10}Be record to vary consistently between lithological units/glacial-interglacial sediments. Some of these factors include production rate changes due to strengthening/weakening of the geomagnetic field, and physical parameters such as grain size and physical reworking, and mineralogy. We can rule out geomagnetic field fluctuations as the primary control on ^{10}Be using the overall variability in ^{10}Be measurements (r.s.d. 65%). Records of deep marine authigenic ^{10}Be typically range within a factor of ∼3 (*von Blanckenburg et al.*, 2015, and references therein), while records closer to continental margins vary by more than 2 orders of magnitude (*Simon et al.*, 2016, and references therein). The latter records highlight the dominance of the environmental signal over the geomagnetic closer to land. (The geomagnetic signal is likely present in our record, but it is unresolvable.)

Grain size also exerts a well-documented control on Be sorption, whereby Be concentrates on silt and clay size fractions with highly negative surface charges and an abundance of sorption sites (*You et al.*, 1989; *Aldahan et al.*, 1999; *Wittmann et al.*, 2012; *Boschi*, 2016). As expected, we observe a strong correlation between ^{10}Be and clay size abundance, and the greatest correlation is observed with the 11-15 μm range (r=0.72). Preferential loss of this fine fraction via a strong overflowing current (i.e. winnowing) might explain lowered

glacial-interval ^{10}Be. We can negate this possibility using grain size frequency distributions, which indicate extremely poor sorting. Much like grain size, sorption capacity of Be is also observed to correlate with increasing specific surface area (e.g., *Shen et al.*, 2004). However, our BET specific surface area measurements show no correlation with ^{10}Be. For grain size frequency diagrams and BET surface area analyses, see Appendix A.

Finally, clay mineralogy may exert a control on Be sorption. Regional clay mineralogy is dominated by illite with chlorite, smectite and kaolinite in descending abundance (*Damiani et al.*, 2006; *Verma et al.*, 2014); our analyses complement these findings (see Appendix A). In general, interglacial sediments are characterized by a relative increase in smectite abundance (*Cook et al.*, 2013). Experimentally, these dominant clay species are observed to equilibrate rapidly with Be at geologically instantaneous times (*You et al.*, 1989; *Taylor et al.*, 2012; *Boschi*, 2016). Thus, we regard it as unlikely that minor shifts in relative clay abundance can impart such a strong control on ^{10}Be fluctuations.

4.4.2. Authigenic ^{9}Be

Authigenic ^{9}Be ranges from 231±4 to 424±7 ng g^{-1}. Variations throughout the core are minor (overall r.s.d. 17%). Mean glacial and interglacial ^{9}Be concentrations are indistinguishable: 325±16 and 327±20 ng g^{-1}. These concentrations are lower than those measured in the Ross Sea in Holocene-age sediments (*Sjunneskog et al.*, 2007). Much like the Ross Sea record, we do not observe a significant correlation between ^{9}Be and changing lithofacies, suggesting the signal is complicated by indirect sediment transport from weathering zone to depositional location and/or that increased warming during interglacials does not significantly increase terrestrial weathering rates. Further, we may expect that in the Wilkes Land Subglacial Basin, which is largely below sea level, silicate weathering is kept to a minimum. Complex sediment transport accounts for the poor correlation between ^{9}Be and other geochemical proxies (see Table 4.2), and muted chemical weathering rates account for the low overall variation of ^{9}Be.

4.4.3. Authigenic $^{10}Be/^{9}Be$

The authigenic $^{10}Be/^{9}Be$ ratio ranges 0.59±0.09 to 6.94±0.09 x 10^{-8}, slightly lower than the globally averaged deep water $^{10}Be/^{9}Be$ dissolved in seawater (*von Blanckenburg and Bouchez*, 2014) and authigenic $^{10}Be/^{9}Be$ (*von Blanckenburg et al.*, 2015, and references therein), but in accordance with regional (*Sjunneskog et al.*, 2007) and high latitude records from authigenic minerals (*Aldahan et al.*, 1997; *Frank et al.*, 1997, 2008; *Simon et al.*, 2016) and ferromanganese crusts (*von Blanckenburg et al.*, 1996). Like the ^{10}Be record, the $^{10}Be/^{9}Be$ record correlates very well with glacial-interglacial oscillations. Accordingly, the ratio appears to be dominated by changes in ^{10}Be. We can see this by comparing the relative standard deviations of ^{10}Be (63%) and ^{9}Be (16%) with that of $^{10}Be/^{9}Be$ (60%). We would also expect a weakly positive trend between ^{10}Be and ^{9}Be in regions where ^{10}Be delivery varies greatly - due to changes in paleoproduction or, in this case, supply from melting ice sheets - and its signal is superimposed on that of boundary scavenging (see Section S6 of *von Blanckenburg et al.*, 2015). Indeed, we observe a weakly positive trend between ^{10}Be and ^{9}Be, confirming that the ratio mostly reflects ^{10}Be fluctuations; see Fig. 4.3.

The average $^{10}Be/^{9}Be$ ratio in interglacial sediments is 42.59±0.01 x 10^{-9}, a factor of 3.5 times greater than that in glacial sediments, 9.59±0.03 x 10^{-9}. High ^{10}Be and ^{9}Be loads and low $^{10}Be/^{9}Be$ ratios, indicate efficient transport of Be-bearing freshwaters (*Frank et al.*, 2009). Thus, the observation of globally low ratios supports our hypothesis that ^{10}Be is sourcing freshwaters discharged from the melting ice sheet. Comparably low ratio values are observed in other regions of deep water formation, such as the Fram Strait (*Frank et al.*, 2009).

4.4.4. Opal ^{9}Be

We find that at least 15% of the ^{9}Be sorbed to authigenic minerals is represented by that within diatoms; see Fig. 4.4. ^{9}Be measured in dissolved diatoms ranges from 1.89±0.04 to 51.1±1.21 ng g^{-1}, Table 4.3. This non-negligible percentage indicates significant portions of

the dissolved Be load enters the diatom frustule, a testament to the element's documented affinity for opal (*Chase et al.*, 2002; *Lal et al.*, 2006), particularly in zones where opal dominates the particle load (*Frank et al.*, 2000). The affinity for Be sorption to opal versus clay minerals is questioned (*Chase et al.*, 2002). Our data suggest a greater affinity of Be for clay minerals over opal in regions where both are present in abundance, but clay dominates.

Future applications should measure opal ^{10}Be as well. Measuring opal and authigenic ^{10}Be/^{9}Be from the same depth interval may allow for the reconstruction of Be depth profiles in seawater. While diatom frustule mineralization is limited to the shallow photic zone, authigenic mineral precipitation may better represent a depth-integrated average Be load of the overlying water column. Such an approach would require consideration of the timing of diatom frustule mineralization versus authigenic mineral precipitation.

4.5. ^{10}Be delivery during interglacials

Thus far, we have considered authigenic ^{10}Be/^{9}Be fluctuations in response to changing mineralogy, grain sizes, surface areas and opal content. Next, we discuss possible controls on ^{10}Be delivery to U1361a sediments, including changes in paleoproductivity and sea ice coverage.

4.5.1. The impact of paleoproductivity

We expect that during interglacials, increased biological productivity would effectively scavenge Be isotopes from the water column. As biological productivity proxies, we use opal weight percentages (opal $\%_{wt}$) and biogenic barium (*Cook et al.*, 2013), produced in the microenvironment surrounding settling diatoms (*Tjallingii et al.*, 2007). Here, biogenic barium is expressed as a ratio of scanning XRF-derived Ba/Al, to normalize for background lithogenic input of Ba (data obtained from *Tauxe et al.*, 2015). We observe significant positive correlations between ^{10}Be and opal $\%_{wt}$ (r=0.59) and ^{10}Be and Ba/Al (r=0.82) (see Table 4.2). The correlation between ^{9}Be and opal is insignificant, as is that between ^{9}Be and Ba/Al, perhaps indicating the majority of ^{9}Be was already particle associated upon

deposition. However, if the mechanism causing increased ^{10}Be in marine sediments was scavenging by biogenic particles alone, this does not explain the equally strong correlations between ^{10}Be and proxies for ice sheet terminus position, ε_{Nd} and ^{87}Sr/^{86}Sr, whose bulk chemistries are insensitive to particle flux.

Thus, all variables must reflect some underlying mechanism. We attribute this, as *Cook et al.* (2013) do, to increased warming during interglacials. Increased warming would lead to reduced sea ice coverage, allowing for greater bioproductivity in the shallow marine environment and increases in opal $\%_{wt}$ and Ba/Al. Warming would also increase ice mass discharge via calving and melting from the Wilkes Land region, leading to a retracted ice sheet terminus, fluctuations in Nd and Sr isotopes, and increases in ^{10}Be delivery offshore.

4.5.2. The impact of sea ice coverage

In the absence of sea ice, we would expect increased atmospheric flux to reach settling marine particulate. This phenomenon is especially likely during Pliocene interglacials when sea ice coverage was greatly reduced (*Whitehead et al.*, 2005). But, this source cannot alone account for interglacial ^{10}Be inventories delivered off the Antarctic coastline. Consider *Yokoyama et al.*'s (2016) record from the Ross Sea. Researchers attribute maximum [^{10}Be]≈3.8 x 10^{9} atoms g^{-1} to increased atmospheric deposition during ice-free periods. However, this value is inconsistent with atmospheric flux models, which yield a regional flux value of ∼5 x 10^{5} atoms cm^{-2} y^{-1} for the Ross Sea latitude (*Heikkilä*, 2007; *Field et al.*, 2006) [*Willenbring and von Blanckenburg*'s (2010a) Fig. 3], which may be an overestimate given that it is slightly higher than the dry deposition flux calculated from the Taylor Dome ice core (8.6 x 10^{4} atoms cm^{2} y^{-1}) (*Steig et al.*, 1995). Assuming 100% of atmospheric flux sorbs to settling marine sediments, this translates to ∼8.3 x 10^{7} ^{10}Be atoms g^{-1}, two orders of magnitude too low (when distributed over their 5 ky record of 20 cm thick sediments with a density of 1.5 g cm^{-3}). Clearly, additional sources are required to explain the missing nuclide inventory.

We repeat this exercise for our sediments using the closest source of meteoric ^{10}Be: the Mertz Glacier polynya. We assume the following: deep water flowing to site U1361 forms in the Mertz Glacier polynya with an area of 23,300 km^2; the volume of Adélie Land Bottom Water originating at this polynya is 1.78 x 10^8 km^3 (*Johnson*, 2008); and 100% of ^{10}Be which falls out on the polynya's surface adsorbs to settling particles over our longest interval of sedimentation (300 ky, density of 1.52 g cm^{-3}). We produce an inventory of only 1.29 x 10^2 atoms ^{10}Be g^{-1}. Clearly this value is a rough estimate, and ^{10}Be distribution on settling particles would vary spatially within bottom waters. Additionally, both the Mertz Glacier polynya size and Adélie Land Bottom Water volume would likely change during warmer Pliocene conditions. Nevertheless, even a doubling in both of these values would still result in ^{10}Be inventory far underestimating ($\ll$1%) our average measured value.

A more reasonable, much larger source of ^{10}Be must be the melting East Antarctic Ice Sheet during interglacials. See Fig. 4.5 for an illustration depicting Be transport along the Wilkes Land Region. ^{10}Be contribution from melting ice is invoked elsewhere to explain enriched concentrations of dissolved ^{10}Be in surface waters of the Drake Passage (*Kusakabe et al.*, 1982) and the Arctic (*Frank et al.*, 2009) and as a possible source of increased ^{10}Be observed in interglacial sediments (termed the "environmental signal") (*Simon et al.*, 2016, and references therein).

4.5.3. ^{10}Be in deep water formation zones

Finally, we note that concentrations of ^{10}Be measured in sediments offshore the Adélie Coastline are the highest measured near any zone of bottom water formation in the Antarctic including the Ross (*Sjunneskog et al.*, 2007; *Yokoyama et al.*, 2016) and Weddell Seas (*Frank et al.*, 1995), though no records exist to our knowledge of ^{10}Be in the two other regions of deep water formation, Prydz Bay and Cape Darnley. Antarctic bottom waters (AABW) flowing over the U1361 site are a combination of westward flowing waters that originate in the Ross Sea (*Rintoul*, 2007) and in coastal polynyas above the Adélie Depression (*Williams et al.*, 2008). AABW circulates around East Antarctica to Prydz Bay and

either continues circulating westward or diverts northwards into the Australian Antarctic Basin (*Rintoul*, 2007). Continuous circulation of AABW may lead to the enrichment of Be isotopes incorporated in zones of deep water formation. Based on our measurements, and because bottom waters originating at the Adélie Depression represent 38% of AABW (*Johnson*, 2008), it seems plausible that the Adélie coastline represents a major region of ^{10}Be input into AABW during interglacials.

On glacial-interglacial timescales, deep marine ^{10}Be/^{9}Be collected from authigenic and ferromanganese records remain relatively constant (*Willenbring and von Blanckenburg*, 2010b; *von Blanckenburg et al.*, 2015) and it is posited that the ^{10}Be/^{9}Be ratio may be set at the ocean's margins, where, globally, the vast majority of ^{9}Be is added and ^{10}Be is removed (*von Blanckenburg et al.*, 1996; *von Blanckenburg and Bouchez*, 2014). Our results show that where Adélie Land Bottom Water forms the opposite trend is observed: melting glacial ice injects ^{10}Be into deep waters and ^{9}Be is relatively depleted, raising the ^{10}Be/^{9}Be ratio. If the ^{10}Be/^{9}Be ratio advects conservatively in water masses (*von Blanckenburg et al.*, 1996), then deep, saline water masses may prove vital in "insulating" ^{10}Be/^{9}Be values from the effects of shallow water scavenging and extend Be isotope residence time out of the ACC and into the global thermohaline circulation belt.

4.6. Summary

We analyze the authigenic ^{10}Be/^{9}Be record in marine sediments spanning several Pliocene glacial-interglacial intervals. By comparing this record to existing geochemical proxies for EAIS fluctuations, we posit that the first order control on the ^{10}Be/^{9}Be ratio must be freshwater discharged from the EAIS during interglacial period melting. The most important indicator supporting this interpretation is the strong positive correlation between ^{10}Be/^{9}Be and ε_{Nd} and ^{87}Sr/^{86}Sr, which are unaffected by other controls on ^{10}Be delivery to marine sediments, including paleoproductivity and sea ice coverage.

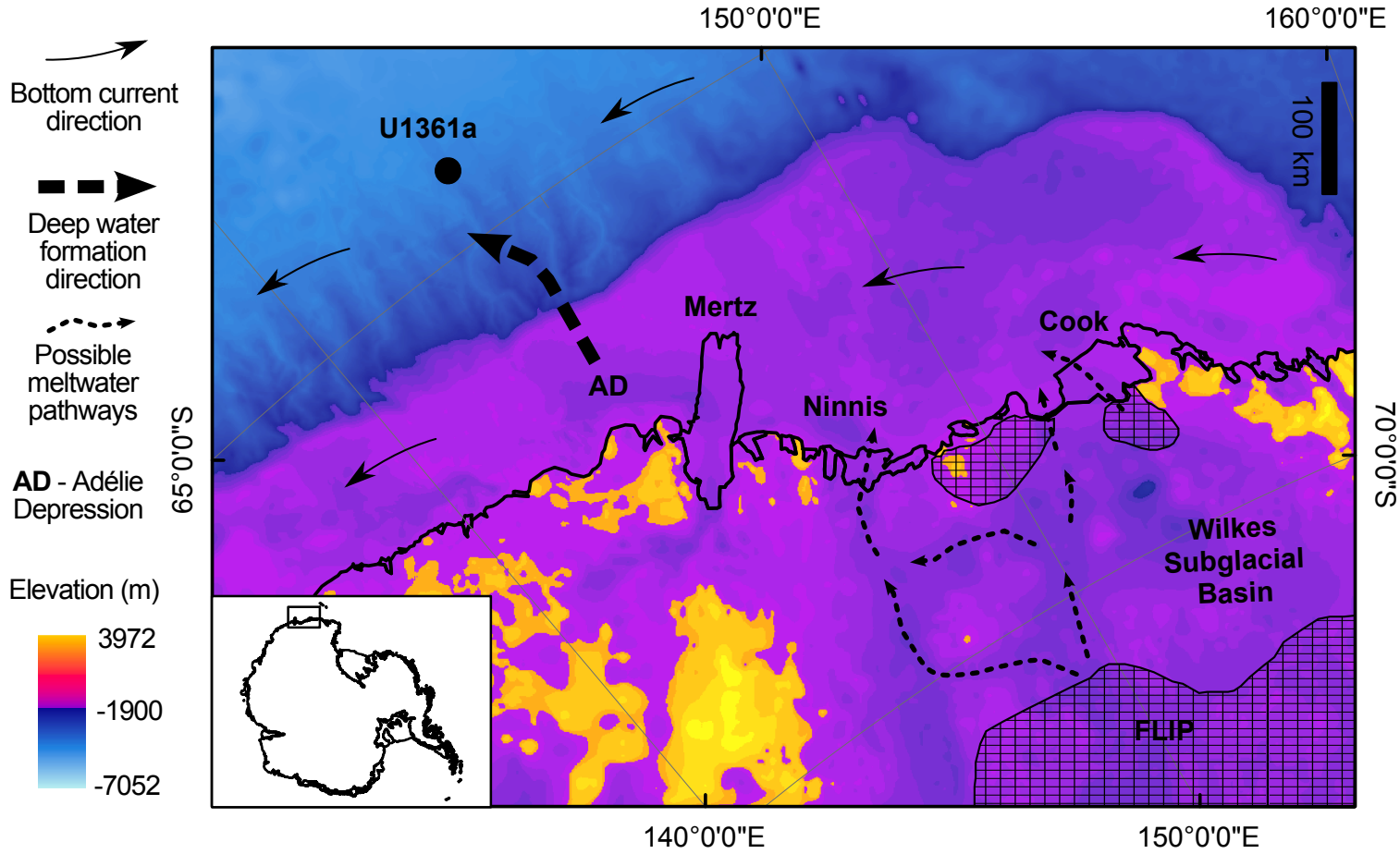

Figure 4.1: Site map U1361a offshore the Adélie Coastline, East Antarctica. Note major tidewater glaciers: Cook, Ninnis and Mertz. The Wilkes Subglacial Basin is almost entirely below sea level. Hypothesized FLIP subglacial outcrops are indicated with hatch marking (*Ferraccioli et al.*, 2009). Local bottom water forms in the Adélie Depression, flowing northwestward to mix with westward flowing bottom waters originating in the Ross Sea. Bottom current directions and possible meltwater pathways from *Cook et al.* (2013). Topographic data: BedMap2 (*Fretwell et al.*, 2013).

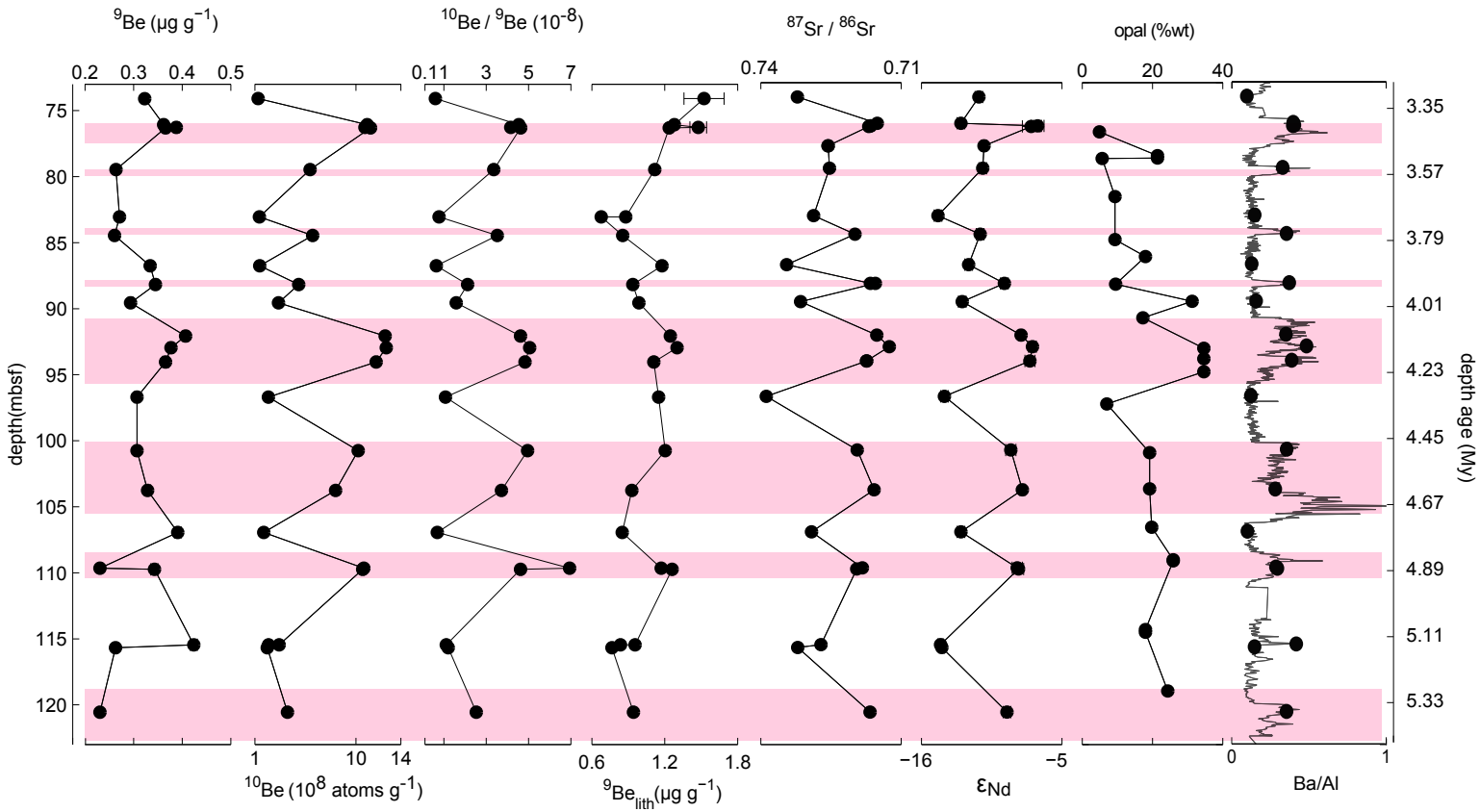

Figure 4.2: Down-core Be authigenic and lithogenic fractions compared to *Cook et al.*'s (2013) ε_{Nd}, $^{87}Sr/^{86}Sr$, and opal weight percentage (opal $\%_{wt}$) data and *Tauxe et al.*'s (2015) Ba/Al data. Ba/Al: thin black line shows entire record, black dots indicate measurements at our corresponding sampling depths. Maximum ^{10}Be and $^{10}Be/^{9}Be$ values peak in interglacial (pink) units, where ε_{Nd}, $^{87}Sr/^{86}Sr$, opal $\%_{wt}$, and Ba/Al data indicate a retracted EAIS in the Wilkes Land region and warmer, more productive conditions. Authigenic ^{9}Be is, on average, lower in interglacial sediments than in glacial sediments, but not consistently so. Lithogenic ^{9}Be shows no correlation with authigenic ^{9}Be or ^{10}Be. See Section 4.4.

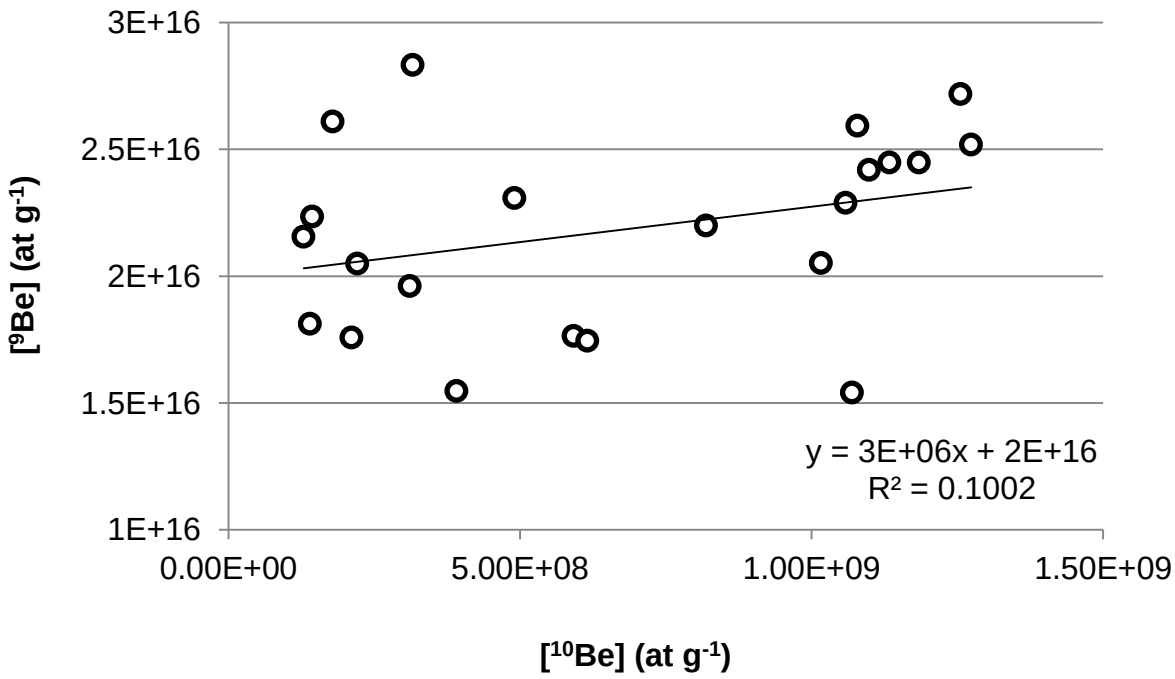

Figure 4.3: [^{10}Be] vs [^{9}Be], normalized to average down-core values of each. Global datasets expressing a weak, positive linear relationship (m<1) indicate the ^{10}Be/^{9}Be signal is dominated by changes in ^{10}Be supply.

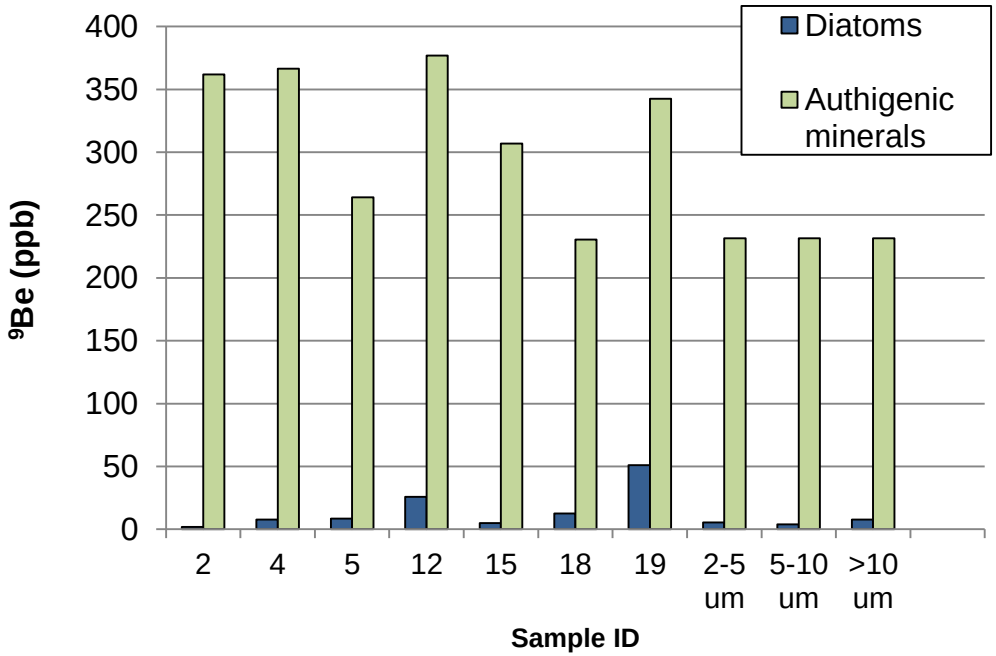

Figure 4.4: ^{9}Be in biogenic opal (diatoms) compared to that leached from authigenic minerals.

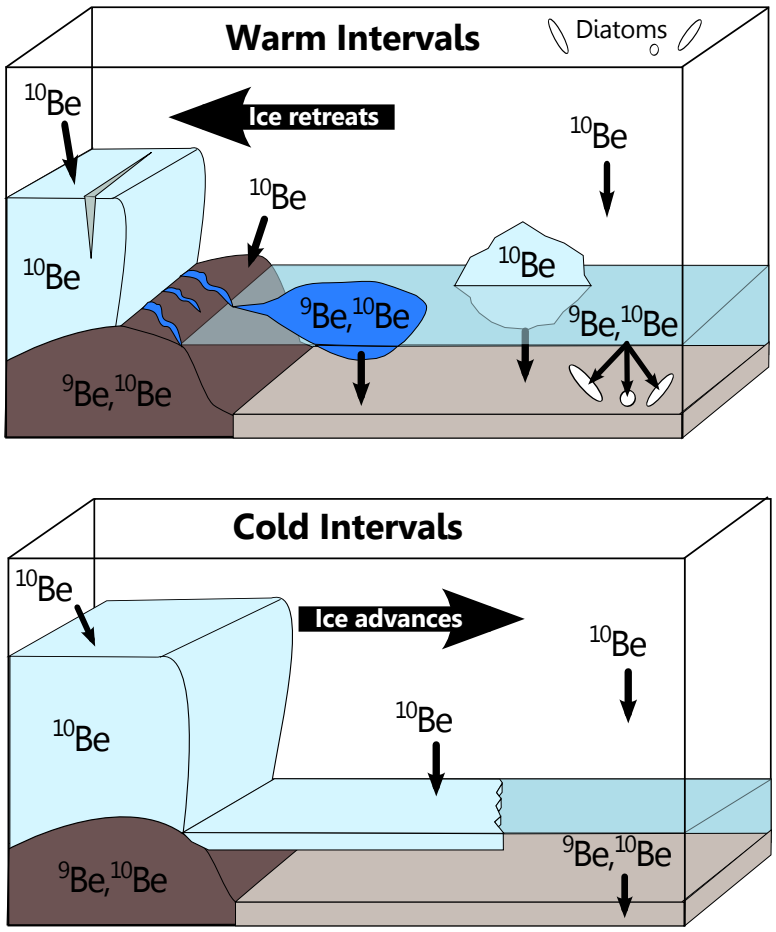

Figure 4.5: Illustration depicting ^{10}Be fallout and delivery to submarine sediments. During warm interglacials, the ice sheet retracts inland, its calved icebergs and discharging freshwaters release ^{10}Be and freshly exposed high elevation region undergo increased weathering, liberating ^{9}Be. During cold glacials, the ice advances again and sea ice becomes a permanent feature. Ice coverage disallows fallout ^{10}Be from reaching sub-ice shelf sediments. (Dimensions not to scale.)

Depth (m)	Sample ID	Depth age (My)	^{10}Be (10^8 atoms g^{-1})	^{9}Be (ng g^{-1})	^{10}Be/^{9}Be error (10^{-9})	^{9}Be$_{lith}$ (μg g^{-1})	Unit*
74.09	01	3.31	1.29 ± 0.20	323 ± 5	5.97 ± 0.94	1.49 ± 0.16	1
76.07	02	3.84	10.98 ± 0.21	362 ± 5	45.41 ± 0.89	1.26 ± 0.02	2
76.27	03	3.85	10.79 ± 0.14	388 ± 6	41.60 ± 0.54	1.50 ± 0.07	2
76.31	04	3.86	11.33 ± 0.18	366 ± 6	46.30 ± 0.73	1.24 ± 0.02	2
79.47	05	4.09	5.92 ± 0.08	264 ± 4	33.55 ± 0.45	1.09 ± 0.00	2
83.05	06	4.18	1.40 ± 0.02	271 ± 5	7.71 ± 0.12	0.86 ± 0.01	3
84.45	07	4.22	6.15 ± 0.08	261 ± 5	35.25 ± 0.49	0.90 ± 0.00	2
86.75	08	4.28	1.43 ± 0.02	334 ± 5	6.42 ± 0.11	1.25 ± 0.01	3
88.17	09	4.31	4.90 ± 0.08	345 ± 5	21.24 ± 0.33	0.94 ± 0.01	2
89.55	10	4.35	3.11 ± 0.05	294 ± 5	15.84 ± 0.28	0.99 ± 0.00	3
92.07	11	4.42	12.56 ± 0.18	407 ± 6	46.20 ± 0.67	1.24 ± 0.01	2
92.95	12	4.44	12.74 ± 0.17	377 ± 5	50.58 ± 0.69	1.23 ± 0.01	2
94.03	13	4.47	11.84 ± 0.15	366 ± 6	48.38 ± 0.61	1.10 ± 0.01	2
96.7	14	4.54	2.21 ± 0.03	307 ± 5	10.77 ± 0.16	1.01 ± 0.01	3
100.75	15	4.22	10.16 ± 0.15	307 ± 5	49.55 ± 0.75	1.16 ± 0.00	2
103.76	16	4.36	8.19 ± 0.10	329 ± 6	37.23 ± 0.47	0.90 ± 0.01	2
106.94	17	4.51	1.79 ± 0.03	391 ± 7	6.85 ± 0.12	0.84 ± 0.00	3
109.65	18	4.63	10.69 ± 0.13	231 ± 4	69.43 ± 0.88	1.14 ± 0.01	2
109.74	19	4.63	10.58 ± 0.14	343 ± 7	46.24 ± 0.62	1.26 ± 0.01	2
115.45	20	4.83	3.16 ± 0.06	424 ± 7	11.14 ± 0.20	0.85 ± 0.00	3
115.45	20dup†	4.83	2.22 ± 0.03	-	-	0.82 ± 0.01	3
115.67	21	4.84	2.11 ± 0.04	263 ± 5	12.01 ± 0.25	0.77 ± 0.01	3
120.55	22	4.56	3.91 ± 0.08	231 ± 4	25.27 ± 0.53	0.82 ± 0.01	2

*Lithological units (as defined by *Cook et al.* (2013)). 1: silty clay with dispersed clasts, 2: diatom-rich silty clay, 3: clay with dispersed clays

†Duplicate sampling indicates leaching procedure is reproducible to within ∼30%.

Table 4.1: Be isotopes in authigenic and lithogenic fractions of U1361a sediments.

	11-15 μm grain size	Auth ^{9}Be (ppm)	Auth ^{10}Be (at g^{-1})	Lith Be (ppm)	^{10}Be/ ^{9}Be	ε_{Nd}	^{87}Sr/^{86}Sr	BET (m^2 g^{-1})	Ba/Al	Opal ($\%_{wt}$)
11-15 μm grain size	1.000									
Auth ^{9}Be (ppm)	0.289	1.000								
Auth ^{10}Be (at g^{-1})	**0.720**	0.316	1.000							
Lith Be (ppm)	0.336	0.324	**0.499**	1.000						
^{10}Be/ ^{9}Be	**0.668**	0.028	**0.941**	0.410	1.000					
ε_{Nd}	**0.433**	0.197	**0.802**	**0.502**	**0.771**	1.000				
^{87}Sr/^{86}Sr	**-0.570**	-0.213	**-0.837**	-0.226	**-0.804**	**-0.791**	1.000			
BET (m^2 g^{-1})	**-0.454**	0.172	-0.154	**0.434**	-0.205	-0.089	0.423	1.000		
Ba/Al	**0.760**	0.326	**0.813**	0.265	**0.760**	**0.674**	**-0.885**	**-0.497**	1.000	
Opal ($\%_{wt}$)	0.272	0.275	**0.589**	0.007	**0.536**	**0.530**	**-0.679**	-0.233	**0.589**	1.000

Table 4.2: Pearson correlation coefficients of geochemical proxies in U1361a sediments (**significant at 95% C.I.**).

Sample	Sample depth (mbsf)	Opal mass (mg)	Opal ^{9}Be (ng g^{-1})	% Authigenic ^{9}Be in diatoms
2	76.07	13.51	1.89 ± 0.04	0.52
4	76.31	29.88	7.68 ± 0.14	2.1
5	79.47	17.71	8.39 ± 0.06	3.18
12	92.95	26.51	25.89 ± 0.57	6.87
15	100.75	33.64	4.86 ± 0.27	1.58
18	109.65	14.65	12.52 ± 0.24	5.43
19	109.74	28.43	51.05 ± 1.21	14.9
22, 2-5 μm	120.55	16.05	5.57 ± 0.2	2.41
22, 5-10 μm	120.55	17.51	3.81 ± 0.14	1.65
22, >10 μm	120.55	84.81	7.72 ± 0.17	3.34

Table 4.3: ^{9}Be in biogenic opal.

CHAPTER 5 : Extreme decay of meteoric beryllium-10 as a proxy for persistent aridity

Previously published as:

Valletta, R.D., Willenbring, J.K., Lewis, A.R., Ashworth, A.C., and Caffee, M., 2015, Extreme decay of meteoric beryllium-10 as a proxy for persistent aridity: Scientific Reports, v. 5, p. 17813, doi: 10.1038/srep17813.

Abstract

The modern Antarctic Dry Valleys are locked in a hyper-arid, polar climate that enables the East Antarctic Ice Sheet (EAIS) to remain stable, frozen to underlying bedrock. The duration of these dry, cold conditions is a critical prerequisite when modeling the long-term mass balance of the EAIS during past warm climates and is best examined using terrestrial paleoclimatic proxies. Unfortunately, deposits containing such proxies are extremely rare and often difficult to date. Here, we apply a unique dating approach to tundra deposits using concentrations of meteoric beryllium-10 (^{10}Be) adhered to paleolake sediments from the Friis Hills, central Dry Valleys. We show that lake sediments were emplaced between 14-17.5 My and have remained untouched by meteoric waters since that time. Our results support the notion that the onset of Dry Valleys aridification occurred ∼14 My, precluding the possibility of EAIS collapse during Pliocene warming events. Lake fossils indicate that >14 My ago the Dry Valleys hosted a moist tundra that flourished in elevated atmospheric CO_2 (>400 ppm). Thus, Dry Valleys tundra deposits record regional climatic transitions that affect EAIS mass balance, and, in a global paleoclimatic context, these deposits demonstrate how warming induced by 400 ppm CO_2 manifests at high latitudes.

5.1. Introduction

The long-standing dispute concerning the stability of the East Antarctic Ice Sheet (EAIS) calls into question its susceptibility to collapse throughout Neogene climate changes (*Bar-*

rett, 2013). Two opposing views pervade the literature: the "dynamic" hypothesis posits that the EAIS underwent major retraction during mild Pliocene warming events, reducing to as much as two-thirds of its present size (*Wilson*, 1995; *Hambrey and McKelvey*, 2000; *Rebesco et al.*, 2006), while the opposing "stable" hypothesis argues the EAIS has been largely frozen to its bed since ∼14 My and has undergone only minimal, peripheral melting during Pliocene warming (*Marchant et al.*, 1993, 1996; *Sugden*, 1996; *Lewis et al.*, 2008). The dynamic theory - if correct - would imply drastic Antarctic ice mass loss and resultant sea-level rise (tens of meters) under atmospheric temperatures and CO_2 concentrations that were only modestly greater than today (2-3°C and 350-450 ppmv, respectively (*Royer*, 2014; *Dowsett*, 2007) and that are projected within the coming century (*Stocker*, 2014). With such great implications, there remains a need to expand the number of geological datasets that inform on the EAIS's behavior through time.

Central to the dynamic/stable controversy is the timing of the onset of polar aridity, which limits substantial ice mass loss to only sublimation and is a key factor in determining long term EAIS mass balance (*Lewis et al.*, 2008). The hyper-arid polar conditions of the Dry Valleys have protected inland sites from alteration due to weathering via precipitation or ice melt since the mid-Miocene. As such, these relict landscapes have the potential to record the inception of polar aridity and critically comment on the dynamic/stable debate, but targeted sampling locations that contain paleoclimatic proxies are uncommon and difficult to directly date.

We present a rare, continuous record of climate change contained within the innermost, highest elevation zone of the Dry Valleys. The Friis Hills, Taylor Valley (800 masl) contains a thick (14 m) series of stacked glacial drifts found interbedded with silty paleolacustrine sediments. These sediments contain a diverse fossil assemblage now extinct in Antarctica including *Nothofagus* (southern beech) wood and leaves. Although brine lakes commonly exist alongside and under Antarctic glaciers under the modern climatic regime (*Frezzotti et al.*, 2004), the fossils within Paleolake Friis sediments were likely deposited in a semi-

permanent proglacial lake on wet, freshwater tundra. Because modern climatic conditions at the Friis Hills are extremely cold (average annual temperature: -22°C) and arid (lows measured <16% relative humidity) (*Mikucki et al.*, 2015), these deposits must archive a period of warmer and wetter climatic conditions. Directly dating these sediments becomes necessary to resolve when tundra-like conditions last prevailed in the upper, inner Dry Valleys.

Meteoric beryllium-10 as an age indicator

To provide chronologic control for the lake sediments we utilize beryllium-10 (^{10}Be) as an isotopic tracer. Cosmic-ray-produced (cosmogenic) ^{10}Be forms in the atmosphere when high-energy neutrons from secondary cosmic rays spall nitrogen and oxygen atoms. This ^{10}Be, denoted meteoric ^{10}Be, exists in the form of ^{10}BeO and ^{10}Be(OH)$_2$ in the atmosphere and quickly adheres to atmospheric aerosols (primarily sulfates) (*Lal and Peters*, 1967). The ^{10}Be-bearing aerosols are then delivered to the Earth's surface through wet (rain) or dry (dust) deposition. Through continued deposition, meteoric ^{10}Be will accumulate at the surface and at depth, as ^{10}Be moves into the soil column via infiltration and clay illuviation (*Willenbring and von Blanckenburg*, 2010a).

5.2. Sediment age model

Concentrations of meteoric ^{10}Be adhered to Paleolake Friis sediments are used to model a minimum age of paleolacustrine deposition. *Lebatard et al.* (2010) first demonstrated that it is possible to date ancient terrestrial deposits with meteoric ^{10}Be if, once buried, sediments remain a closed system. One way to achieve this prerequisite is if meteoric waters do not infiltrate the subsurface. When these conditions are met, the measured ^{10}Be reflects the initial inventory, $[^{10}\text{Be}]_{initial}$, which is only altered by decay. A hyper-arid climate in the Dry Valleys provides the conditions needed for a closed ^{10}Be system, allowing the use of meteoric ^{10}Be as a chronometer.

To model sediment age, we first determine a range of potential $[^{10}\text{Be}]_{initial}$. This is possible

if we model lake sediments as soil surface sediments. Solving *Willenbring and von Blanckenburg*'s (2010a) equation for steady state erosion rate (Eq. 21) we estimate a likely range of $[^{10}\mathrm{Be}]_{initial}$ (Eq. 2.8, reprinted here):

$$[^{10}Be]_{initial} = \frac{Q}{\rho\varepsilon} \tag{5.1}$$

where Q is flux of ^{10}Be to the Earth's surface (at cm^{-2} y^{-1}), ε is erosion rate (cm y^{-1}), ρ is soil density (1.57 g cm^{-3}), and $[^{10}\mathrm{Be}]_{initial}$ is the measured surface concentration (1.53 x 10^7 at g^{-1}). We use the ^{10}Be flux calculated for Table Mountain (3.4 x 10^3 at cm^{-2} y^{-1}) (*Dickinson et al.*, 2012), a nearby location that is a suitable representative analog of Friis Hills because comparable arid, windy conditions disallow accumulation of atmospheric aerosols on the earth's surface. To estimate ε, we use a range of plausible erosion and total denudation rates obtained independently throughout the Dry Valleys on bedrock and regolith material (Table 5.2).

To determine when lake sediments were emplaced, we utilize the radioactive decay equation (Eq. 2.2, reprinted here):

$$N(t) = N_0 exp(-\lambda t) \tag{5.2}$$

where $N(t)$ is the measured $[^{10}\mathrm{Be}]$ in the "blank" sample (3.48 x 10^4 $\pm$ 3.48 x 10^4 at g^{-1}), N_0 is $[^{10}\mathrm{Be}]_{initial}$ (at g^{-1}) determined using Eq. 5.1, and λ is the ^{10}Be decay constant ($\lambda = \frac{ln(2)}{t_{1/2}}$ = 5 x 10^{-7} y^{-1}), and t is age (y). Thus, solving Eq. 5.2 for t will yield the time range during which Paleolake Friis sediments were emplaced.

Central to our approach are measurement capabilities. The ^{10}Be concentrations are measured using accelerator mass spectrometer (AMS); the detection sensitivity is $\sim 10^4$ at g^{-1}. Given the half-life of ^{10}Be ($t_{1/2}$=1.387 My) (*Chmeleff et al.*, 2010), the detection limit corresponds to a maximum age of ~14 My. That is, assuming no $[^{10}\mathrm{Be}]$ lost in lake sediment

erosion, an AMS measurement of [^{10}Be] within error of $\sim 10^4$ at g^{-1} indicates a maximum lake sediment age of 14 My.

5.3. Methods

5.3.1. Treating paleolake sediments

During the austral summer of 2008, five samples for meteoric ^{10}Be dating were collected from silty paleolacustrine sediments exposed on a hillside within the Friis Hills stacked tills. Samples were prepared at the University of Pennsylvania Cosmogenic Isotope Lab following protocol for adhered meteoric ^{10}Be extraction, including a 0.5 M HCl agitated leach and a 1 M hydroxylamine hydrochloride ($NH_2OH \bullet HCl$) leach in an ultrasonic bath (*Ebert et al.*, 2012). Following ^{9}Be spike addition (GFZ German Research Centre for Geosciences "Phenakite" standard, $^{10}Be/^9Be_{spike} = 10^{-16}$) and ion exchange chromatography, samples were oxidized over open flame, packed with Nb powder into cathode targets, and sent to the Purdue PRIME Lab for AMS measurement of ^{10}Be/^{9}Be.

5.3.2. Error assessment

The overall range of erosion rates reported in the literature is 0.1-2.6 m My^{-1} corresponding to an overall range of $[^{10}Be]_{initial}$ of 0.83 to 22.00 x 10^7 at g^{-1} (see Table 5.2). Not all published erosion rates are reported with associated errors and cannot be recalculated because in most cases erosion rate error distributions, ^{9}Be carrier spike, and/or assumed ^{10}Be/^{9}Be spike ratio were not reported. These missing data prohibit the inclusion of simple error propagation in our age model. Nevertheless, to assess the impact of error on our age estimates we apply a commonly reported error value of 10% to the upper and lower erosion rate estimates. This implementation results in marginally different lake sediment age estimates (10.7-17.7 My). Thus, incorporating erosion rate error does not affect our overall thesis.

5.3.3. Choosing a flux value, Q

The proper choice of a flux value, Q, is critical for constraining the emplacement age of Friis Hills sediments. We have chosen a relatively low flux value of 3.4 x 10^3 at cm^{-2} y^{-1} because it has been quantified from a nearby location with extremely similar climatic and erosional conditions (*Dickinson et al.*, 2012). Other applications of meteoric ^{10}Be dating in the Dry Valleys have instead used a higher flux value that was determined from the Taylor Dome ice core (1.3 x 10^5 at g^{-1} y^{-1}) (*Steig et al.*, 2000). Using this greater flux value for Paleolake Friis sediments yields a much older emplacement age of 18.2-24.8 My. This range exceeds the underlying ash's age of 19.76 My (*Lewis and Ashworth*, 2015). As such, we regard the Taylor Dome flux value as unreasonably high for the Friis Hills location.

5.4. Results

Three samples collected at or below 26 cm depth at the Friis Hills fall below or within the 1-σ uncertainty of "blank" samples (see Table 5.1, Fig. 5.1), thus indicating that measured concentrations approach the analytical limit of AMS (^{10}Be/^{9}Be$\approx$9 x 10^{-16}) and chemical extraction process (ranging from ^{10}Be/^{9}Be$\approx$1 x 10^{-15} to 5 x 10^{-15}). We note that other publications measure concentrations at the surface and at depth up to two and six orders of magnitude greater, respectively (*Graham et al.*, 2002; *Dickinson et al.*, 2012; *Schiller et al.*, 2009, 2014). Higher concentrations may simply be a reflection of younger surfaces. The most comparable measurements made elsewhere are from Table Mountain (see Fig. 5.1, profile TM4). These data have been corrected for contamination from *in situ* ^{10}Be. While meteoric ^{10}Be is adsorbed to the outside of clay minerals, *in situ* ^{10}Be is produced and contained within the mineral structure itself. As *Dickinson et al.* (2012) note, *in situ* concentrations are commonly $< 1\%$ of the meteoric ^{10}Be concentrations, but because of the great age of Dry Valleys sediments these two fractions may be of the same magnitude. *In situ* ^{10}Be concentrations are most likely liberated via partial decomposition of the clay mineral due to an aggressive leaching solution. By correcting for this contamination, the authors constrain the ^{10}Be flux value (Q) that we use to help model a $[^{10}\mathrm{Be}]_{initial}$ range.

The modeled $[^{10}Be]_{initial}$ range is 0.83 to 22 x 10^7 at g^{-1} (see Section 5.3, Table 5.2). We compile a database of $[^{10}Be]$ measurements from modern and ancient lake sediments and find that our estimates for $[^{10}Be]_{initial}$ are well within the range of published values (see Table 5.3). The corresponding age range for the minimum time since lake sediment deposition is 11.0-17.5 My (see Fig. 5.2). The upper limit of 17.5 My is in agreement with a 19.76 ± 0.11 My ($^{40}Ar/^{39}Ar$ dated) ash that lies stratigraphically below sampling Pit 1 to the east (*Lewis and Ashworth*, 2015). Assuming no erosion of paleolake sediments, the lower limit of 11.0 My indicates $[^{10}Be]>10^4$ at g^{-1} (near the AMS detection capability). However, measured concentrations within error of our "blank" indicate that Friis Hills lacustrine deposits must be at least ∼14 My. Accordingly, we raise the lower age limit estimate and propose an adjusted range for lake sediment ages: 14.0-17.5 My.

5.5. Discussion

5.5.1. Middle Miocene climatic transitions and Paleolake Friis emplacement

Lake sediments' age range spans the Middle Miocene Climatic Optimum (MMCO) ∼15-17 My. This period is characterized by increases in global marine and terrestrial temperatures and reduced global ice coverage as indicated by marine stable isotope records (*Zachos et al.*, 2008). In the Ross Sea region, abundant evidence for increased temperatures during the MMCO is well documented in the ANDRILL 2A core, including lithostratigraphic (*Passchier et al.*, 2011), palynological (*Warny et al.*, 2009) and leaf wax abundance (*Feakins et al.*, 2012) studies. These studies recognize periods of a retracted EAIS margin, decreased sea ice coverage, increased precipitation along the Ross Sea coastline, and a proliferation of vegetation. Definitive terrestrial evidence of the MMCO is found in high altitude tills deposited by wet-based ice (*Lewis et al.*, 2007) and in preserved lake fossils (*Lewis et al.*, 2008), but is otherwise sparse.

The Middle Miocene Climate Transition (MMCT) followed the MMCO at ∼14 My. It is marked most notably by ice sheet expansion accompanied by a rapid, 8°C cooling on

land (13.85-14.07 My)(*Lewis et al.*, 2008) and 6-7° C cooling in the southern Pacific ocean (13.8-14.2 My)(*Shevenell et al.*, 2004). Marine depositional and terrestrial erosional features record this expansion in thick offshore Middle Miocene units in the Ross Sea (*Fielding et al.*, 2011), in the cross-cutting bedrock channels of the Labyrinth, Wright Valley (*Lewis et al.*, 2006), and in the Friis Hills themselves, where glacial expansion and down-cutting likely formed the near-modern surface (*Lewis and Ashworth*, 2015). A synchronized transition to arid conditions is recorded in volcanic ashes in nearby Olympus (*Lewis et al.*, 2007) and western Asgard Ranges (*Marchant et al.*, 1993, 1996). Workers note that ashfalls infill sand-wedge troughs, which form only in cold/dry conditions, contain glass shards, and lack evidence of cryoturbation or clay formation. This pristine preservation indicates no presence of surface moisture or chemical weathering since the time of ash emplacement. The oldest, unaltered ash deposits in the Dry Valleys indicate that other parts of the region have experienced uninterrupted polar desert climate since ∼15 My (*Marchant et al.*, 1996); our results expand this zone.

Based on the abundant evidence for warmer global and regional temperatures ∼15-17 My, we suggest that Paleolake Friis sediments were likely emplaced during the MMCO (see Fig. 5.3). At their warmest, terrestrial summer temperatures reached as high as 10°C (*Warny et al.*, 2009), great enough to support a wet tundra environment in which fossils like *Nothofagus* thrived [*Lewis et al.* (2008) associated this species with mean summer temperatures of ∼5°C]. Warmer temperatures coincide with increases in global CO_2 reconstructions. According to *Royer*'s 2014 data compilation, the MMCO is arguably the last time global CO_2 remained 400 ppm for several million years, making CO_2 a possible driver of EAIS retraction and terrestrial plant proliferation at this time. The linkages between global CO_2 concentrations, ice volume and vegetation during the MMCO have proven challenging to model, but these simulations are valuable towards our understanding of future climate and require improvement. A notable model deficiency is the lack of reliable temperature proxy data, particularly at high latitudes (e.g., *Goldner et al.*, 2014). The Paleolake Friis deposits, along with those described in *Lewis et al.* (2008), represent the southernmost terrestrial de-

posits, and highest latitude deposits overall, available for middle Miocene paleoclimatic reconstructions. These records should be incorporated as constraints when modeling the MMCO; they are especially useful in reconstructing Equator to pole temperature gradients.

Following their deposition, Paleolake Friis sediments entered a closed system, one that did not receive meteoric ^{10}Be in surface waters via ice melt or precipitation. This closed system is maintained if plunging temperatures of the MMCT $\sim$14 My were accompanied by an onset of extreme aridity. The lack of ^{10}Be in lake sediments indicates persistent polar aridity was established in the inner Dry Valleys by at least this time, contradicting the notion of large-scale EAIS collapse during the Pliocene.

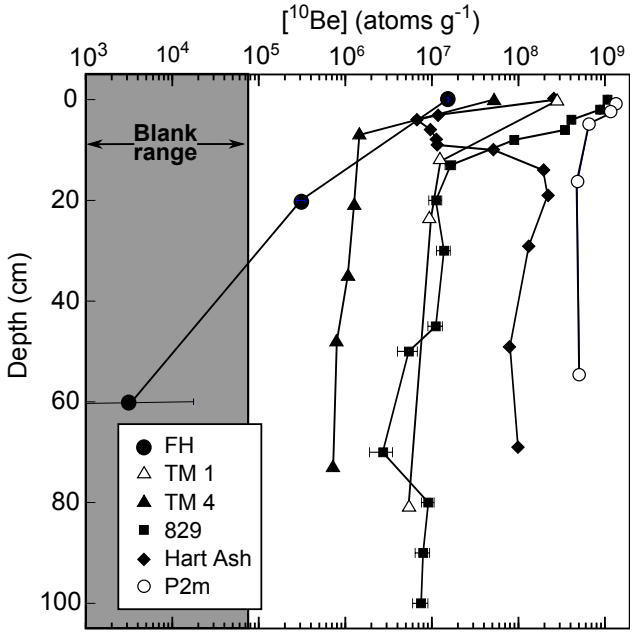

Figure 5.1: Meteoric [^{10}Be] measured in shallow Dry Valleys sediments. FH (Friis Hills, this study's Pit 1); TM 1, TM 4 (corrected for *in situ*^{10}Be contamination) (*Dickinson et al.*, 2012); 82920; Hart Ash (and its underlying paleosol) (*Schiller et al.*, 2009); P2m (*Schiller et al.*, 2014). Gray shading indicates measured [^{10}Be] and associated error in the chemical blank. Results from Pit 2 register [^{10}Be] < 0 at g^{-1} and, as such, cannot be plotted on log scale.

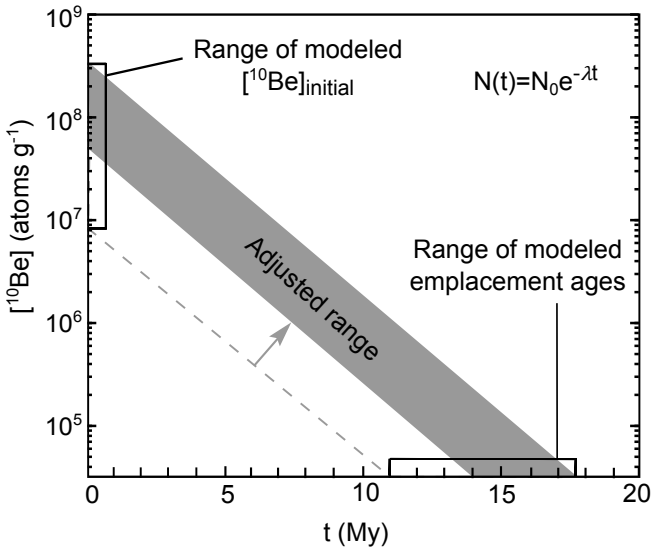

Figure 5.2: Using the radioactive decay equation, the decay of $[^{10}\mathrm{Be}]_{initial}$ to the modern "blank" concentration (3.48 x 10 $^4\pm$ 3.48 x 10^4 at g^{-1}) corresponds to a sediment emplacement age of 11.0-17.5 My. The AMS detection sensitivity of $\sim 10^4$ at g^{-1} corresponds to $\sim$14 My resulting in an adjusted age range of 14.0-17.5 My.

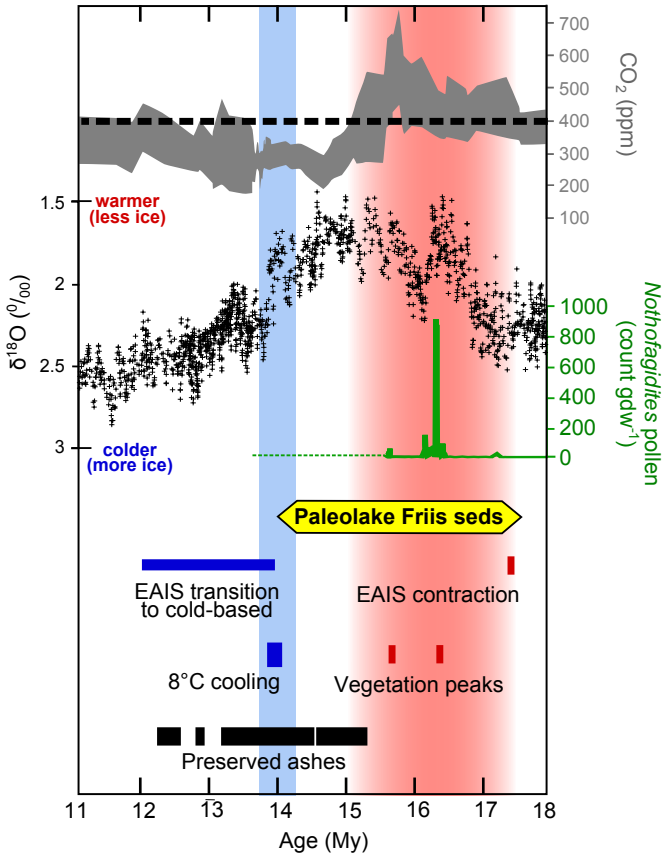

Figure 5.3: Modeled age range of Paleolake Friis sediments (14.0-17.5 My) and global and regional paleoclimatic indicators throughout the middle Miocene. In red: the MMCO defined globally ∼15-17 My (*Zachos et al.*, 2008) and regionally 15.4-17.6 My (*Passchier et al.*, 2011). In blue: the MMCT, 13.8-14.2 My (*Shevenell et al.*, 2004). Labeled events include: the onset of EAIS contraction, 17.21-17.49 My (*Sandroni and Talarico*, 2011); peaks in vegetation expansion (including terrestrial tundra taxa and marine and freshwater algae species) centered on 15.7 and 16.4 My (*Feakins et al.*, 2012); the range of ages of pristinely preserved ashes (measurement error included in bar width) (*Marchant et al.*, 1996; *Sugden*, 1996; *Lewis et al.*, 2007); 8°C cooling on Antarctica (*Lewis et al.*, 2008); EAIS transition to cold-based 12-14 My prior to major expansion at ∼12 My (*Lewis et al.*, 2008; *Zachos et al.*, 2008). Black crosses: global δ^{18}O record ($\frac{0}{00}$), five point smooth (*Zachos et al.*, 2008). Grey shading: global atmospheric CO_2 (ppm) reconstruction, 5 point smooth (*Royer*, 2014). Green line: *Nothofagidites* (type *Nothofagus fusca*) pollen abundance (count per grams dry weight, gdw^{-1}) measured in AND-2A core (*Feakins et al.*, 2012). The pollen abundance peak ∼16.4 My is further evidence that Nothofagus, those leaf fossils in Paleolake Friis sediments, existed on Antarctica during the MMCO. The dotted green line represents a sedimentary hiatus in the AND-2A core that is attributed to ice sheet growth.

Sample	**Sample depth (cm)**	**^{10}Be/^{9}Be (10^{-14} atoms atoms^{-1})**	**Error (10^{-14} atoms atoms^{-1})**	**[^{10}Be] (10^{5} atoms g^{-1})**	**1-σ error (10^{5} atoms g^{-1})**
Friis Hills Pit 1					
ANT-08-FH-03	0	110	1.8	150	3
ANT-08-FH-02	20	2.4	0.24	3.1	0.36
ANT-08-FH-01	60	0.3	0.06	0.03	0.1
Friis Hills Pit 2					
ANT-08-FH-05	26	0.1	0.04	-0.1	0.1
ANT-08-FH-04	30	0.2	0.11	-0.054	0.18
Chemical blanks					
1	N.A.	0.2	0.08	0.3	0.3
2	N.A.	0.2	0.09	0.3	0.3

Table 5.1: Meteoric ^{10}Be adhered to Paleolake Friis sediments.

Reference	**Material**	**Min-Max ε (m My^{-1})**	**Min-Max [^{10}Be]$_{initial}$ (atoms g^{-1} x 10^7)***
Nishiizumi et al. (1991)	Sandstone boulder	0.32-1.31	1.65-6.77
Summerfield et al. (1999)	Sandstone, granite boulders	0.133-1.02	2.12-16.28
Putkonen et al. (2008)	Regolith	2.1	1.03
Morgan et al. (2010)	Regolith	0.19-2.6	0.83-11.40
Dickinson et al. (2012)	Diamicton, sandstone	0.1-0.33	6.56-21.66
	Overall range	**0.1-2.6**	**0.83-22.0**
	Predicted age range (My)†		**11.0-17.5**

$\star$ Calculated using Eq. 5.1 and parameters as defined in text.
† Calculated using Eq. 5.2.

Table 5.2: Erosion rates used to estimate Paleolake Friis sediment age.

Location	**Sample type**	**Minimum [^{10}Be]* (atoms g^{-1})**	**Maximum [^{10}Be]* (atoms g^{-1})**	**Reference**
Lake Lisan (Dead Sea), Negev Desert, Israel	Bulk	0.78±0.03x10^{8}	1.64±0.07x10^{8}	*Belmaker et al.* (2008)
Lake Lehmilampi, Finland	Core	2.1x10^{8}	1.76x10^{9}	*Berggren et al.* (2013)
Anderson Pond, TN, USA	Core	2.16±0.13x10^{9}	2.90±0.13x10^{9}	*Brown et al.* (1987)
Lake Baikal, Russia	Core	5.07±0.39x10^{8}	1.13±0.05x10^{9}	*Horiuchi et al.* (1999)
Lake Baikal, Russia	Core	0.5x10^{9}	1.5x10^{9}	*Horiuchi et al.* (2000)
Lake Mega-Chad, North Africa	Paleolake	2.38±0.25x10^{6}	8.59±0.35x10^{7}	*Lebatard et al.* (2010)
Hillpiece Bog, Tristan da Cunha	Core	7.02±0.379x10^{8}	1.75±0.98x10^{9}	*Ljung et al.* (2007)
Union Lake, NJ, USA	Bulk	1.20±0.60x10^{7}	2.60±0.30x10^{10}	*Lundberg et al.* (1983)
Lake Keilambete, Australia	Bulk	0.76x10^{9}	2.31x10^{9}	*Raisbeck et al.* (1981)
Lake Windermere, England	Bulk	1.11x10^{9}	1.6x10^{9}	*Raisbeck et al.* (1981)
Lake Zurich, Switzerland	Sediment trap	4.96±0.32x10^{7}	2.54±0.20x10^{8}	*Schuler et al.* (1991)
Mono Lake, CA, USA	Bulk	0.7x10^{8}	4.1x10^{8}	*Ticich et al.* (1986)
Overall average† (atoms g^{-1})		2.38x10^{6}	2.90x10^{9}	
[^{10}Be]$_{initial}$ estimates at Friis Hills (atoms g^{-1})		8.3x10^{6}	2.2x10^{8}	

* Some measurements initially reported in dpm kg^{-1}. Converted to atoms g^{-1} using the following: dpm (decays per minute)= A (radioactive activity) and A=λN, where N=atoms of ^{10}Be and λ=5.0x10^{-7} y^{-1}.
† Not all values are published with associated error. As such, overall minimum and maximum [^{10}Be] are calculated without reported error. Where an external age estimator was provided, the effect of decay correction was calculated. Maximum decay corrected concentrations differ <3% from non-corrected values, and are not included in the overall average.

Table 5.3: Concentration ranges of meteoric ^{10}Be adhered to lake sediments worldwide.

CHAPTER 6 : Summary

This body of work utilizes and expands upon existing cosmogenic radionuclide (CRN) dating tools. Each chapter presents a dataset collected from a spatiotemporal transect, stretching from inner Dry Valleys, middle elevation sites of Miocene age, to mid-valley high elevation sites of Quaternary age, and finally to an offshore, marine site of Pliocene age. Each dataset presents a unique application of CRN dating, allowing us to construct chronologies closely linked with climatic shifts of varying magnitude and frequencies.

Here, I outline the major findings of each chapter and their contributions to the field of geochronology. I then make suggestions regarding future improvements and applications of each technique.

6.1. Difference Dating

In Chapter 3 I presented Difference Dating, a new method for dating glacial moraines. Difference Dating will prove especially useful in the Dry Valleys, Antarctica, where sluggish rates of geomorphic change preserve ancient landscapes and moraine boulders contain high levels of inheritance, prohibiting accurate deglaciation chronologies. Difference Dating was so-named for its measurement of the difference between expected and measured exposure ages of desert pavement clasts underlying moraine boulders.

The largest obstacles facing Difference Dating are:

- Difference Dating is inherently spatially limited. There are only so many clasts lying beneath each moraine boulder. Larger sample populations are preferred so as to properly identify outliers. In turn, this increases the sample procedure's cost.
- The sampling technique is physically demanding and requires the field party to overturn large, meter-scale moraine boulders and then return the boulders to their original positioning. Atop unstable deposits, this process may be made more challenging.

A primary goal moving forward will be to incorporate multi-nuclide systems to minimize age uncertainty. In quartz-bearing deposits, this includes the following pairs which are established for use in the Dry Valleys: ^{26}Al-^{10}Be, ^{21}Ne-^{10}Be (*Balco et al.*, 2014). For younger deposits (on the order of 10 ky), the ^{14}C-^{10}Be pair will prove very useful (*Goehring et al.*, 2011). Bayesian techniques should be considered when fitting burial isochrons, so as to minimize overall uncertainty (*Muzikar*, 2011; *Goehring et al.*, 2013). Ultimately, the applicability of any of these nuclide pairings will be limited by the rate of desert pavement formation (it is critical that pavement formation rate is less than the lifetime of the nuclide pair).

In Chapter 3, as a proof of concept, we made a first attempt at using Al-Be burial ages on high altitude cirque desert pavements. While the Al-Be burial ages were consistent with our modeled difference dates, the uncertainty is of the same order as the burial age itself. In this case, isochron burial dating could only ameliorate the problem to a certain extent, as the youngest deposits approach the analytical lower limit of Al$-$Be burial dating of $\sim$100 ky (*Granger*, 2006).

Additional sources of uncertainty in Difference Dating include those acquired from modeled shielding factors (f), nuclide measurements (N), and surface production rates [$P(0)$]. I suggest the following improvements to reduce the uncertainty associated with each variable:

- To limit shielding factor uncertainty, one may implement an automated modeling exercise (*Balco*, 2014). Much of the uncertainty deriving from f is human-error, incorporated into the Monte Carlo model as maximum likely error introduced via coarse field measurements and quasi-quantitative photogrammetry.

- Similarly, reducing N could be fairly straightforward using interlaboratory measurements. Because Dry Valleys cosmogenic radionuclide dosages are so high, the probability of micro-contamination in clean laboratory settings is increased. This is possible in our samples: though background levels are acceptable (in most cases $\ll$1% of overall

nuclide concentration), they may still be reduced farther. Interlaboratory comparisons will reveal the occurrence of this phenomenon.

- The final source of uncertainty in Difference Dating derives from P. This is more challenging to reduce, as it relies on the derivation of a localized production rate. The best areas to obtain this for the nuclides used, ^{26}Al and ^{10}Be, are high elevation bedrock surfaces which have been exposed much longer than the lifetime of either nuclide and have experienced negligible erosion. If this condition is met, then nuclide measurement is set by production alone ($\varepsilon \rightarrow 0$; see Eq. 2.4).

A final consideration for improving Difference Dating may be to expand its sampling material to sands. Just as cosmogenic radionuclide concentrations measured in exposed bedrock surfaces are a product of some long-term, "background" erosion rate, so too are the radionuclide concentrations measured from alluvial river sands (*Granger et al.*, 1996). In this sense, one could apply Difference Dating to sands that underlie and surround moraine boulders. This has the advantage of greatly reducing analytical cost, while still providing a mean nuclide concentration that incorporates potential outliers. Regarding the latter point, this may prove a more effective manner in which to quantify the impact of outlier clasts on mean nuclide concentration.

Such an approach is possible so long as the sand source is well understood. For example, in many regions of the Dry Valleys desert pavement clasts are underlain by finer silt sized vesicular layers that form as pavement clasts weather in place (*Bockheim*, 2010). This material could be a useful sampling target if collected and homogenized from the boulder's underlying pavement layer. In doing so, one would need to carefully calculate f to incorporate shielding from both the overlying boulder and the average pavement clast thickness. It is also prudent that, in such an application, pavements surrounding the boulder overlie vesicular layers formed in the same manner (i.e. from clasts weathering in place). A complication may occur if, for example, pavement formation proceeded via inflation, whereby eolian fines are lodged beneath surface clasts and raise them over time. (This final point is

not of concern at inner Wright Valley cirques, where pavements likely originate as glacial deflation lags.)

6.2. Authigenic $^{10}Be/^{9}Be$ as a proxy for East Antarctic Ice Sheet melt

In Chapter 4, I present a record of authigenic $^{10}Be/^{9}Be$ collected offshore Wilkes Land, East Antarctica. The usage of the $^{10}Be/^{9}Be$ ratio as a tracer of continental denudation and terrigenous flux is recast as a tool for monitoring East Antarctic Ice Sheet (EAIS) fluctuation and freshwater discharge during warm interglacial periods.

Such records must address potentially confounding scenarios, most importantly this includes the effect of changing mineralogy, grain size, surface area on Be (de)sorption, and the effects of bioproductivity, sediment focusing/winnowing, and production rates on apparent Be flux. In U1361a sediments, we address all of these issues, and posit that fluctuations in the $^{10}Be/^{9}Be$ record are likely a result of pulsed freshwater discharging during warm interglacials.

Thanks to extensive data collection during and following ocean cruises around the continent, much of the supporting data that are needed to address these confounding effects already exist (clay mineralogy, grain size measurements, XRF scans, etc.). We suggest revisiting archived marine sediment cores of similar age and sampling for ^{10}Be, ^{9}Be; this will strengthen our understanding of Be delivery to the Southern Ocean during Pliocene interglacials. Of particular use would be a marine core nearby U1361a, to confirm the impact of freshwater discharge on the Be isotope content in Antarctic Bottom Water forming in the Adélie Depression. To best explore the impacts of sedimentation and bioproductivity on the $^{10}Be/^{9}Be$ ratio, these additional cores would preferably differ from U1361a sediments in the following ways:

- The additional core should have a different long-term sedimentation rate. It, like U1361a Pliocene age sediments, must also lack signs of sediment sorting. If these conditions are met, we can compare the effects of sediment focusing on the $^{10}Be/^{9}Be$

record. [Typically, sediment focusing is corrected for by normalizing ^{10}Be with ^{230}Th [though the simple interpretation of this normalization procedure is questioned on the basis of differing partition coefficients of ^{10}Be and ^{230}Th on opal (*Chase et al.*, 2002)]. Ideally, we would like to use ^{10}Be through its fullest possible age extent through the late Miocene, but the use of ^{230}Th is limited to ∼600 ky.]

- The additional core should have a record of bioproductivity unique from that of U1361a, such as higher- or lower-on-average diatom abundance. If this condition is met, we can better explore the effect of bioproductivity on Be scavenging. Research questions of interest may include, "How does Be scavenging scale with increasing opal abundance in the Southern Ocean?" and, "How does Be affinity for opal change in the presence of lithogenics?"

Finally, future applications of our diatom separation technique should prioritize deposits with great enough diatom abundance to measure [^{10}Be] (∼100 mg) (*Lal et al.*, 2006). Measuring opal and authigenic ^{10}Be/^{9}Be from the same depth interval may allow for the reconstruction of ^{10}Be/^{9}Be depth profiles in seawater, which is particularly exciting to consider in regions of deep water formation. (While diatom frustule mineralization is limited to the shallow photic zone, authigenic mineral precipitation may better represent a depth-integrated average Be load of the overlying water column.) This approach requires consideration of the timing of diatom frustule mineralization versus authigenic mineral precipitation.

6.3. Extending the upper age limit of meteoric ^{10}Be in paleolake sediments

In Chapter 5, I present a record of extremely low [^{10}Be] in paleolake deposits collected from atop the Friis Hills, Dry Valleys, Antarctica. We provide one of only two published records which use meteoric ^{10}Be to date paleolake sediments. We use a novel approach to construct a chronology based on these concentrations and the presence of other paleoclimatic indicators, such as *Nothofagus* leaf impressions and beetle carcasses, and posit that Paleolake Friis formed during the middle Miocene Climatic Optimum, 14-17.5 My.

The observation of background meteoric [^{10}Be] is astounding and, if observed again in buried paleosols or paleolake deposits, will provide a lower age limit of $\sim$14 My on the last time since meteoric waters percolated to that layer's depth or since lake drainage, respectively. Ultimately, the Paleolake Friis chronology was made possible by the presence of other paleoclimatic indicators. Without these data, it would be unreasonable to assign a definitive age to the paleolake sediments.

APPENDIX A: Specific surface area, XRD, SEM, and grain size analyses mentioned in text

This material is meant to supplement Chapter 4: $^{10}Be/^{9}Be$ ratios reflect East Antarctic Ice Sheet mass changes: a record offshore the Wilkes Subglacial Basin. The possible control of surface area on [^{10}Be] is considered using specific surface area measurements collected with the Brunauer, Emmett and Teller (BET) method. Diatom cleanliness is assessed using x-ray diffraction (XRD) and scanning electron microscopy (SEM).

Specific surface area measurements

Sample specific surface area is measured using the University of Pennsylvania Earth and Environmental Science Department's MicroMeritics Tri-Star BET Analyzer. The BET method is based on gas adsorption to multi-layer mineral surfaces. Prior to analysis, 0.5 g sample aliquots are freeze-dried, homogenized gently using a mortar and pestle, then purged under vacuum with nitrogen gas.

We do not observe a statistically significant correlation between authigenic Be isotopes and BET surface area; see Table 4.2. See Table A.1 for comparison of Be isotope concentrations and corresponding BET surface area.

X-ray diffraction

X-ray diffraction spectra were obtained using a PANAlytical X'Pert PRO diffractometer equipped with an X'Celerator detector (Co-Kαradiation at 40 kV, 40 mA) operating in isothermal mode (25°C) at the University of Pennsylvania. The incident beam optical module PANalytical Bragg- BrentanoHD was used to improve the peak-to-background ratio and increase intensity in measured spectra. Samples were filled into Mark-tubes (Lindemann special glass, with a nominal outside diameter of 0.3 mm and a wall thickness of 0.01 mm) for capillary spinner-mode analysis. Data were collected with a scan range between 3 and 70° 2θ, a step size of 0.008° 2θ, a divergence slit of 1/8°, anti-scatter slits of 1/16°, and

Soller slits of 0.04 rad. The fitted peak width for collected data was about 0.01° 2θ.

We analyze all diatom separates to confirm that our cleaning procedure was effective (see Section 4.3.2). For reference, we also analyze three bulk samples (Samples 1, 6 and 15) to identify major mineral phases. We find bulk sample analysis matches well with previous studies of clay mineralogy at/near U1361a (*Cook et al.*, 2013; *Damiani et al.*, 2006; *Verma et al.*, 2014).

See Fig. A.1 for a comparison of Sample 15, bulk sample versus cleaned diatom separate. See Figs. A.2 and A.3 for XRD scans of cleaned diatom separates collected from interglacial sediments. See Fig. A.4 for XRD scans of Sample 22, size fractions 2-5μm, 5-10μm, and >10μm. See Fig. A.5 for XRD scans of bulk Samples 1 and 6.

Scanning electron microscopy

Sample imaging is carried out using the Singh Center for Nanotechnology's FEI Quanta 600 field emission gun (FEG) Mark II Environmental Scanning Electron Microscope (SEM). We image two samples after diatom separation, Sample 15 and 22. These samples were selected for SEM imaging simply because they had the greatest mass. Following microfiltration, and prior to SEM imaging, all size fractions of Sample 15 are aggregated and homogenized (gentle mixing in sample container). We image Sample 22 size fractions <2, 2-5, 5-10, and >10μm independently. Doing so allows us to confirm that clay minerals are accumulating in the smallest size fraction (<2μm), which is removed prior to dissolution and ^{9}Be analysis (see Section 4.3.2). Imaging individual size fractions also allows us to determine whether or not the cleaning method could separate individual diatom species (based on size and shape) (*Minoletti et al.*, 2008).

SEM images yield two important findings. First, we observe minimal clay content in size fractions >2μm, confirming that the majority of clays are removed during our diatom separation procedure and ensuring that ^{9}Be originates from dissolved diatoms and not from lithogenics. Secondly, we observe that diatom frustules are badly broken, likely reflecting

several scenarios such as diagenesis (e.g., compaction), transportation, and/or energetic deposition (turbidity currents deliver sediment to U1361a site). Thus, these samples are not ideal to test size and shape separation using microfiltration.

See Figs. A.6, A.7, A.8, A.9 and A.10 for representative SEM images of Samples 15 and 22.

Grain size analyses

We measure the grain size of U1361a sediments on Montclair State University's laser particle size analyzer (Malvern Mastersizer 2000). Grain size frequencies indicate slightly greater clay and slightly less silt content in diatom-poor sediments as opposed to diatom-rich sediments. We use standard deviations of grain size distributions based on Folk and Ward's (1968) classic sorting classification scheme. Values 2-4 indicate very poor sorting; values >4 indicate extremely poor sorting. All U1361a sediments have phi standard deviations >2, confirming an absence of grain size sorting processes.

See Fig. A.11 for grain size frequency plots and standard deviation values of diatom-rich and diatom-poor sediments.

Sample*	BET Surface Area (m^2 g^{-1})
01	60.92 ± 0.52
02	39.37 ± 0.35
03	37.91 ± 0.36
04	41.48 ± 0.33
05	31.75 ± 0.22
06-R1	33.03 ± 0.19
06-R2	33.47 ± 0.24
06-R3	33.06 ± 0.22
07	32.28 ± 0.21
08	59.09 ± 0.38
09	35.96 ± 0.20
10	43.57 ± 0.31
11	40.14 ± 0.36
12-R1	42.04 ± 0.38
12-R2	46.34 ± 0.47
12-R3	45.78 ± 0.45
13	37.42 ± 0.33
14	40.61 ± 0.25
15	41.05 ± 0.39
16	32.69 ± 0.35
17	49.90 ± 0.44
18	42.73 ± 0.40
19	44.36 ± 0.37
20-R1	33.09 ± 0.26
20-R2	32.60 ± 0.31
20dup-R1	27.97 ± 0.25
20dup-R2	27.56 ± 0.24
21	46.58 ± 0.38
22	21.40 ± 0.26

* Replicate samples indicated by "-R#."
Duplicate samples indicated by "dup."

Table A.1: Authigenic Be isotopes and BET surface area U1361a sediments. Note: Sample 20dup is a duplicate of Sample 20, but contained a dropstone. As expected, the dropstone lowers the overall surface area of the sample. The dropstone was included in Sample 20dup authigenic leaching (see Table 4.1).

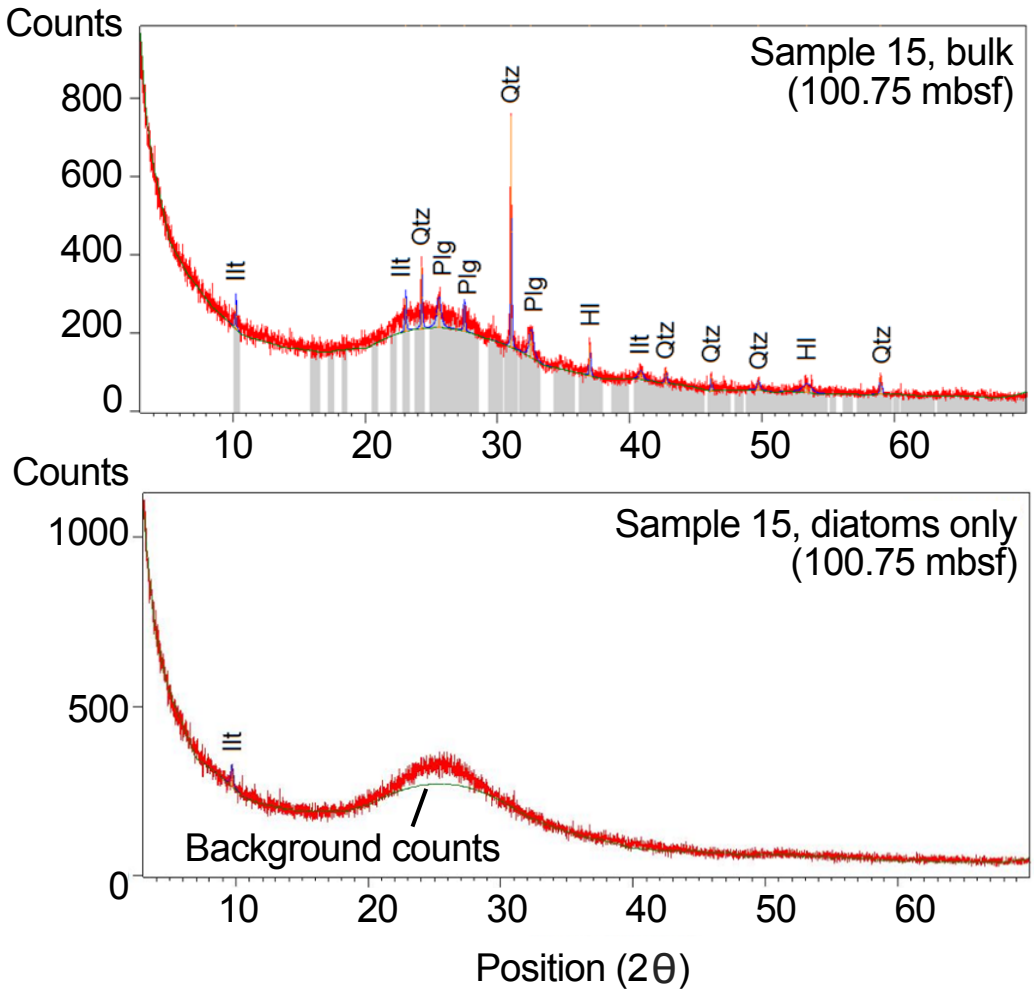

Figure A.1: XRD spectra of bulk and diatom separates of Sample 15. In bulk fraction, note abundance of common minerals quartz (Qtz), plagioclase (Plg), and illite (Ilt). Also present is halite (Hl). In cleaned diatom fraction, note weak peak of illite and a broad area between 20° and 30°2θ related to abundant amorphous content (i.e. biogenic opal).

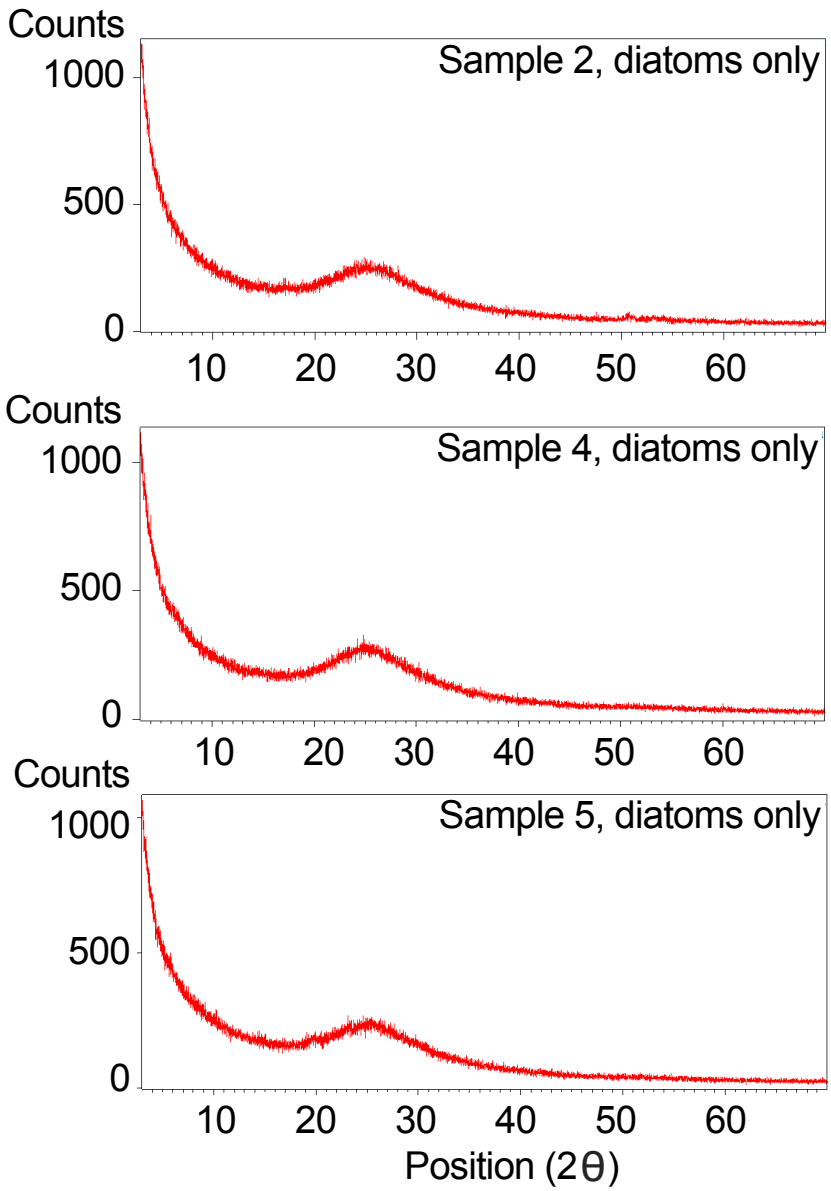

Figure A.2: XRD spectra of cleaned diatom separates of Samples 2, 4, 5. Note broad area between 20° and 30°2θ related to abundant amorphous content (i.e. biogenic opal).

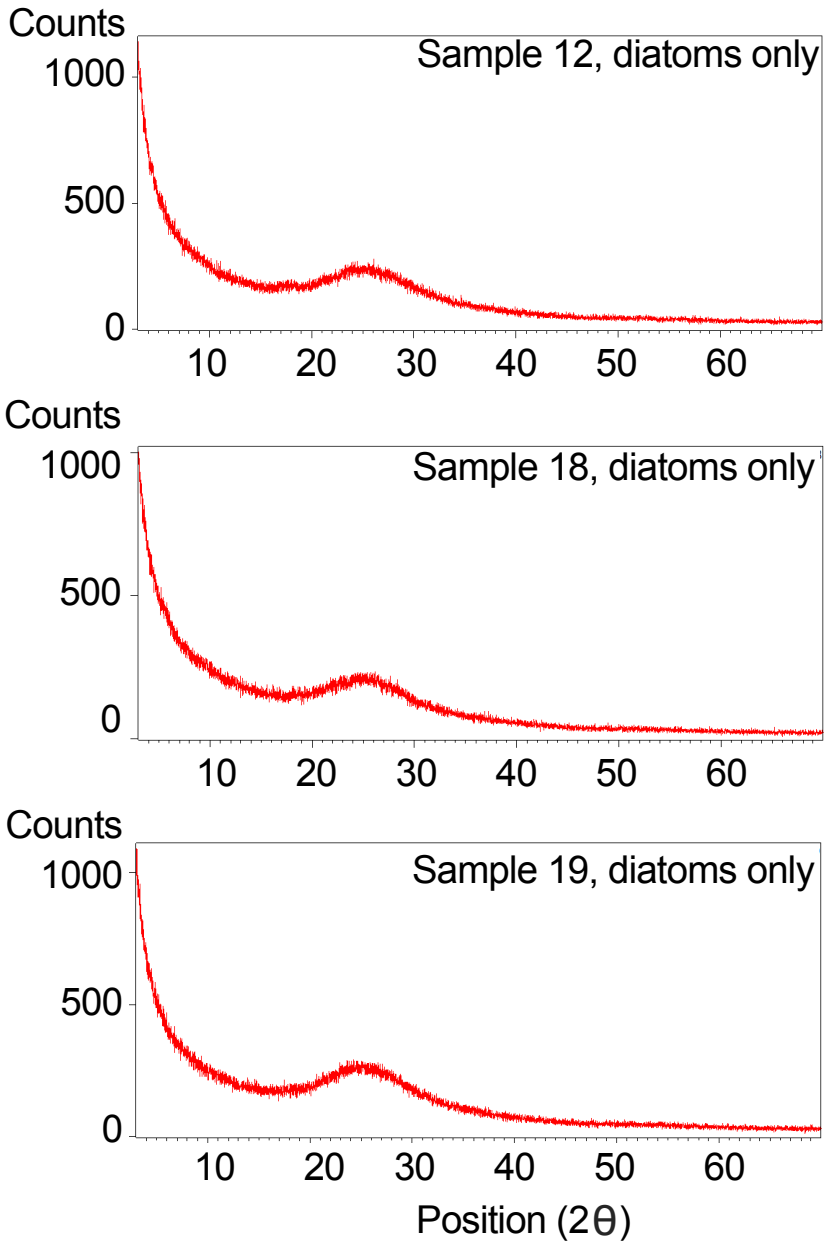

Figure A.3: XRD spectra of cleaned diatom separates of Samples 12, 18, and 19. Note broad area between 20° and 30°2θ related to abundant amorphous content (i.e. biogenic opal).

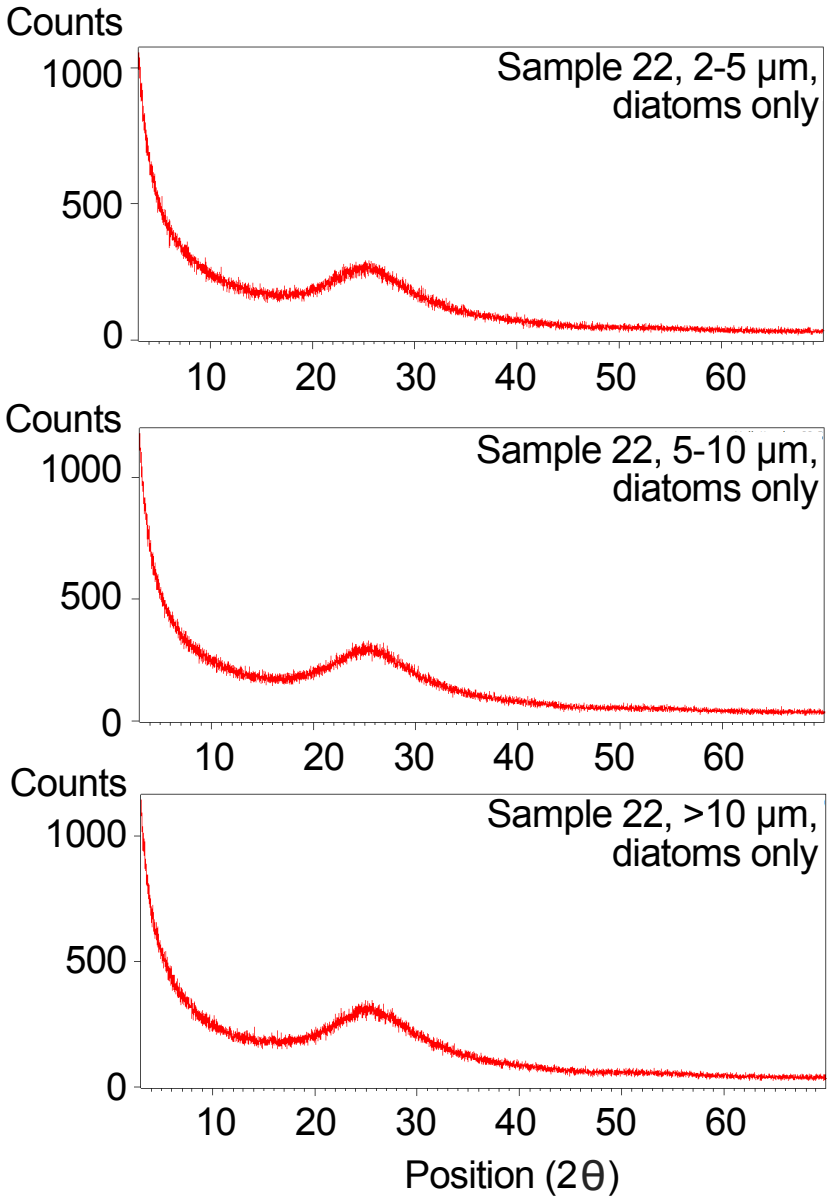

Figure A.4: XRD spectra of cleaned diatom separates of Sample 22, size fractions 2-5μm, 5-10μm, and >10μm. Note broad area between 20° and 30°2θ related to abundant amorphous content (i.e. biogenic opal).

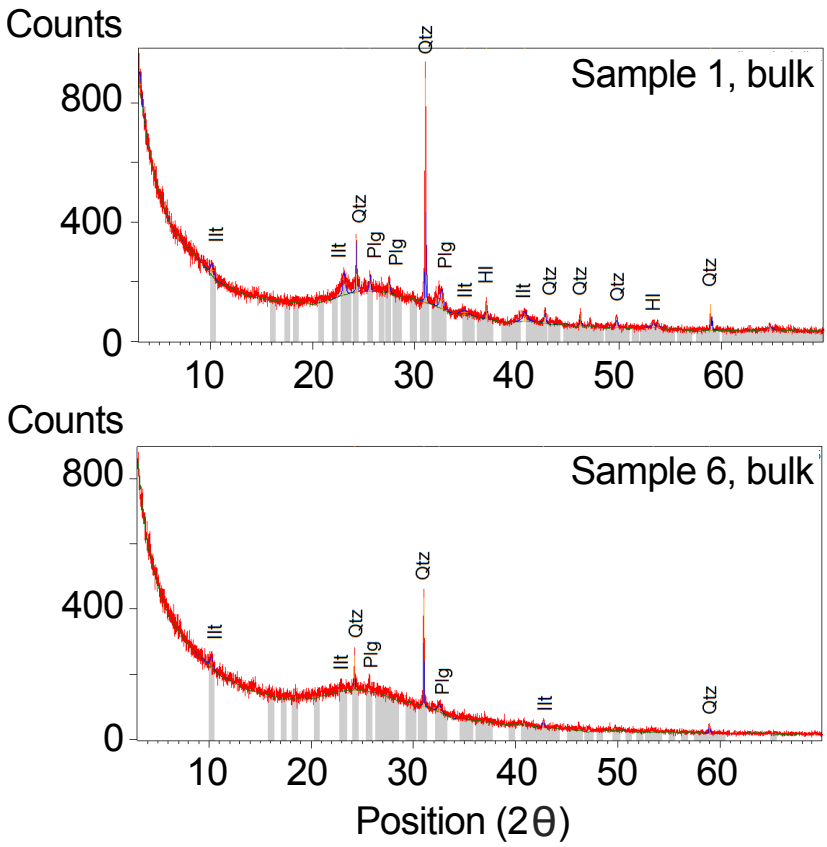

Figure A.5: XRD analyses of bulk samples 1 and 6 (prior to diatom separation). Note abundance of illite (Ilt), quartz (Qtz), and plagioclase (Plg). Halite (Hl) is also present in sample 1.

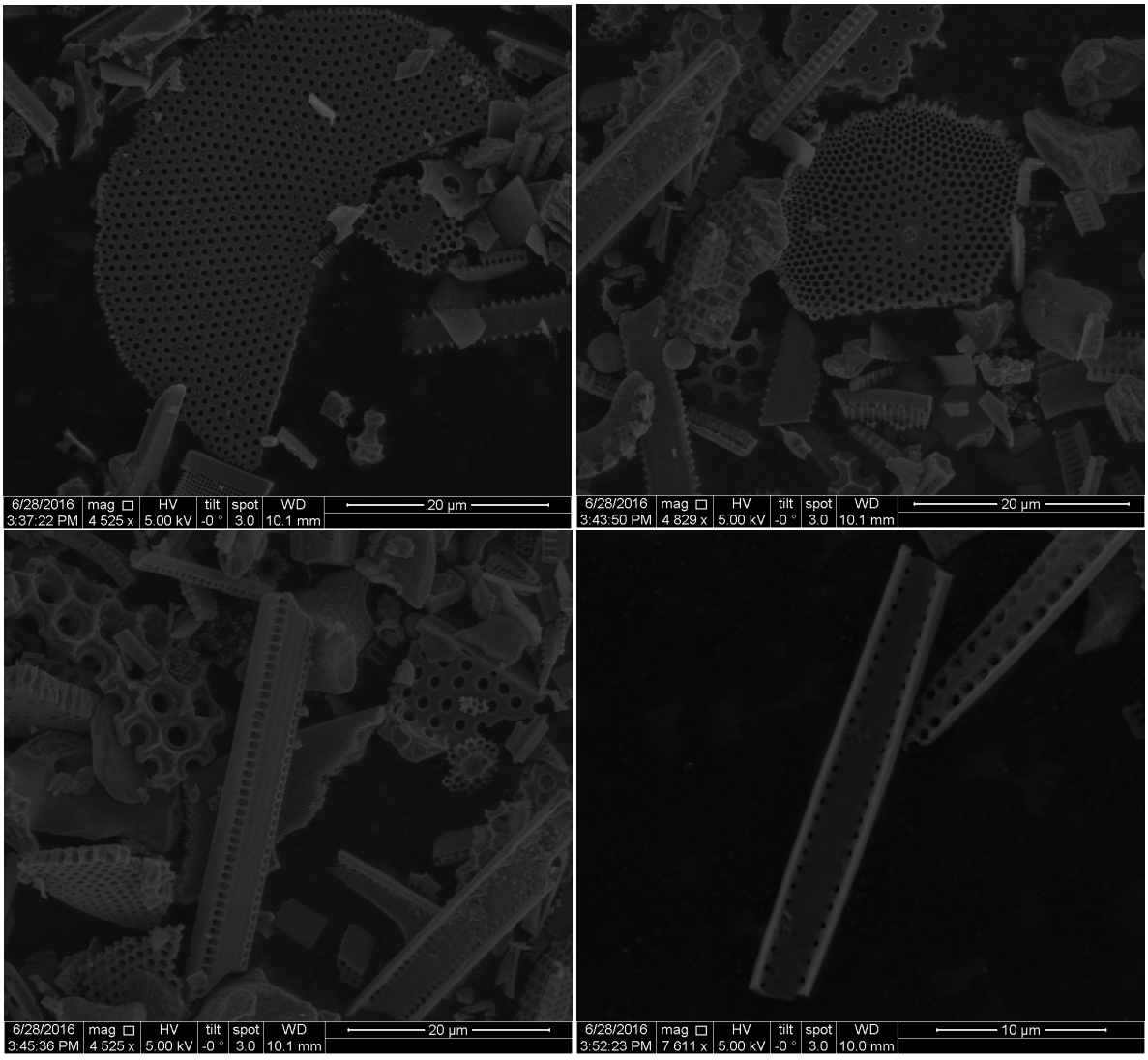

Figure A.6: Assemblage of SEM-derived image of Sample 15 diatoms after cleaning procedure.

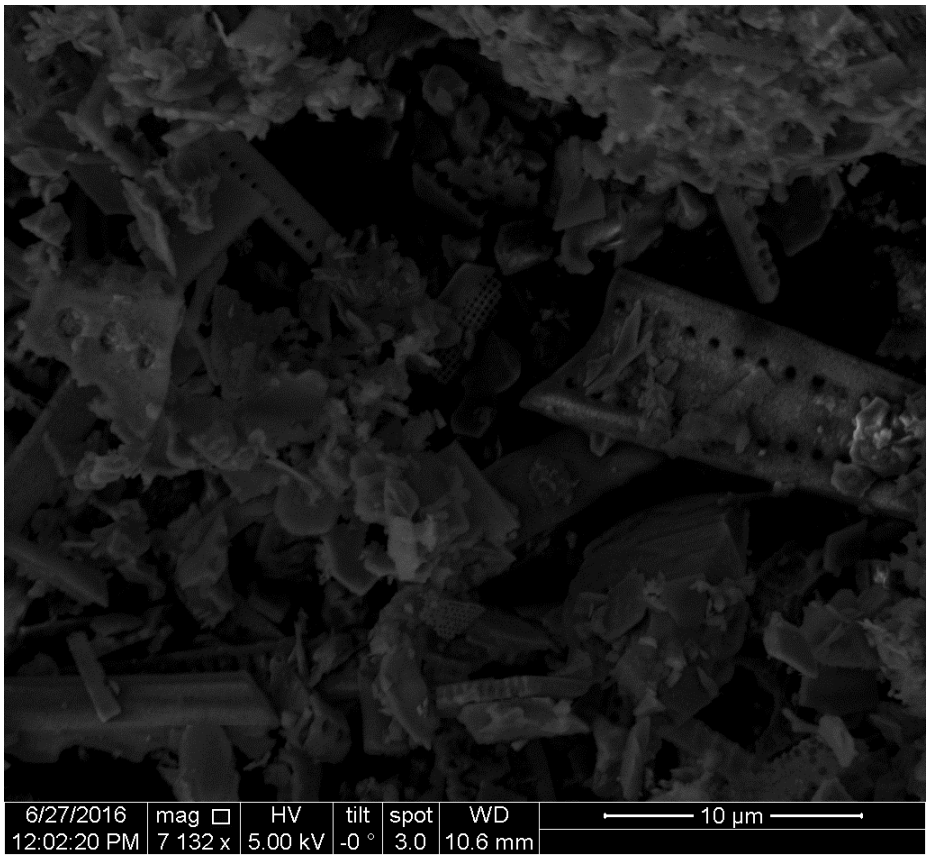

Figure A.7: Sample 22, SEM image of $<2\mu$m fraction. Note abundance of clay.

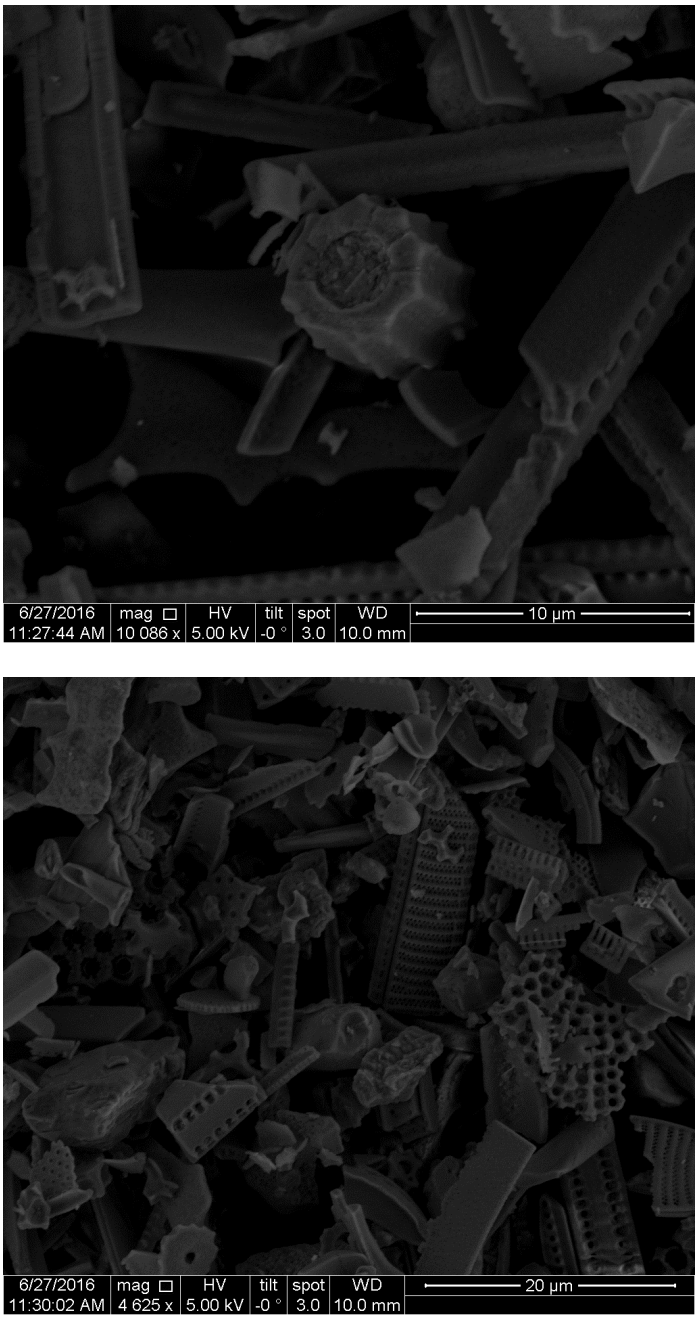

Figure A.8: Sample 22, SEM image of 2-5μm fraction.

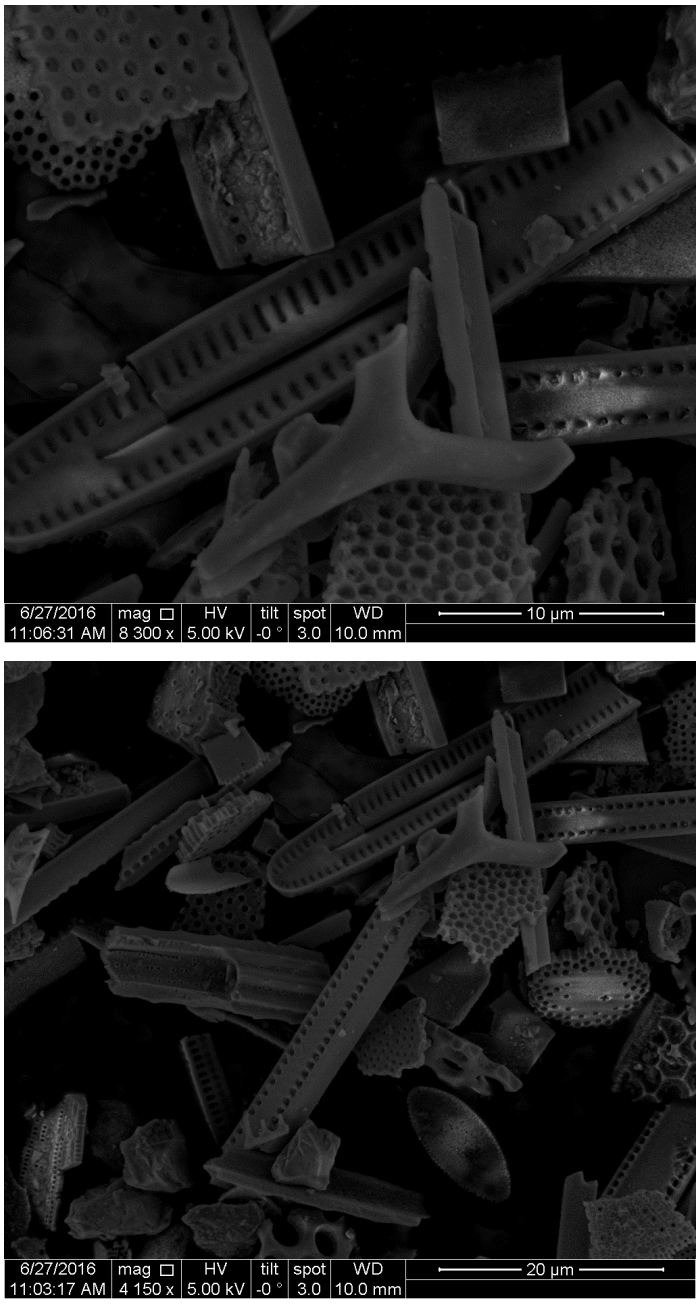

Figure A.9: Sample 22, SEM image of 5-10μm fraction.

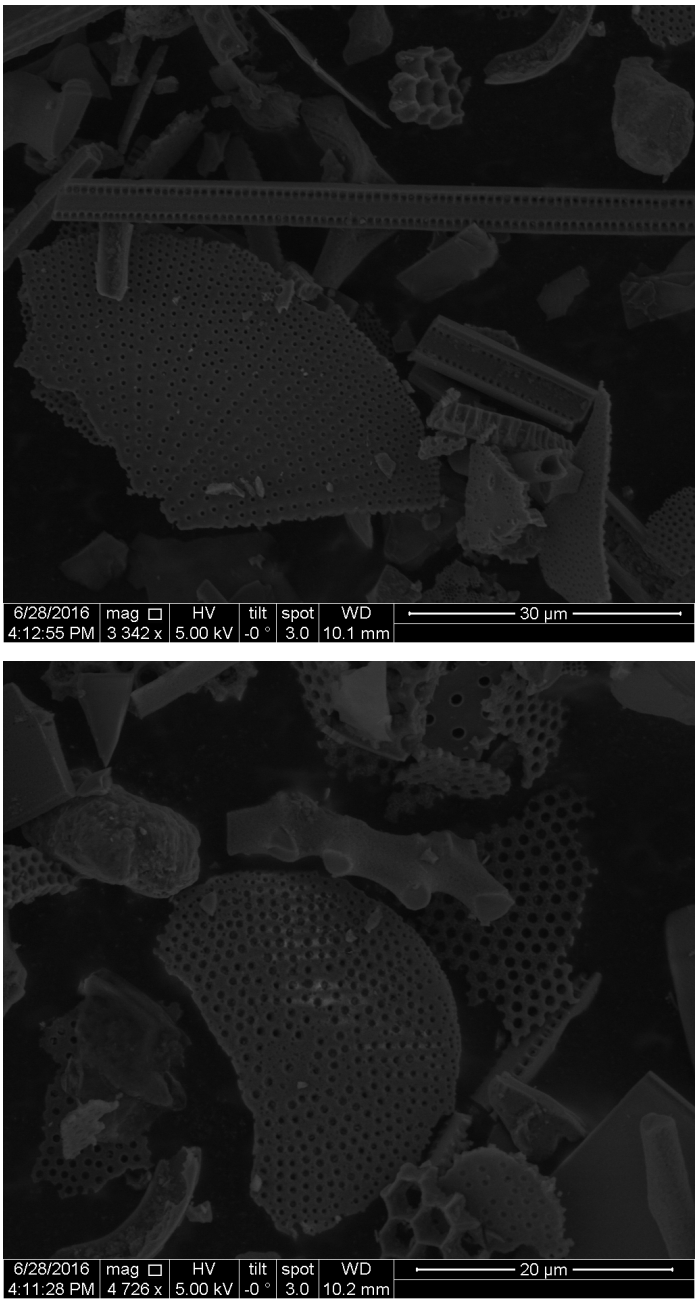

Figure A.10: Sample 22, SEM image of $>10\mu$m fraction.

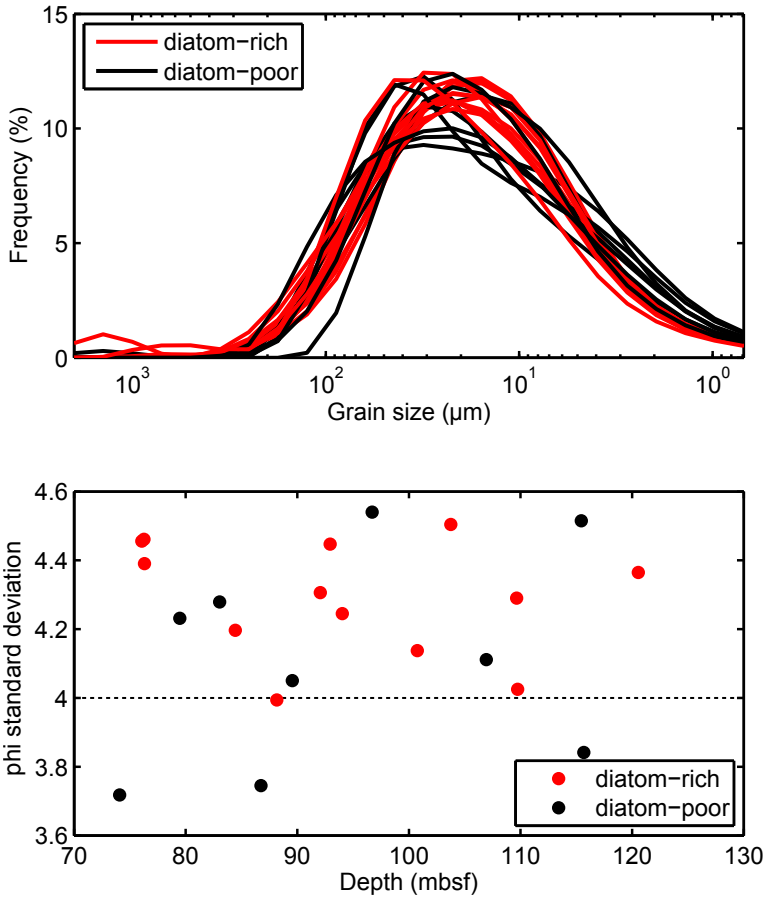

Figure A.11: U1361a grain size data. Top panel: grain size frequency plots of diatom-rich (interglacial) and diatom-poor (glacial) sediments. Note reverse x-axis and slightly greater abundance of clays in interglacial sediments. Bottom panel: phi standard deviation values of diatom-rich and diatom-poor sediments. Values 2-4ϕ=very poorly sorted, ¿4ϕ=extremely poorly sorted.

BIBLIOGRAPHY

Ackert Jr., R. P., and M. D. Kurz (2004), Age and uplift rates of Sirius Group sediments in the Dominion Range, Antarctica, from surface exposure dating and geomorphology, *Global and Planetary Change*, *42*(14), 207–225, doi:10.1016/j.gloplacha.2004.02.001.

Aldahan, A., and G. Possnert (2003), Geomagnetic and climatic variability reflected by 10Be during the Quaternary and late Pliocene, *Geophysical Research Letters*, *30*(6), 1301, doi:10.1029/2002GL016077.

Aldahan, A., Y. Haiping, and G. Possnert (1999), Distribution of beryllium between solution and minerals (biotite and albite) under atmospheric conditions and variable pH, *Chemical Geology*, *156*(14), 209–229, doi:10.1016/S0009-2541(98)00186-7.

Aldahan, A. A., S. Ning, G. Possnert, J. Backman, and K. Bostrm (1997), 10Be records from sediments of the Arctic Ocean covering the past 350 ka, *Marine Geology*, *144*(1), 147–162, doi:10.1016/S0025-3227(97)00084-4.

Anderson, R. S., J. L. Repka, and G. S. Dick (1996), Explicit treatment of inheritance in dating depositional surfaces using in situ 10Be and 26Al, *Geology*, *24*(1), 47–51, doi:10.1130/0091-7613(1996)024⟨0047:ETOIID⟩2.3.CO;2.

Applegate, P., N. Urban, K. Keller, T. Lowell, B. Laabs, M. Kelly, and R. Alley (2012), Improved moraine age interpretations through explicit matching of geomorphic process models to cosmogenic nuclide measurements from single landforms, *Quaternary Research*, *77*(2), 293–304, doi:10.1016/j.yqres.2011.12.002.

Atkins, C. B. (2013), Geomorphological evidence of cold-based glacier activity in South Victoria Land, Antarctica, *Geological Society, London, Special Publications*, *381*(1), 299–318, doi:10.1144/SP381.18.

Balco, G. (2011), Contributions and unrealized potential contributions of cosmogenic-nuclide exposure dating to glacier chronology, 19902010, *Quaternary Science Reviews*, *30*(1-2), 3–27, doi:10.1016/j.quascirev.2010.11.003.

Balco, G. (2014), Simple computer code for estimating cosmic-ray shielding by oddly shaped objects, *Quaternary Geochronology*, *22*, 175–182, doi:10.1016/j.quageo.2013.12.002.

Balco, G., and C. W. Rovey (2008), An isochron method for cosmogenic-nuclide dating of buried soils and sediments, *American Journal of Science*, *308*(10), 1083–1114, doi:10.2475/10.2008.02.

Balco, G., and D. L. Shuster (2009), Production rate of cosmogenic 21Ne in quartz estimated from 10Be, 26Al, and 21Ne concentrations in slowly eroding Antarctic bedrock surfaces, *Earth and Planetary Science Letters*, *281*(12), 48–58, doi:10.1016/j.epsl.2009.02.006.

Balco, G., J. O. H. Stone, and J. A. Mason (2005), Numerical ages for Plio-Pleistocene

glacial sediment sequences by 26Al/10Be dating of quartz in buried paleosols, *Earth and Planetary Science Letters*, *232*(12), 179–191, doi:10.1016/j.epsl.2004.12.013.

Balco, G., J. O. Stone, N. A. Lifton, and T. J. Dunai (2008), A complete and easily accessible means of calculating surface exposure ages or erosion rates from 10Be and 26Al measurements, *Quaternary Geochronology*, *3*(3), 174–195, doi:10.1016/j.quageo.2007.12.001.

Balco, G., J. O. Stone, M. G. Sliwinski, and C. Todd (2014), Features of the glacial history of the Transantarctic Mountains inferred from cosmogenic 26Al, 10Be and 21Ne concentrations in bedrock surfaces, *Antarctic Science*, *26*(Special Issue 06), 708–723, doi:10.1017/S0954102014000261.

Bamber, J. L., et al. (2013), A new bed elevation dataset for Greenland, *The Cryosphere*, *7*(2), 499–510, doi:10.5194/tc-7-499-2013.

Barrett, P. J. (2013), Resolving views on Antarctic Neogene glacial history the Sirius debate, *Earth and Environmental Science Transactions of the Royal Society of Edinburgh*, *104*(01), 31–53, doi:10.1017/S175569101300008X.

Barrett, P. J., C. J. Adams, W. C. Mclntosh, C. C. Swisher, and G. S. Wilson (1992), Geochronological evidence supporting Antarctic deglaciation three million years ago, *Nature*, *359*(6398), 816–818, doi:10.1038/359816a0.

Belmaker, R., B. Lazar, N. Tepelyakov, M. Stein, and J. Beer (2008), 10Be in Lake Lisan sediments A proxy for production or climate?, *Earth and Planetary Science Letters*, *269*(34), 448–457, doi:10.1016/j.epsl.2008.02.032.

Benedetti, L. C., and J. van der Woerd (2014), Cosmogenic Nuclide Dating of Earthquakes, Faults, and Toppled Blocks, *Elements*, *10*(5), 357–361, doi:10.2113/gselements.10.5.357.

Berggren, A.-M., A. Aldahan, G. Possnert, E. Haltia-Hovi, and T. Saarinen (2013), Linking ice sheet and lake sediment archives of 10Be, 14681980 CE, *Nuclear Instruments and Methods in Physics Research Section B: Beam Interactions with Materials and Atoms*, *294*, 524–529, doi:10.1016/j.nimb.2012.05.024.

Bibby, T., J. Putkonen, D. Morgan, G. Balco, and D. L. Shuster (2016), Million year old ice found under meter thick debris layer in Antarctica, *Geophysical Research Letters*, p. 2016GL069889, doi:10.1002/2016GL069889.

Bockheim, J. G. (2010), Evolution of desert pavements and the vesicular layer in soils of the Transantarctic Mountains, *Geomorphology*, *118*(3-4), 433–443, doi:10.1016/j.geomorph.2010.02.012.

Borchers, B., et al. (2015), Geological calibration of spallation production rates in the CRONUS-Earth project, *Quaternary Geochronology*, doi:10.1016/j.quageo.2015.01.009.

Borchers, B., et al. (2016), Geological calibration of spallation production rates in the CRONUS-Earth project, *Quaternary Geochronology*, *31*, 188–198, doi:10.1016/j.quageo.2015.01.009.

Boschi, V. (2016), Characterization of the Physical and Chemical Controls on the Environmental Geochemical Behavior of Beryllium, *Publicly Accessible Penn Dissertations*.

Bourles, D., G. M. Raisbeck, and F. Yiou (1989), 10Be and 9Be in marine sediments and their potential for dating, *Geochimica et Cosmochimica Acta*, *53*(2), 443–452, doi:10.1016/0016-7037(89)90395-5.

Brocard, G. Y., P. A. van der Beek, D. L. Bourls, L. L. Siame, and J. L. Mugnier (2003), Long-term fluvial incision rates and postglacial river relaxation time in the French Western Alps from 10Be dating of alluvial terraces with assessment of inheritance, soil development and wind ablation effects, *Earth and Planetary Science Letters*, *209*(12), 197–214, doi:10.1016/S0012-821X(03)00031-1.

Brook, E. J., M. D. Kurz, R. P. Ackert, G. H. Denton, E. T. Brown, G. M. Raisbeck, and F. Yiou (1993), Chronology of Taylor Glacier Advances in Arena Valley, Antarctica, Using in Situ Cosmogenic 3He and 10Be, *Quaternary Research*, *39*(1), 11–23, doi:10.1006/qres.1993.1002.

Brown, E. T., J. M. Edmond, G. M. Raisbeck, F. Yiou, M. D. Kurz, and E. J. Brook (1991), Examination of surface exposure ages of Antarctic moraines using in situ produced 10Be and 26Al, *Geochimica et Cosmochimica Acta*, *55*(8), 2269–2283, doi:10.1016/0016-7037(91)90103-C.

Brown, E. T., C. I. Measures, J. M. Edmond, D. L. Bourls, G. M. Raisbeck, and F. Yiou (1992), Continental inputs of beryllium to the oceans, *Earth and Planetary Science Letters*, *114*(1), 101–111, doi:10.1016/0012-821X(92)90154-N.

Brown, T. A., D. E. Nelson, J. R. Southon, and J. S. Vogel (1987), 10Be production rate variations as recorded in a mid-latitude lake sediment, *Nuclear Instruments and Methods in Physics Research Section B: Beam Interactions with Materials and Atoms*, *29*(1-2), 232–237.

Caburlotto, A., R. G. Lucchi, L. De Santis, P. Macr, and R. Tolotti (2010), Sedimentary processes on the Wilkes Land continental rise reflect changes in glacial dynamic and bottom water flow, *International Journal of Earth Sciences*, *99*(4), 909–926, doi:10.1007/s00531-009-0422-8.

Cardinal, D., N. Savoye, T. W. Trull, F. Dehairs, E. E. Kopczynska, F. Fripiat, J.-L. Tison, and L. Andr (2007), Silicon isotopes in spring Southern Ocean diatoms: Large zonal changes despite homogeneity among size fractions, *Marine Chemistry*, *106*(12), 46–62, doi:10.1016/j.marchem.2006.04.006.

Chase, Z., R. F. Anderson, M. Q. Fleisher, and P. W. Kubik (2002), The influence of particle

composition and particle flux on scavenging of Th, Pa and Be in the ocean, *Earth and Planetary Science Letters*, *204*(12), 215–229, doi:10.1016/S0012-821X(02)00984-6.

Chmeleff, J., F. von Blanckenburg, K. Kossert, and D. Jakob (2010), Determination of the 10Be half-life by multicollector ICP-MS and liquid scintillation counting, *Nuclear Instruments and Methods in Physics Research Section B: Beam Interactions with Materials and Atoms*, *268*(2), 192–199, doi:10.1016/j.nimb.2009.09.012.

Christl, M., C. Strobl, and A. Mangini (2003), Beryllium-10 in deep-sea sediments: a tracer for the Earth's magnetic field intensity during the last 200,000 years, *Quaternary Science Reviews*, *22*(57), 725–739, doi:10.1016/S0277-3791(02)00195-6.

Christl, M., J. Lippold, F. Steinhilber, F. Bernsdorff, and A. Mangini (2010), Reconstruction of global 10Be production over the past 250ka from highly accumulating Atlantic drift sediments, *Quaternary Science Reviews*, *29*(19-20), 2663–2672, doi:10.1016/j.quascirev.2010.06.017.

Cook, C. P., et al. (2013), Dynamic behaviour of the East Antarctic ice sheet during Pliocene warmth, *Nature Geoscience*, *6*(9), 765–769, doi:10.1038/ngeo1889.

Cooke, R. U. (1970), Stone Pavements in Deserts, *Annals of the Association of American Geographers*, *60*(3), 560–577, doi:10.1111/j.1467-8306.1970.tb00741.x.

Corbett, L. B., P. R. Bierman, D. H. Rood, M. W. Caffee, N. A. Lifton, and T. E. Woodruff (2017), Cosmogenic 26Al/10Be surface production ratio in Greenland, *Geophysical Research Letters*, *44*(3), 2016GL071276, doi:10.1002/2016GL071276.

Cuffey, K. M., H. Conway, A. M. Gades, B. Hallet, R. Lorrain, J. P. Severinghaus, E. J. Steig, B. Vaughn, and J. W. C. White (2000), Entrainment at cold glacier beds, *Geology*, *28*(4), 351, doi:10.1130/0091-7613(2000)28⟨351:EACGB⟩2.0.CO;2.

Damiani, D., G. Giorgetti, and I. M. Turbanti (2006), Clay mineral fluctuations and surface textural analysis of quartz grains in PlioceneQuaternary marine sediments from Wilkes Land continental rise (East-Antarctica): Paleoenvironmental significance, *Marine Geology*, *226*(34), 281–295, doi:10.1016/j.margeo.2005.11.002.

Davis, P. T., J. P. Briner, R. D. Coulthard, R. W. Finkel, and G. H. Miller (2006), Preservation of Arctic landscapes overridden by cold-based ice sheets, *Quaternary Research*, *65*(1), 156–163, doi:10.1016/j.yqres.2005.08.019.

DeConto, R. M., and D. Pollard (2003), A coupled climateice sheet modeling approach to the Early Cenozoic history of the Antarctic ice sheet, *Palaeogeography, Palaeoclimatology, Palaeoecology*, *198*(1-2), 39–52, doi:10.1016/S0031-0182(03)00393-6.

DeConto, R. M., and D. Pollard (2016), Contribution of Antarctica to past and future sea-level rise, *Nature*, *531*(7596), 591–597, doi:10.1038/nature17145.

Desilets, D., M. Zreda, and T. Prabu (2006), Extended scaling factors for in situ cosmogenic nuclides: New measurements at low latitude, *Earth and Planetary Science Letters*, *246*(34), 265–276, doi:10.1016/j.epsl.2006.03.051.

Dickinson, W. W., M. Schiller, B. G. Ditchburn, I. J. Graham, and A. Zondervan (2012), Meteoric Be-10 from Sirius Group suggests high elevation McMurdo Dry Valleys permanently frozen since 6Ma, *Earth and Planetary Science Letters*, *355-356*, 13–19, doi:10.1016/j.epsl.2012.09.003.

Dixon, J. L., and C. S. Riebe (2014), Tracing and Pacing Soil Across Slopes, *Elements*, *10*(5), 363–368, doi:10.2113/gselements.10.5.363.

Dolan, A. M., A. M. Haywood, D. J. Hill, H. J. Dowsett, S. J. Hunter, D. J. Lunt, and S. J. Pickering (2011), Sensitivity of Pliocene ice sheets to orbital forcing, *Palaeogeography, Palaeoclimatology, Palaeoecology*, *309*(1-2), 98–110, doi:10.1016/j.palaeo.2011.03.030.

Doran, P. T., R. A. Wharton, and W. B. Lyons (1994), Paleolimnology of the McMurdo Dry Valleys, Antarctica, *Journal of Paleolimnology*, *10*, 85–114.

Dowsett, H. J. (2007), The PRISM palaeoclimate reconstruction and Pliocene sea-surface temperature, in *Deep-time perspectives on climate change: Marrying the signal from computer models and biological proxies*, micropalaeontological society special publication ed., pp. 459–480, Geological Society of London, London.

Dunai, T. J. (2001), Influence of secular variation of the geomagnetic field on production rates of in situ produced cosmogenic nuclides, *Earth and Planetary Science Letters*, *193*(12), 197–212, doi:10.1016/S0012-821X(01)00503-9.

Dunai, T. J. (2010), *Cosmogenic nuclides principles, concepts and applications in the earth surface sciences*, Cambridge University Press, Cambridge; New York.

Ebert, K., J. Willenbring, K. P. Norton, A. Hall, and C. Hättestrand (2012), Meteoric 10Be concentrations from saprolite and till in northern Sweden: Implications for glacial erosion and age, *Quaternary Geochronology*, *12*, 11–22, doi:10.1016/j.quageo.2012.05.005.

Egan, K. E., R. E. Rickaby, M. J. Leng, K. R. Hendry, M. Hermoso, H. J. Sloane, H. Bostock, and A. N. Halliday (2012), Diatom silicon isotopes as a proxy for silicic acid utilisation: A Southern Ocean core top calibration, *Geochimica et Cosmochimica Acta*, *96*, 174–192, doi:10.1016/j.gca.2012.08.002.

Eisenhauer, A., R. F. Spielhagen, M. Frank, G. Hentzschel, A. Mangini, P. W. Kubik, B. Dittrich-Hannen, and T. Billen (1994), 10Be records of sediment cores from high northern latitudes: Implications for environmental and climatic changes, *Earth and Planetary Science Letters*, *124*(1), 171–184, doi:10.1016/0012-821X(94)00069-7.

Ellwood, M. J., and K. A. Hunter (1999), Determination of the Zn/Si ratio in diatom opal:

a method for the separation, cleaning and dissolution of diatoms, *Marine Chemistry*, *66*(34), 149–160, doi:10.1016/S0304-4203(99)00037-7.

Escutia, C., L. De Santis, F. Donda, R. Dunbar, A. Cooper, G. Brancolini, and S. Eittreim (2005), Cenozoic ice sheet history from East Antarctic Wilkes Land continental margin sediments, *Global and Planetary Change*, *45*(1-3), 51–81, doi:10.1016/j.gloplacha.2004.09.010.

Escutia, C., H. Brinkhuis, A. Klaus, and the IODP Expedition 318 Scientists (2011), IODP Expedition 318: From Greenhouse to Icehouse at the Wilkes Land Antarctic Margin, *Scientific Drilling*, (12, September 2011), doi:10.2204/iodp.sd.12.02.2011.

Feakins, S. J., S. Warny, and J.-E. Lee (2012), Hydrologic cycling over Antarctica during the middle Miocene warming, *Nature Geoscience*, *5*(8), 557–560, doi:10.1038/ngeo1498.

Ferraccioli, F., E. Armadillo, T. Jordan, E. Bozzo, and H. Corr (2009), Aeromagnetic exploration over the East Antarctic Ice Sheet: A new view of the Wilkes Subglacial Basin, *Tectonophysics*, *478*(1-2), 62–77, doi:10.1016/j.tecto.2009.03.013.

Field, C. V., G. A. Schmidt, D. Koch, and C. Salyk (2006), Modeling production and climate-related impacts on ^{10} Be concentration in ice cores, *Journal of Geophysical Research*, *111*(D15), doi:10.1029/2005JD006410.

Fielding, C. R., et al. (2011), Sequence stratigraphy of the ANDRILL AND-2A drillcore, Antarctica: A long-term, ice-proximal record of Early to Mid-Miocene climate, sea-level and glacial dynamism, *Palaeogeography, Palaeoclimatology, Palaeoecology*, *305*(1-4), 337–351, doi:10.1016/j.palaeo.2011.03.026.

Finkel, R. C., and K. Nishiizumi (1997), Beryllium 10 concentrations in the Greenland Ice Sheet Project 2 ice core from 340 ka, *Journal of Geophysical Research: Oceans*, *102*(C12), 26699–26706, doi:10.1029/97JC01282.

Fountain, A. G., H. J. Basagic, and S. Niebuhr (2016), Glaciers in equilibrium, McMurdo Dry Valleys, Antarctica, *Journal of Glaciology*, pp. 1–14, doi:10.1017/jog.2016.86.

Frank, M., A. Eisenhauer, W. J. Bonn, P. Walter, H. Grobe, P. W. Kubik, B. Dittrich-Hannen, and A. Mangini (1995), Sediment redistribution versus paleoproductivity change: Weddell Sea margin sediment stratigraphy and biogenic particle flux of the last 250,000 years deduced from 230Thex, 10Be and biogenic barium profiles, *Earth and Planetary Science Letters*, *136*(3-4), 559–573.

Frank, M., B. Schwarz, S. Baumann, P. W. Kubik, M. Suter, and A. Mangini (1997), A 200 kyr record of cosmogenic radionuclide production rate and geomagnetic field intensity from 10Be in globally stacked deep-sea sediments1, *Earth and Planetary Science Letters*, *149*(14), 121–129, doi:10.1016/S0012-821X(97)00070-8.

Frank, M., R. Gersonde, M. R. van der Loeff, G. Bohrmann, C. C. Nrnberg, P. W. Kubik,

M. Suter, and A. Mangini (2000), Similar glacial and interglacial export bioproductivity in the Atlantic Sector of the Southern Ocean: Multiproxy evidence and implications for glacial atmospheric CO $_2$, *Paleoceanography*, *15*(6), 642–658, doi:10.1029/2000PA000497.

Frank, M., M. M. Rutgers van der Loeff, P. W. Kubik, and A. Mangini (2002), Quasi-conservative behaviour of 10Be in deep waters of the Weddell Sea and the Atlantic sector of the Antarctic Circumpolar Current, *Earth and Planetary Science Letters*, *201*(1), 171–186, doi:10.1016/S0012-821X(02)00688-X.

Frank, M., J. Backman, M. Jakobsson, K. Moran, M. O'Regan, J. King, B. A. Haley, P. W. Kubik, and D. Garbe-Schönberg (2008), Beryllium isotopes in central Arctic Ocean sediments over the past 12.3 million years: Stratigraphic and paleoclimatic implications: BERYLLIUM ISOTOPES IN ACEX SEDIMENTS, *Paleoceanography*, *23*(1), n/a–n/a, doi:10.1029/2007PA001478.

Frank, M., D. Porcelli, P. Andersson, M. Baskaran, G. Bjrk, P. Kubik, B. Hattendorf, and D. Guenther (2009), The dissolved Beryllium isotope composition of the Arctic Ocean, *Geochimica et Cosmochimica Acta*, *73*(20), 6114–6133, doi:10.1016/j.gca.2009.07.010.

Fretwell, P., et al. (2013), Bedmap2: improved ice bed, surface and thickness datasets for Antarctica, *The Cryosphere*, *7*(1), 375–393, doi:10.5194/tc-7-375-2013.

Frezzotti, M., et al. (2004), New estimations of precipitation and surface sublimation in East Antarctica from snow accumulation measurements, *Climate Dynamics*, *23*(7-8), 803–813, doi:10.1007/s00382-004-0462-5.

Goehring, B. M., J. M. Schaefer, C. Schluechter, N. A. Lifton, R. C. Finkel, A. J. T. Jull, N. Akar, and R. B. Alley (2011), The Rhone Glacier was smaller than today for most of the Holocene, *Geology*, *39*(7), 679–682, doi:10.1130/G32145.1.

Goehring, B. M., P. Muzikar, and N. A. Lifton (2013), An in situ 14C10Be Bayesian isochron approach for interpreting complex glacial histories, *Quaternary Geochronology*, *15*, 61–66, doi:10.1016/j.quageo.2012.11.007.

Goldner, A., N. Herold, and M. Huber (2014), The challenge of simulating the warmth of the mid-Miocene climatic optimum in CESM1, *Clim. Past*, *10*(2), 523–536, doi:10.5194/cp-10-523-2014.

Golledge, N. R., D. E. Kowalewski, T. R. Naish, R. H. Levy, C. J. Fogwill, and E. G. W. Gasson (2015), The multi-millennial Antarctic commitment to future sea-level rise, *Nature*, *526*(7573), 421–425, doi:10.1038/nature15706.

Gosse, J. C., and F. M. Phillips (2001), Terrestrial in situ cosmogenic nuclides: theory and application, *Quaternary Science Reviews*, *20*(14), 1475–1560.

Gosse, J. C., J. Klein, B. Lawn, R. Middleton, and E. B. Evenson (1995), Beryllium-10

Dating of the Duration and Retreat of the Last Pinedale Glacial Sequence, *Science*, *268*(5215), 1329–1333, doi:10.1126/science.268.5215.1329.

Graham, I. J., R. G. Ditchburn, G. G. C. Claridge, N. E. Whitehead, A. Zondervan, and D. S. Sheppard (2002), Dating Antarctic soils using atmosphere-derived ^{10}Be and nitrate.

Granger, D. E. (2006), A review of burial dating methods using 26Al and 10Be, *Geological Society of America Special Papers*, *415*, 1–16, doi:10.1130/2006.2415(01).

Granger, D. E., and P. F. Muzikar (2001), Dating sediment burial with in situ-produced cosmogenic nuclides: theory, techniques, and limitations, *Earth and Planetary Science Letters*, *188*(1), 269–281.

Granger, D. E., J. W. Kirchner, and R. Finkel (1996), Spatially Averaged Long-Term Erosion Rates Measured from in Situ-Produced Cosmogenic Nuclides in Alluvial Sediment, *The Journal of Geology*, *104*(3), 249–257.

Granger, D. E., N. A. Lifton, and J. K. Willenbring (2013), A cosmic trip: 25 years of cosmogenic nuclides in geology, *Geological Society of America Bulletin*, *125*(9-10), 1379–1402, doi:10.1130/B30774.1.

Hambrey, M. J., and B. McKelvey (2000), Major Neogene fluctuations of the East Antarctic ice sheet: Stratigraphic evidence from the Lambert Glacier region, *Geology*, *28*(10), 887, doi:10.1130/0091-7613(2000)28⟨887:MNFOTE⟩2.0.CO;2.

Haywood, A. M., and P. J. Valdes (2004), Modelling Pliocene warmth: contribution of atmosphere, oceans and cryosphere, *Earth and Planetary Science Letters*, *218*(3-4), 363–377, doi:10.1016/S0012-821X(03)00685-X.

Heikkilä, U. (2007), Modeling of the atmospheric transport of the cosmogenic radionuclides 10Be and 7Be using the ECHAM5HAM General Circulation Model, Ph.D. thesis, Helsinki University of Technology.

Heikkilä, U., and F. von Blanckenburg (2015), The global distribution of Holocene meteoric 10Be fluxes from atmospheric models. Distribution maps for terrestrial Earths surface applications.

Heikkilä, U., J. Beer, J. A. Abreu, and F. Steinhilber (2013), On the Atmospheric Transport and Deposition of the Cosmogenic Radionuclides (10Be): A Review, *Space Science Reviews*, *176*(1-4), 321–332, doi:10.1007/s11214-011-9838-0.

Hein, A. S., C. J. Fogwill, D. E. Sugden, and S. Xu (2014), Geological scatter of cosmogenic-nuclide exposure ages in the Shackleton Range, Antarctica: Implications for glacial history, *Quaternary Geochronology*, *19*, 52–66, doi:10.1016/j.quageo.2013.03.008.

Heyman, J., A. P. Stroeven, J. M. Harbor, and M. W. Caffee (2011), Too young or too old: Evaluating cosmogenic exposure dating based on an analysis of compiled boulder

exposure ages, *Earth and Planetary Science Letters*, *302*(12), 71–80, doi:10.1016/j.epsl.2010.11.040.

Higgins, S. M., C. H. Hendy, and G. H. Denton (2000), Geochronology of Bonney Drift, Taylor Valley, Antarctica: Evidence for Interglacial Expansions of Taylor Glacier, *Geografiska Annaler: Series A, Physical Geography*, *82*(2-3), 391–409, doi:10.1111/j.0435-3676.2000.00130.x.

Hill, D., A. M. Haywood, R. C. A. Hindmarsh, and P. J. Valdes (2007), Characterizing ice sheets during the Pliocene: evidence from data and models, in *Deep-time perspectives on climate change: marrying the signal from computer models and biological proxies*, edited by M. Williams, A. M. Haywood, F. J. Gregory, and D. N. Schmidt, pp. 517–538, Geological Society of London, London.

Hoffman, M. J., A. G. Fountain, and G. E. Liston (2016), Distributed modeling of ablation (19962011) and climate sensitivity on the glaciers of Taylor Valley, Antarctica, *Journal of Glaciology*, *62*(232), 215–229, doi:10.1017/jog.2015.2.

Hooke, R. L. (2005), *Principles of glacier mechanics*, Cambridge university press.

Horiuchi, K., K. Minoura, K. Kobayashi, T. Nakamura, S. Hatori, H. Matsuzaki, and T. Kawai (1999), Last-Glacial to Post-Glacial 10Be fluctuations in a sediment core from the Academician Ridge, Lake Baikal, *Geophysical Research Letters*, *26*(8), 1047–1050, doi:10.1029/1999GL900163.

Horiuchi, K., K. Kobayashi, T. Oda, T. Nakamura, C. Fujimura, H. Matsuzaki, and Y. Shibata (2000), Climate-induced fluctuations of 10Be concentration in Lake Baikal sediments, *Nuclear Instruments and Methods in Physics Research Section B: Beam Interactions with Materials and Atoms*, *172*(1-4), 562–567.

Huybrechts, P. (1993), Glaciological Modelling of the Late Cenozoic East Antarctic Ice Sheet: Stability or Dynamism?, *Geografiska Annaler. Series A, Physical Geography*, *75*(4), 221–238.

Ivy-Ochs, S., and J. P. Briner (2014), Dating Disappearing Ice with Cosmogenic Nuclides, *Elements*, *10*(5), 351–356, doi:10.2113/gselements.10.5.351.

Ivy-Ochs, S., C. Schlchter, P. W. Kubik, B. Dittrich-Hannen, and J. Beer (1995), Minimum 10Be exposure ages of early Pliocene for the Table Mountain plateau and the Sirius Group at Mount Fleming, Dry Valleys, Antarctica, *Geology*, *23*(11), 1007, doi:10.1130/0091-7613(1995)023⟨1007:MBEAOE⟩2.3.CO;2.

Johnson, G. C. (2008), Quantifying Antarctic Bottom Water and North Atlantic Deep Water volumes, *Journal of Geophysical Research: Oceans*, *113*(C5), C05027, doi:10.1029/2007JC004477.

Kennicutt, M. I., et al. (2015), A roadmap for Antarctic and Southern Ocean sci-

ence for the next two decades and beyond, *Antarctic Science*, *27*(01), 3–18, doi: 10.1017/S0954102014000674.

Klein, J., R. Giegengack, R. Middleton, P. Sharma, J. R. Underwood, and R. A. Weeks (1986), Revealing Histories of Exposure Using In Situ Produced 26Al and 10Be in Libyan Desert Glass, *Radiocarbon*, *28*(2A), 547–555, doi:10.1017/S0033822200007700.

Kleman, J., and N. F. Glasser (2007), The subglacial thermal organisation (STO) of ice sheets, *Quaternary Science Reviews*, *26*(56), 585–597, doi:10.1016/j.quascirev.2006.12.010.

Kohl, C., and K. Nishiizumi (1992), Chemical isolation of quartz for measurement of in-situ-produced cosmogenic nuclides, *Geochimica et Cosmochimica Acta*, *56*(9), 3583–3587.

Korschinek, G., et al. (2010), A new value for the half-life of 10Be by Heavy-Ion Elastic Recoil Detection and liquid scintillation counting, *Nuclear Instruments and Methods in Physics Research Section B: Beam Interactions with Materials and Atoms*, *268*(2), 187–191, doi:10.1016/j.nimb.2009.09.020.

Kusakabe, M., T. L. Ku, J. Vogel, J. R. Southon, D. E. Nelson, and G. Richards (1982), 10Be profiles in seawater, *Nature*, *299*(5885), 712–714, doi:10.1038/299712a0.

Lal, D. (1991), Cosmic ray labeling of erosion surfaces: in situ nuclide production rates and erosion models, *Earth and Planetary Science Letters*, *104*(2-4), 424–439.

Lal, D., and B. Peters (1967), Cosmic Ray Produced Radioactivity on the Earth, in *Kosmische Strahlung II / Cosmic Rays II*, edited by K. Sitte, no. 9 / 46 / 2 in Handbuch der Physik / Encyclopedia of Physics, pp. 551–612, Springer Berlin Heidelberg, dOI: 10.1007/978-3-642-46079-1_7.

Lal, D., C. Charles, L. Vacher, J. Goswami, A. Jull, L. McHargue, and R. Finkel (2006), Paleo-ocean chemistry records in marine opal: Implications for fluxes of trace elements, cosmogenic nuclides (10Be and 26Al), and biological productivity, *Geochimica et Cosmochimica Acta*, *70*(13), 3275–3289, doi:10.1016/j.gca.2006.04.004.

Lebatard, A.-E., et al. (2010), Application of the authigenic 10Be/9Be dating method to continental sediments: Reconstruction of the Mio-Pleistocene sedimentary sequence in the early hominid fossiliferous areas of the northern Chad Basin, *Earth and Planetary Science Letters*, *297*(1-2), 57–70, doi:10.1016/j.epsl.2010.06.003.

Levy, R., et al. (2012), Late Neogene climate and glacial history of the Southern Victoria Land coast from integrated drill core, seismic and outcrop data, *Global and Planetary Change*, *8081*, 61–84, doi:10.1016/j.gloplacha.2011.10.002.

Lewis, A., D. Marchant, A. Ashworth, S. Hemming, and M. Machlus (2007), Major middle Miocene global climate change: Evidence from East Antarctica and the Transantarctic

Mountains, *Geological Society of America Bulletin*, *119*(11-12), 1449–1461, doi:10.1130/0016-7606(2007)119[1449:MMMGCC]2.0.CO;2.

Lewis, A. R., and A. C. Ashworth (2015), An early to middle Miocene record of ice-sheet and landscape evolution from the Friis Hills, Antarctica, *Geological Society of America Bulletin*, p. B31319.1, doi:10.1130/B31319.1.

Lewis, A. R., D. R. Marchant, D. E. Kowalewski, S. L. Baldwin, and L. E. Webb (2006), The age and origin of the Labyrinth, western Dry Valleys, Antarctica: Evidence for extensive middle Miocene subglacial floods and freshwater discharge to the Southern Ocean, *Geology*, *34*(7), 513, doi:10.1130/G22145.1.

Lewis, A. R., et al. (2008), Mid-Miocene cooling and the extinction of tundra in continental Antarctica, *Proceedings of the National Academy of Sciences*, *105*(31), 10676–10680.

Lifton, N., T. Sato, and T. J. Dunai (2014), Scaling in situ cosmogenic nuclide production rates using analytical approximations to atmospheric cosmic-ray fluxes, *Earth and Planetary Science Letters*, *386*, 149–160, doi:10.1016/j.epsl.2013.10.052.

Lifton, N. A., J. W. Bieber, J. M. Clem, M. L. Duldig, P. Evenson, J. E. Humble, and R. Pyle (2005), Addressing solar modulation and long-term uncertainties in scaling secondary cosmic rays for in situ cosmogenic nuclide applications, *Earth and Planetary Science Letters*, *239*(12), 140–161, doi:10.1016/j.epsl.2005.07.001.

Ljung, K., S. Bjrck, R. Muscheler, J. Beer, and P. W. Kubik (2007), Variable 10Be fluxes in lacustrine sediments from Tristan da Cunha, South Atlantic: a solar record?, *Quaternary Science Reviews*, *26*(7-8), 829–835, doi:10.1016/j.quascirev.2006.12.016.

Lundberg, T., T. Ticich, G. F. Herzog, T. Hughes, G. Ashley, R. K. Moniot, C. Tuniz, T. Kruse, and W. Savin (1983), Lundberg_1983_JGR.pdf, *Journal of Geophysical Research: Oceans*.

Marchant, D. R., and J. W. Head (2007), Antarctic dry valleys: Microclimate zonation, variable geomorphic processes, and implications for assessing climate change on Mars, *Icarus*, *192*(1), 187–222, doi:10.1016/j.icarus.2007.06.018.

Marchant, D. R., G. H. Denton, D. E. Sugden, and C. C. Swisher (1993), Miocene Glacial Stratigraphy and Landscape Evolution of the Western Asgard Range, Antarctica, *Geografiska Annaler. Series A, Physical Geography*, *75*(4), 303, doi:10.2307/521205.

Marchant, D. R., G. H. Denton, J. G. Bockheim, S. C. Wilson, and A. R. Kerr (1994), Quaternary changes in level of the upper Taylor Glacier, Antarctica: implications for paleoclimate and East Antarctic Ice Sheet dynamics, *Boreas*, *23*(1), 29–43, doi:10.1111/j.1502-3885.1994.tb00583.x.

Marchant, D. R., G. H. Denton, C. C. Swisher, and N. Potter (1996), Late Cenozoic Antarctic paleoclimate reconstructed from volcanic ashes in the Dry Valleys region of

southern Victoria Land, *Geological Society of America Bulletin*, *108*(2), 181–194, doi:10.1130/0016-7606(1996)108⟨0181:LCAPRF⟩2.3.CO;2.

Margerison, H., W. Phillips, F. Stuart, and D. Sugden (2005), Cosmogenic 3He concentrations in ancient flood deposits from the Coombs Hills, northern Dry Valleys, East Antarctica: interpreting exposure ages and erosion rates, *Earth and Planetary Science Letters*, *230*(1-2), 163–175, doi:10.1016/j.epsl.2004.11.007.

Marrero, S. M., F. M. Phillips, B. Borchers, N. Lifton, R. Aumer, and G. Balco (2016), Cosmogenic nuclide systematics and the CRONUScalc program, *Quaternary Geochronology*, *31*, 160–187, doi:10.1016/j.quageo.2015.09.005.

Masarik, J., and J. Beer (1999), Simulation of particle fluxes and cosmogenic nuclide production in the Earth's atmosphere, *Journal of Geophysical Research: Atmospheres*, *104*(D10), 12099–12111, doi:10.1029/1998JD200091.

Masarik, J., and J. Beer (2009), An updated simulation of particle fluxes and cosmogenic nuclide production in the Earth's atmosphere, *Journal of Geophysical Research: Atmospheres*, *114*(D11), D11103, doi:10.1029/2008JD010557.

Middleton, J. L., R. P. Ackert Jr., and S. Mukhopadhyay (2012), Pothole and channel system formation in the McMurdo Dry Valleys of Antarctica: New insights from cosmogenic nuclides, *Earth and Planetary Science Letters*, *355356*, 341–350, doi:10.1016/j.epsl.2012.08.017.

Mikucki, J. A., E. Auken, S. Tulaczyk, R. A. Virginia, C. Schamper, K. I. Srensen, P. T. Doran, H. Dugan, and N. Foley (2015), Deep groundwater and potential subsurface habitats beneath an Antarctic dry valley, *Nature Communications*, *6*, doi:10.1038/ncomms7831.

Minoletti, F., M. Hermoso, and V. Gressier (2008), Separation of sedimentary micron-sized particles for palaeoceanography and calcareous nannoplankton biogeochemistry, *Nature Protocols*, *4*(1), 14–24, doi:10.1038/nprot.2008.200.

Morgan, D. J., J. Putkonen, G. Balco, and J. Stone (2010), Degradation of glacial deposits quantified with cosmogenic nuclides, Quartermain Mountains, Antarctica, *Earth Surface Processes and Landforms*, *36*(2), 217–228.

Muzikar, P. (2011), Geological constraints and 26Al10Be burial dating isochrons, *Earth Surface Processes and Landforms*, *36*(7), 946–952, doi:10.1002/esp.2124.

Nishiizumi, K. (2004), Preparation of 26Al AMS standards, *Nuclear Instruments and Methods in Physics Research Section B: Beam Interactions with Materials and Atoms*, *223224*, 388–392, doi:10.1016/j.nimb.2004.04.075.

Nishiizumi, K., C. Kohl, J. Arnold, J. Klein, D. Fink, and R. Middleton (1991), Cosmic ray produced 10 Be and 26 Al in Antarctic rocks: exposure and erosion history, *Earth and Planetary Science Letters*, *104*(2), 440–454.

Nishiizumi, K., M. Imamura, M. W. Caffee, J. R. Southon, R. C. Finkel, and J. McAninch (2007), Absolute calibration of 10Be AMS standards, *Nuclear Instruments and Methods in Physics Research Section B: Beam Interactions with Materials and Atoms*, *258*(2), 403–413, doi:10.1016/j.nimb.2007.01.297.

Passchier, S., G. Browne, B. Field, C. R. Fielding, L. A. Krissek, K. Panter, S. F. Pekar, and and ANDRILL-SMS Science Team (2011), Early and middle Miocene Antarctic glacial history from the sedimentary facies distribution in the AND-2A drill hole, Ross Sea, Antarctica, *Geological Society of America Bulletin*, *123*(11-12), 2352–2365, doi:10.1130/B30334.1.

Passchier, S., D. J. Ciarletta, T. E. Miriagos, P. K. Bijl, and S. M. Bohaty (2016), An Antarctic stratigraphic record of stepwise ice growth through the Eocene-Oligocene transition, pp. B31,482–1.

Patterson, M. O., et al. (2014), Orbital forcing of the East Antarctic ice sheet during the Pliocene and Early Pleistocene, *Nature Geoscience*, *7*(11), 841–847, doi:10.1038/ngeo2273.

Pavich, M. J., L. Brown, J. Harden, J. Klein, and R. Middleton (1986), 10Be distribution in soils from Merced River terraces, California, *Geochimica et Cosmochimica Acta*, *50*(8), 1727–1735, doi:10.1016/0016-7037(86)90134-1.

Pollard, D., and R. M. DeConto (2009), Modelling West Antarctic ice sheet growth and collapse through the past five million years, *Nature*, *458*(7236), 329–332, doi:10.1038/nature07809.

Pollard, D., R. M. DeConto, and R. B. Alley (2015), Potential Antarctic Ice Sheet retreat driven by hydrofracturing and ice cliff failure, *Earth and Planetary Science Letters*, *412*, 112–121, doi:10.1016/j.epsl.2014.12.035.

Pritchard, H. D., R. J. Arthern, D. G. Vaughan, and L. A. Edwards (2009), Extensive dynamic thinning on the margins of the Greenland and Antarctic ice sheets, *Nature*, *461*(7266), 971–975, doi:10.1038/nature08471.

Putkonen, J., and T. Swanson (2003), Accuracy of cosmogenic ages for moraines, *Quaternary Research*, *59*(2), 255–261, doi:10.1016/S0033-5894(03)00006-1.

Putkonen, J., G. Balco, and D. Morgan (2008), Slow regolith degradation without creep determined by cosmogenic nuclide measurements in Arena Valley, Antarctica, *Quaternary Research*, *69*(2), 242–249, doi:10.1016/j.yqres.2007.12.004.

Ragueneau, O., N. Savoye, Y. Del Amo, J. Cotten, B. Tardiveau, and A. Leynaert (2005), A new method for the measurement of biogenic silica in suspended matter of coastal waters: using Si:Al ratios to correct for the mineral interference, *Continental Shelf Research*, *25*(56), 697–710, doi:10.1016/j.csr.2004.09.017.

Raisbeck, G. M., F. Yiou, M. Fruneau, J. M. Loiseaux, M. Lieuvin, J. C. Ravel, and C. Lorius (1981), Cosmogenic 10Be concentrations in Antarctic ice during the past 30,000 years, *Nature*, *292*(5826), 825–826, doi:10.1038/292825a0.

Raisbeck, G. M., F. Yiou, O. Cattani, and J. Jouzel (2006), 10Be evidence for the MatuyamaBrunhes geomagnetic reversal in the EPICA Dome C ice core, *Nature*, *444*(7115), 82–84, doi:10.1038/nature05266.

Rebesco, M., A. Camerlenghi, R. Geletti, and M. Canals (2006), Margin architecture reveals the transition to the modern Antarctic ice sheet ca. 3 Ma, *Geology*, *34*(4), 301, doi:10.1130/G22000.1.

Rhodes, E. J. (2011), Optically Stimulated Luminescence Dating of Sediments over the Past 200,000 Years, *Annual Review of Earth and Planetary Sciences*, *39*(1), 461–488, doi:10.1146/annurev-earth-040610-133425.

Riebe, C. S., L. S. Sklar, C. E. Lukens, and D. L. Shuster (2015), Climate and topography control the size and flux of sediment produced on steep mountain slopes, *Proceedings of the National Academy of Sciences*, p. 201503567, doi:10.1073/pnas.1503567112.

Rignot, E., S. Jacobs, J. Mouginot, and B. Scheuchl (2013), Ice-Shelf Melting Around Antarctica, *Science*, *341*(6143), 266–270, doi:10.1126/science.1235798.

Riihimaki, C. A., and J. C. Libarkin (2007), Terrestrial Cosmogenic Nuclides as Paleoaltimetric Proxies, *Reviews in Mineralogy and Geochemistry*, *66*(1), 269–278, doi:10.2138/rmg.2007.66.11.

Rinterknecht, V. R., et al. (2006), The Last Deglaciation of the Southeastern Sector of the Scandinavian Ice Sheet, *Science*, *311*(5766), 1449–1452, doi:10.1126/science.1120702.

Rintoul, S. R. (2007), Rapid freshening of Antarctic Bottom Water formed in the Indian and Pacific oceans, *Geophysical Research Letters*, *34*(6), L06606, doi:10.1029/2006GL028550.

Ritz, C., T. L. Edwards, G. Durand, A. J. Payne, V. Peyaud, and R. C. A. Hindmarsh (2015), Potential sea-level rise from Antarctic ice-sheet instability constrained by observations, *Nature*, *528*(7580), 115–118, doi:10.1038/nature16147.

Royer, D. L. (2014), Atmospheric CO2 and O2 during the Phanerozoic: Tools, patterns, and impacts., *Treatise on Geochemistry*, *6*, 251–267.

Sandroni, S., and F. M. Talarico (2011), The record of Miocene climatic events in AND-2A drill core (Antarctica): Insights from provenance analyses of basement clasts, *Global and Planetary Change*, *75*(12), 31–46, doi:10.1016/j.gloplacha.2010.10.002.

Schäfer, J. M., S. Ivy-Ochs, R. Wieler, I. Leya, H. Baur, G. H. Denton, and C. Schlchter (1999), Cosmogenic noble gas studies in the oldest landscape on earth: surface exposure ages of the Dry Valleys, Antarctica, *Earth and Planetary Science Letters*, *167*(3), 215–226.

Scherer, R. P., A. Aldahan, S. Tulaczyk, G. Possnert, H. Engelhardt, and B. Kamb (1998), Pleistocene Collapse of the West Antarctic Ice Sheet, *Science*, *281*(5373), 82–85, doi: 10.1126/science.281.5373.82.

Scherer, R. P., R. M. DeConto, D. Pollard, and R. B. Alley (2016), Windblown Pliocene diatoms and East Antarctic Ice Sheet retreat, *Nature Communications*, *7*, 12957, doi: 10.1038/ncomms12957.

Schiller, M., W. Dickinson, R. G. Ditchburn, I. J. Graham, and A. Zondervan (2009), Atmospheric ^{10} Be in an Antarctic soil: Implications for climate change, *Journal of Geophysical Research*, *114*(F1), doi:10.1029/2008JF001052.

Schiller, M., W. Dickinson, A. Zondervan, R. Ditchburn, and N. Wang (2014), Rapid soil accumulation in a frozen landscape, *Geology*, *42*(4), 335–338, doi:10.1130/G35450.1.

Schuler, C., et al. (1991), A multitracer study of radionuclides in Lake Zurich, Switzerland: 1. Comparison of atmospheric and sedimentary fluxes of 7Be, 10Be, 210Pb, 210Po, and 137Cs, *Journal of Geophysical Research: Oceans*, *96*(C9), 17051–17065, doi:10.1029/ 91JC01765.

Sharma, P., R. Mahannah, W. Moore, T. Ku, and J. Southon (1987), Transport of10Be and9Be in the ocean, *Earth and Planetary Science Letters*, *86*(1), 69–76, doi:10.1016/ 0012-821X(87)90189-0.

Shemesh, A., R. A. Mortlock, and P. N. Froelich (1989), Late Cenozoic Ge/Si record of marine biogenic opal: Implications for variations of riverine fluxes to the ocean, *Paleoceanography*, *4*(3), 221–234, doi:10.1029/PA004i003p00221.

Shen, C., J. Beer, P. W. Kubik, M. Suter, M. Borkovec, and T. Liu (2004), Grain size distribution, 10Be content and magnetic susceptibility of micrometernanometer loess materials, *Nuclear Instruments and Methods in Physics Research Section B: Beam Interactions with Materials and Atoms*, *223-224*, 613–617.

Shevenell, A. E., J. P. Kennett, and D. W. Lea (2004), Middle Miocene Southern Ocean Cooling and Antarctic Cryosphere Expansion, *Science*, *305*(5691), 1766–1770, doi:10. 1126/science.1100061.

Simon, Q., N. Thouveny, D. L. Bourls, L. Nuttin, C. Hillaire-Marcel, and G. St-Onge (2016), Authigenic 10Be/9Be ratios and 10Be-fluxes (230Thxs-normalized) in central Baffin Bay sediments during the last glacial cycle: Paleoenvironmental implications, *Quaternary Science Reviews*, *140*, 142–162, doi:10.1016/j.quascirev.2016.03.027.

Sjunneskog, C., R. Scherer, A. Aldahan, and G. Possnert (2007), 10Be in glacial marine sediment of the Ross Sea, Antarctica, a potential tracer of depositional environment and sediment chronology, *Nuclear Instruments and Methods in Physics Research Section B: Beam Interactions with Materials and Atoms*, *259*(1), 576–583, doi:10.1016/j.nimb.2007. 01.203.

Staiger, J., D. Marchant, J. Schaefer, P. Oberholzer, J. Johnson, A. Lewis, and K. Swanger (2006a), Plio-Pleistocene history of Ferrar Glacier, Antarctica: Implications for climate and ice sheet stability, *Earth and Planetary Science Letters*, *243*(3-4), 489–503, doi: 10.1016/j.epsl.2006.01.037.

Staiger, J. W., J. Gosse, E. C. Little, D. J. Utting, R. Finkel, J. V. Johnson, and J. Fastook (2006b), Glacial erosion and sediment dispersion from detrital cosmogenic nuclide analyses of till, *Quaternary Geochronology*, *1*(1), 29–42, doi:10.1016/j.quageo.2006.06.009.

Steig, E. J., P. J. Polissar, and M. Stuiver (1995), Cosmogenic isotope concentrations at Taylor Dome, Antarctica, *Antarctic Journal of the United States*, *30*, 95–97.

Steig, E. J., D. L. Morse, E. D. Waddington, M. Stuiver, P. M. Grootes, P. A. Mayewski, M. S. Twickler, and S. I. Whitlow (2000), Wisconsinan and Holocene Climate History from an Ice Core at Taylor Dome, Western Ross Embayment, Antarctica, *Geografiska Annaler. Series A, Physical Geography*, *82*(2/3), 213–235.

Stocker, T. F. (2014), *Climate Change 2013: The Physical Science Basis: Working Group I Contribution to the Fifth Assessment Report of the Intergovernmental Panel on Climate Change*, Cambridge University Press, google-Books-ID: o4gaBQAAQBAJ.

Stone, J. O. (2000), Air pressure and cosmogenic isotope production, *Journal of Geophysical Research: Solid Earth*, *105*(B10), 23753–23759, doi:10.1029/2000JB900181.

Sugden, D. E. (1996), The East Antarctic Ice Sheet: Unstable Ice or Unstable Ideas?, *Transactions of the Institute of British Geographers*, *21*(3), 443, doi:10.2307/622590.

Sugden, D. E., D. R. Marchant, and G. H. Denton (1993), The Case for a Stable East Antarctic Ice Sheet: The Background, *Geografiska Annaler. Series A, Physical Geography*, *75*(4), 151–154, doi:10.2307/521199.

Summerfield, M. A., F. M. Stuart, H. A. P. Cockburn, D. E. Sugden, G. H. Denton, T. Dunai, and D. R. Marchant (1999), Long-term rates of denudation in the Dry Valleys, Transantarctic Mountains, southern Victoria Land, Antarctica based on in-situ-produced cosmogenic 21Ne, *Geomorphology*, *27*(1), 113–129.

Swanger, K. M., D. R. Marchant, D. E. Kowalewski, and J. W. Head III (2010), Viscous flow lobes in central Taylor Valley, Antarctica: Origin as remnant buried glacial ice, *Geomorphology*, *120*(34), 174–185, doi:10.1016/j.geomorph.2010.03.024.

Swanger, K. M., D. R. Marchant, J. M. Schaefer, G. Winckler, and J. W. Head III (2011), Elevated East Antarctic outlet glaciers during warmer-than-present climates in southern Victoria Land, *Global and Planetary Change*, *79*(12), 61–72, doi:10.1016/j.gloplacha.2011.07.012.

Swanger, K. M., J. M. Schaefer, G. Winckler, D. R. Marchant, J. L. Lamp, and D. E. Kowalewski (2014), Cosmogenic 3He exposure dating of glacial deposits in the Olympus

Range, Antarctica: influence of cold-based deposition and weathering processes on age scatter.

Swanger, K. M., J. L. Lamp, G. Winckler, J. M. Schaefer, and D. R. Marchant (2017), Glacier advance during Marine Isotope Stage 11 in the McMurdo Dry Valleys of Antarctica, *Scientific Reports*, *7*, 41433, doi:10.1038/srep41433.

Tauxe, L., et al. (2012), Chronostratigraphic framework for the IODP Expedition 318 cores from the Wilkes Land Margin: Constraints for paleoceanographic reconstruction, *Paleoceanography*, *27*(2), PA2214, doi:10.1029/2012PA002308.

Tauxe, L., S. Sugisaki, F. Jimnez-Espejo, C. Escutia, C. P. Cook, T. van de Flierdt, and M. Iwai (2015), Geology of the Wilkes land sub-basin and stability of the East Antarctic Ice Sheet: Insights from rock magnetism at IODP Site U1361, *Earth and Planetary Science Letters*, *412*, 61–69, doi:10.1016/j.epsl.2014.12.034.

Taylor, A., W. Blake, L. Couldrick, and M. Keith-Roach (2012), Sorption behaviour of beryllium-7 and implications for its use as a sediment tracer, *Geoderma*, *187-188*, 16–23, doi:10.1016/j.geoderma.2012.04.013.

Taylor, T. P., M. Ding, D. S. Ehler, T. M. Foreman, J. P. Kaszuba, and N. N. Sauer (2003), Beryllium in the Environment: A Review, *Journal of Environmental Science and Health, Part A*, *38*(2), 439–469, doi:10.1081/ESE-120016906.

Ticich, T., et al. (1986), 10Be contents of Mono Lake sediments: search for enhancement during a geomagnetic excursion, *Geophysical Journal International*, *87*(2), 487–492.

Tjallingii, R., U. Rhl, M. Klling, and T. Bickert (2007), Influence of the water content on X-ray fluorescence core-scanning measurements in soft marine sediments, *Geochemistry, Geophysics, Geosystems*, *8*(2), Q02004, doi:10.1029/2006GC001393.

Turnbull, I. M., A. H. Allibone, P. J. Forsyth, and D. W. Heron (1994), *Geology of the Bull Pass-St Johns Range Area, Victoria Land, Antarctica*, no. 14 in geological map, Institute of Geological and Nuclear Sciences Ltd., Lower Hutt, New Zealand.

Valletta, R. D., J. K. Willenbring, A. R. Lewis, A. C. Ashworth, and M. Caffee (2015), Extreme decay of meteoric beryllium-10 as a proxy for persistent aridity, *Scientific Reports*, *5*, 17813, doi:10.1038/srep17813.

VandenHeuvel, B. (2002), Surficial geology and geomorphology of the western Olympus Range, Antarctica: Implications for ice-sheet history.

Vaughan, D. G., et al. (2013), Observations: cryosphere, *Climate change*, *2103*, 317–382.

Verma, K., S. Bhattacharya, P. Biswas, P. K. Shrivastava, M. Pandey, N. C. Pant, and I. E. . S. Party (2014), Clay mineralogy of the ocean sediments from the Wilkes Land margin, east Antarctica: implications on the paleoclimate, provenance and sediment

dispersal pattern, *International Journal of Earth Sciences*, *103*(8), 2315–2326, doi:10.1007/s00531-014-1043-4.

Vesely, J., S. A. Norton, P. Skrivan, V. Majer, P. Kram, T. Navratil, and J. M. Kaste (2002), Environmental Chemistry of Beryllium, *Reviews in Mineralogy and Geochemistry*, *50*(1), 291–317, doi:10.2138/rmg.2002.50.7.

von Blanckenburg, F., and J. Bouchez (2014), River fluxes to the sea from the oceans 10Be/9Be ratio, *Earth and Planetary Science Letters*, *387*, 34–43, doi:10.1016/j.epsl.2013.11.004.

von Blanckenburg, F., R. K. O'Nions, N. S. Belshaw, A. Gibb, and J. R. Hein (1996), Global distribution of beryllium isotopes in deep ocean water as derived from FeMn crusts, *Earth and Planetary Science Letters*, *141*(14), 213–226, doi:10.1016/0012-821X(96)00059-3.

von Blanckenburg, F., J. Bouchez, and H. Wittmann (2012), Earth surface erosion and weathering from the 10Be (meteoric)/9Be ratio, *Earth and Planetary Science Letters*, *351352*, 295–305, doi:10.1016/j.epsl.2012.07.022.

von Blanckenburg, F., J. Bouchez, D. E. Ibarra, and K. Maher (2015), Stable runoff and weathering fluxes into the oceans over Quaternary climate cycles, *Nature Geoscience*, *8*(7), 538–542, doi:10.1038/ngeo2452.

Warny, S., R. A. Askin, M. J. Hannah, B. A. Mohr, J. I. Raine, D. M. Harwood, F. Florindo, and the SMS Science Team (2009), Palynomorphs from a sediment core reveal a sudden remarkably warm Antarctica during the middle Miocene, *Geology*, *37*(10), 955–958, doi:10.1130/G30139A.1.

Webb, P. N., D. M. Harwood, B. C. McKelvey, J. H. Mercer, and L. D. Stott (1984), Cenozoic marine sedimentation and ice-volume variation on the East Antarctic craton, *Geology*, *12*(5), 287–291, doi:10.1130/0091-7613(1984)12⟨287:CMSAIV⟩2.0.CO;2.

Whitehead, J. M., S. Wotherspoon, and S. M. Bohaty (2005), Minimal Antarctic sea ice during the Pliocene, *Geology*, *33*(2), 137–140, doi:10.1130/G21013.1.

Willenbring, J. K., and F. von Blanckenburg (2010a), Meteoric cosmogenic Beryllium-10 adsorbed to river sediment and soil: Applications for Earth-surface dynamics, *Earth-Science Reviews*, *98*(1-2), 105–122, doi:10.1016/j.earscirev.2009.10.008.

Willenbring, J. K., and F. von Blanckenburg (2010b), Long-term stability of global erosion rates and weathering during late-Cenozoic cooling, *Nature*, *465*(7295), 211–214, doi:10.1038/nature09044.

Williams, G. D., N. L. Bindoff, S. J. Marsland, and S. R. Rintoul (2008), Formation and export of dense shelf water from the Adlie Depression, East Antarctica, *Journal of Geophysical Research: Oceans*, *113*(C4), C04039, doi:10.1029/2007JC004346.

Williams, T., T. van de Flierdt, S. R. Hemming, E. Chung, M. Roy, and S. L. Goldstein (2010), Evidence for iceberg armadas from East Antarctica in the Southern Ocean during the late Miocene and early Pliocene, *Earth and Planetary Science Letters*, *290*(34), 351–361, doi:10.1016/j.epsl.2009.12.031.

Wilson, G. S. (1995), The neogene east antarctic ice sheet: A dynamic or stable feature?, *Quaternary Science Reviews*, *14*(2), 101–123.

Wittmann, H., F. von Blanckenburg, J. Bouchez, N. Dannhaus, R. Naumann, M. Christl, and J. Gaillardet (2012), The dependence of meteoric 10Be concentrations on particle size in Amazon River bed sediment and the extraction of reactive 10Be/9Be ratios, *Chemical Geology*, *318319*, 126–138, doi:10.1016/j.chemgeo.2012.04.031.

Yiou, F., et al. (1997), Beryllium 10 in the Greenland Ice Core Project ice core at Summit, Greenland, *Journal of Geophysical Research: Oceans*, *102*(C12), 26783–26794, doi:10.1029/97JC01265.

Yokoyama, Y., et al. (2016), Widespread collapse of the Ross Ice Shelf during the late Holocene, *Proceedings of the National Academy of Sciences*, *113*(9), 2354–2359, doi:10.1073/pnas.1516908113.

You, C.-F., T. Lee, and Y.-H. Li (1989), The partition of Be between soil and water, *Chemical Geology*, *77*(2), 105–118, doi:10.1016/0009-2541(89)90136-8.

Zachos, J. C., G. R. Dickens, and R. E. Zeebe (2008), An early Cenozoic perspective on greenhouse warming and carbon-cycle dynamics, *Nature*, *451*(7176), 279–283, doi:10.1038/nature06588.

INDEX

Adélie Depression, 58, 63–65, 91

BET, 55, 71, 94, 97
burial dating, 6, 7, 11, 13, 22, 89

Difference Dating, 7, 20, 25, 88–90

exposure age dating, 3, 6, 7, 11–14, 20, 23, 88

Friis Hills, 7, 8, 73–80, 85, 92

high salinity shelf waters, 58

inheritance, 13, 14, 20, 23, 25, 88

Middle Miocene Climatic Optimum, 8, 79, 84, 92
Middle Miocene Climatic Transition, 79, 84
Middle Pliocene warming, 2–4, 6, 8, 51, 54, 57, 62, 63, 73, 74, 81, 91
Miocene, 3, 4, 6, 18, 74, 80, 81, 84, 88, 92
Monte Carlo, 14, 89

opal, 60, 61

production, 9, 10, 12–19, 51, 52, 58, 89–91

stable hypothesis, 3, 74
steady state erosion, 12, 18, 21, 22, 76

unstable hypothesis, 2, 3, 74